coefficients are evaluated, the subroutine **Polarmix** puts together the magnetic dipole polarization matrix using the dot product calculations performed in Polarmat. Polarmix returns an array, E, to the calling subroutine, Initialize. This multidimensional array, as explained earlier, is proportional to the scattering tensor given by Eq. 7-2.1, and it carefully tracks which nuclear sites and energy levels were involved in the scattering process for each scattering tensor element and for various incident and scattered photon directions (EWALD only does a two-beam calculation in which there is a forward and only one reflection scattering channel). These terms vary insignificantly over the hyperfine resonance energy range and can therefore also be calculated just once (as was the case for photoelectric scattering).

Once Initialize is finished with its calculations, the subroutine **Dispersion** will be ready to solve the linearized dispersion relation given by Eq. 7-4.19 where, in the most general case, $\mathbf{G}_{lin}$ is given by 7-8.1. When called by Dispersion, subroutine **StrFact** constructs the $\mathbf{G}_{lin}$ matrix as a function of energy and angle. Then, by making a call to **Cgg** of the EIS_LIN_PACK code, Dispersion finds both the eigenvalues and eigenvectors of $\mathbf{G}_{lin}$. Next, a thick crystal approximation is applied if the crystal is thick enough to cause floating point overflow problems. Then, subroutine **TandR_coeff** is called to solve the boundary value relation, Eq. 7-4.30, where, in general, $\mathbf{B}_c$ is not decoupled. These last two steps are explained in more detail in the next section. **Clineq** of EIS_LIN_PACK is used to solve the simultaneous equations represented by the boundary value equation.

Once the boundary value equation is solved, the reflected and transmitted amplitudes are constructed. Dispersion then proceeds to calculate the reflected and transmitted electric field intensities by summing the square moduli of the sigma and pi electric field amplitudes. The amplitude and intensity calculations are finally sent to the main calling program, Ewald, for further analysis such as computing energy averaged angular spectra, angle averaged energy spectra, time spectra, or fitting to experimental data (none of these detailed calculations are shown here).

For the EWALD code below, program Ewald and subroutines Dispersion and TandR_coeff are combined in one Fortran code called EWALD.FOR. Subroutines Initialize, Strfact, Polarmat, Polarmix, YIG_basis, FeBO3_basis, and Cdot are combined in another Fortran code called NUCLEAR.FOR.

```
    Program Ewald
c This Program Uses the Ewald-Laue Dynamical Diffraction Theory to Compute the Reflection and
c Transmission Coefficients from a Crystal.
c In this Program : x = sigma polarization component ; y = pi polarization component
c VARIABLES:  (See INITIALIZE Subroutine for more comments on variables)
c devE = (incoming photon energy) - (Bragg energy) (eV) ; devB = (incoming angle) - (Bragg angle) (radians)
c fconv  = conversion factor from Energy to Frequency (/[eV-sec])
c Rx,Ry = Bragg reflected amplitudes ; Rxm,Rym = Laue transmitted amplitudes
c Txm,Tym = Transmission amplitudes ; R,T = reflected and transmitted field intensities
c LINK TO:  NUCLEAR,  EIS_LIN_PACK
c D.E.Brown 1990          (SSRL/STANFORD)
    Complex Txm(600),Tym(600),Rx(600),Ry(600),Rxm(600),Rym(600),uin(4,1)
    Real Freq(600),T(600),R(600) ; Complex zo,xpol,ypol ; Real*8 b
    Common uin ; Common /ts/ zo,Txm,Tym,Rx,Ry,Rxm,Rym
c Initializing Parameters
    Call Initialize(xpol,ypol,Erange,Trange,devE0,devB0,zo,sinBragg,b,fconv,Npts,iflg)
    uin(1,1) = xpol ; uin(3,1) = ypol ; uin(2,1) = 0.0 ; uin(4,1) = 0.0
    If(iflg .Eq. 1) Then  ; delE0 = Erange/(npts-1) ; devE = devE0 - Erange/2.0 - delE0 ; devB = devB0
    Else ;                  delth = Trange/(npts-1) ; devB = devB0 - Trange/2.0 - delth  ; devE = devE0
    Endif
    Do 1 KK=1,npts
      If(iflg .Eq. 1) Then ; devE = devE + delE0 ; Freq(kk) = devE*fconv
      Else                 ; devB = devB + delth
      Endif
1     Call Dispersion(devB,devE,R(kk),T(kk),b,kk)
        ===> Call a Fast Fourier Transform Routine to take the Fourier Transform of Rx,Ry having abscissa
             points contained in the array Freq  ===>  This gives the Reflected Time Spectrum
    End
*****************************************************************************************************************
    Subroutine Dispersion(devB,devE,R,T,b,i)
c This subroutine solves the Dispersion equation for Dynamical Diffraction
    Parameter (n1 = 600)
    Complex w(4),g(4,4),e(4),Txm(n1),Tym(n1),Rx(n1),Ry(n1),Rxm(n1),Rym(n1),Tx(n1),Ty(n1)
    Real gr(4,4),gi(4,4),vr(4,4),vi(4,4),wr(4),wi(4),fv1(4),fv2(4),fv3(4),thick(4) ; Complex zo ; Real*8 b
    Common /ts/ zo,Txm,Tym,Rx,Ry,Rxm,Rym ; Common /disp/ e,g,thick
c Initializing Parameters
    n = 4  !order of g matrix ; nm = 4  !rows of g matrix ; matz = 1  !compute eigenvalues and eigenvectors
        ===> Set Tx(i),Ty(i),Rx(i),Ry(i),Rxm(i),Rym(i),Txm(i),Tym(i) to zero
    Call StrFact(devB,devE,b,g)  ! Scattering Amplitude Computation
c Computation of Eigenvalues (returned in w) and Eigenvectors (returned in g) of g-matrix.
    Call Cgg(nm,n,g,matz,w,fv1,fv2,fv3,gr,gi,vr,vi,wr,wi,ierr)
   Do L=1,n
c Thick crystal approx. is used to take care of floating point overflow problem.  Note that the conditional can be
c true only in the Bragg case
      If(Real(zo*w(l)) .Gt. 72.0) Then ; thick(l) = 0.0          ; e(l) = 1.0
      Else                             ; e(l) = Cexp(zo*w(l))  ; thick(l) = 1.0
      Endif
    Enddo
c Computation of Transmission and Reflection Coefficients
    Call TandR_coeff(Tx(i),Ty(i),Txm(i),Tym(i),Rx(i),Ry(i),Rxm(i),Rym(i),b)
    T = Txm(i)*Conjg(Txm(i)) + Tym(i)*Conjg(Tym(i))
    If(b .Lt. 0.0) Then ; R = Rx(i)*Conjg(Rx(i)) + Ry(i)*Conjg(Ry(i))                ! Bragg Case
    Else ;                R = Rxm(i)*Conjg(Rxm(i)) + Rym(i)*Conjg(Rym(i))          ! Laue Case
    Endif
    Return
*****************************************************************************************************************
    Subroutine TandR_coeff(Tx,Ty,Txm,Tym,Rx,Ry,Rxm,Rym,b)
    Complex e(4),Bc(4,4),uin(4,1),x(4,1),aa(4,4),v(4,4),D10xx(4),D00yx(4),D10yx(4),D00xx(4),
   1        ex(4),Tx,Ty,Rx,Ry,Txm,Tym,Rxm,Rym,atx,aty,arx,ary,norm
    Real thick(4) ; Real*8 b
    Common uin ; Common /disp/ e,v,thick
    n = 4     !order of Bc-matrix ; nm = 4     !rows of Bc-matrix ; nr = 1   !columns of x and uin arrays
    If(b .Lt. 0.0) Then
      Do 1 J=1,4          ! BRAGG CASE
```

```
1       ex(j) = e(j)
      Else
        Do 5 J=1,4              ! LAUE CASE
5       ex(j) = 1.0
      Endif
      Do 15 J=1,4
        Do K=1,4
          If(Cabs(v(k,j)) .Gt. 1.0e-20) Then ; norm = v(k,j) ; GoTo 10
        Endif
      Enddo
10    D00xx(j) = v(1,j)/norm      ; D10xx(j) = v(2,j)/norm    ; D00yx(j) = v(3,j)/norm      ; D10yx(j) = v(4,j)/norm
15    Bc(1,j) = D00xx(j)*thick(j) ; Bc(2,j) = ex(j)*D10xx(j) ; Bc(3,j) = D00yx(j)*thick(j) ; Bc(4,j) = ex(j)*D10yx(j)
c Boundary Condition Constraints--Evaluation of Simultaneous Equations: Bc*x = uin
      Call Clineq(Bc,uin,x,nm,n,nr,aa,ierr)  ! Bc*x = uin computation
c Computation of Tx,Ty,Ry,Rx by adding up all eigen amplitudes
      Do 20 K=1,4
        atx = x(k,nr)*D00xx(k) ; arx = x(k,nr)*D10xx(k)*thick(k)
        aty = x(k,nr)*D00yx(k) ; ary = x(k,nr)*D10yx(k)*thick(k)
        If(b .Lt. 0.0) Then ;   Rx = Rx + arx          ; Ry = Ry + ary                ! BRAGG CASE
        Else                ; Rxm = Rxm + arx*e(k) ; Rym = Rym + ary*e(k)          ! LAUE CASE
        Endif
20    Txm = Txm + atx*e(k) ; Tym = Tym + aty*e(k)
      Return
*****************************************************************************************************************
      Subroutine Initialize(xpol,ypol,Erange,Trange,devE0,devB0,zo,snBrgg,b,fconv,npts,iflg)
c This Subroutine Receives and Computes the Initialization Factors needed to Calculate Nuclear and
c Photoelectric Structure Factors and their associated Polarization Matrices
c VARIABLES:  (See ORIENT_CRYST Subroutine for more comments on variables)
c U = Net Orientation Matrix ; Erange = Spread of Energy to be Examined (eV) ; Trange = Spread of Angles to
c be Examined (radians) ; devE0,devB0 = Central Deviation Energy (eV) and Angle (radians) ; Npts = # of points
c of Angle or Energy scan ; Nptsi = # of integration points; iflg  = 0 --> angular scan, 1 --> Energy scan
c con = Relative Concentration of resonant nuclei ; DW = Debye Waller Factor for Photoelectric Scattering
c LM = Lamb-Mossbauer Factor for Nuclear Scattering ; efg = Electric Field Gradient direction ; to = Thickness
c of Crystal (cm) ; Z = # of Nuclei per site per unit cell ; QQ = Quadrupole Shift (mm/sec) ; isomer = Isomer
c Shift (mm/sec)  Hint = Internal Magnetic Field (gauss) ; spindp = Spin Dipolar Anisotropic Field (gauss)
c canting = canting angle (deg) ; zo = -ii*k*to/sinBragg , k = wavenumber ; xpol,ypol = Horizontal (Sigma) and
c Vertical (Pi) Polarization factor ; Hz = magnetic field direction in Lab coordinate system
c     Pjk(x,y) = Polarization matrix for Photoelectric scattering
c Yijk(n,x,y) = Polarization matrix element where:  x,y = polarizations
c                 i =  mg - me  = difference in quantum level between ground state and excited state
c                   = 0,1,or -1 for dipole transitions
c               j,k = 0 or 1  where 0 = transmission channel,  1 = reflection channel
c                 n = 1 for incoming photon,  2 for diffracted or scattered photon
c Eigenvector(x,y,l,iw,isite,igmn) = Scattered Photon Amplitude
c Eigenvalue(l,iw,isite) = Scattered Photon Energy
c                 isite = Particular Cluster of atoms within unit cell that have same internal field parameters
c                     l = index for ground  state quantum level  ; iw = index for excited state quantum level
c               igmn = 1 -> g00, 2 -> g10, 3 -> g01, 4 -> g11          gmn is proportional to the scattering tensor
c                 x,y = polarizations elements of gmn(x,y)          (see comments in STRFACT)
c NOTE:
c (1) Incoming Beam (for Zero Bragg angle) is in the positive Lab_y direction
c       K-incident = (cosBragg)y_Lab - (sinBragg)z_Lab  ; K-diffracted = (cosBragg)y_Lab + (sinBragg)z_Lab
c (2) The Quantum axis in this program is the Internal Magnetic field direction.
c (3) Initially, Hz is the External Magnetic Field Direction in the LAB coordinate system when hp & hs
c       directions are known.  Later, Hz is changed to point in the Internal Magnetic field direction.
c NEED:
c    (1)  Data File Called nuclear.dat (see read statements for variables needed)
c    (2)  Data File Called atompos.dat -- this contains hyperfine information and unit cell positions of the nuclei
c LINK:  Link with EWALD, ORIENT_CRYST, ELECTSTRFACT, SPLITTING
      Complex Y000(2,2,2),Y010(2,2,2),Y001(2,2,2),Y011(2,2,2),Y100(2,2,2),Y110(2,2,2),Y101(2,2,2),
     1        Y111(2,2,2),F0(15),P00(2,2),P01(2,2),P10(2,2),P11(2,2),FH(15),EigenvectorIg(4,4),
     2        EigenvectorIe(4,4),F_H(15),EigenvalueIg(4),Eigenvaluele(4),Eigenvector(2,2,2,4,15,4)
      Real*8 a(3),alpha(3),hp(3),hs(3),h(3),S(3),U(3,3),pii(3),pif(3),sigmai(3),sigmaf(3),Ki(3),Kf(3),
     1       Hz(3),HzLab(3),Hx(3),Hy(3),efg(3),efgLab(3)
```

```
      Real Eigenvalue(2,4,15),fv0(4),fv1(4),fv2(4),fv3(4),d1(4,4),d2(4,4),d3(4,4),d4(4,4),d5(4),d6(4)
      Real*8 pi,rad,c,hbar,hbarc,sinBragg,Vo,phiKi,phiH,norm,beta,gamma,Ee,gamma0,psi,canting,b,rx,ry,rw
     Complex ii,Go,xpol,ypol,zo  ; Real Ie,Ig,Lambda,isomer,LM      ; Character Crystal*10
     Common /stup/ hbarc,sinBragg,Vo,phiKi,phiH,psi,Ki,Kf,gamma0 ; Common /init/ sin2Brgg,sinBrgg2_E0
     Common /strf/ P00,P01,P10,P11,Go,Eigenvector,Eigenvalue     ; Common /Bfield/ Hz,HzLab,Hx,Hy
     Common /conv/ rad,pi,ii      ; Common /site/ isites
          ===> Read in from nuclear.dat file: Crystal;  a;  alpha; Ee, to;  iflg, Npts;  Erange, devB0;
                          Trange, devE0;  hp;  hs;  S;  Hz;  h;  phiH, phiK, psi;  con, LM;  DW;
                          xpolr, xpoli;  ypolr, ypoli
     ii = (0.0,1.0) ; pi = Dacos(-1.0d0) ; rad = pi/180.0d0 ; c = 2.99792d10  !Speed of Light (cm/sec)
     hbar = 6.58217d-16  !Planck Constant (eV-sec)        ; Re = 2.817938e-13 !Classical Electron Radius (cm)
     unu = 3.15245e-12  !Nuclear Magneton (eV/Gauss) ; uex = -0.1549  !Magnetic Moment of Excited State (nm)
     ugr = 0.09024  !Magnetic Moment of Ground State.(nm) ; Ttot = 140.95e-9  !Total Lifetime (sec)
     Alp = 8.23  !Internal Conversion Coefficient                ; Ig = 1.0/2.0 !Ground State Nuclear Energy Level
     Ie = 3.0/2.0 !First Excited State Nucl. Level      ; CG13 = Sqrt(1.0/3.0) !Clebsch Gordan Coeff. for Lines 3,4
     CG23 = Sqrt(4.0/3.0) !Clebsch Gordan Coeff. for Lines 2,5 (Sqrt(2) Polarization Factor added)
     CG11 = 1.0 !Clebsch Gordan Coeff. for Lines 1,6          ; Trad  = Ttot*(1.0 + Alp)  !Radiative Lifetime (sec)
     hbarc = hbar*c ; Go   = ii*hbar/(2.0*Ttot)                ; fconv = 1.0/(2.0*pi*hbar)  ; Polfac = 3.0/(16.0*pi)
c Normalizing polarizations to unity
     xpol = Cmplx(xpolr,xpoli) ; ypol = Cmplx(ypolr,ypoli)
     norm = Csqrt(xpol*Conjg(xpol) + ypol*Conjg(ypol)) ; xpol = xpol/norm ; ypol = ypol/norm
c Set-up Crystal Orientation for Diffraction.
      Call Orient_cryst(Ee,a,alpha,hp,hs,h,S,U,sigmai,pii,sigmaf,pif,b)
          Hzlab(1) = Hz(1) ; Hzlab(2) = Hz(2) ; Hzlab(3) = Hz(3)
     Coeff  = -4.0*pi**2*LM*con*Polfac/((2.0*Ig + 1.0)*(Trad/hbar)*(Ee/hbarc)**3*Vo)
     eCoeff = -2.0*pi*Re*hbarc**2/(Ee**2*Vo)
     sin2Brgg = 2.0*sinBragg*Dsqrt(1.0 - sinBragg**2) ; sinBrgg2_E0 = sinBragg**2/Ee
     zo = -ii*Ee*to/(hbarc*gamma0) ; Lambda = 2.0*pi*hbarc/Ee ; snBrgg = sinBragg
          ===> Read in from atompos.dat file:  isites
     Do 10 isite=1,isites
          ===> Read in from atompos.dat file:  efg;  QQ, Hint;  isomer, spindp;  canting
       e2qQ = 2.0*QQ*Ee/(c*10.0) ; isomer = isomer*Ee/(c*10.0)
c Construct basis of quantum coordinate system where the magnetic field direction is the z-axis
          ===> Call YIG_basis(Hzlab,Kf,Ki,Hint,Hx,Hy,Hz)  when Crystal is YIG
c                          !Incoming Beam Hits Plane from Above; Scattered beam travels in:
      Call Polarmat(pii,sigmai,pii,sigmai,Ki,Ki,Y000,Y100,P00)          !transmission channel.
      Call Polarmat(pii,sigmai,pif,sigmaf,Ki,Kf,Y010,Y110,P10)          !reflection channel.
c                          !Incoming Beam Hits Plane from Below; Scattered beam travels in:
      Call Polarmat(pif,sigmaf,pii,sigmai,Kf,Ki,Y001,Y101,P01)          !transmission channel.
      Call Polarmat(pif,sigmaf,pif,sigmaf,Kf,Kf,Y011,Y111,P11)          !reflection channel.
c Determining Polar Angle Beta and Azimuthal Phi Angle Between Electric Field Gradient and Quantum z-axis
      Call Mv(U,efg,efgLab)          !Transforming efg to Lab coord. system  ; Call Dot(efgLab,efgLab,norm)
     Do 1 I=1,3
 1     efgLab(i) = efgLab(i)/Dsqrt(norm)
      Call Polar(efgLab,Hx,Hy,Hz,beta,gamma) ; Hint = Hint + spindp*(3.0*Dcos(beta)**2 - 1.0)
c Computation of Eigenvectors and Eigenvalues
      ng = 2.0*Ig + 1.01  ; ne = 2.0*Ie + 1.01
       Call Splitting(alph,beta,gamma,eta,Ig,e2qQ,Hint,ugr,unu,EigenvalueIg,EigenvectorIg,ng,
  +              fv0,fv1,fv2,fv3,d1,d2,d3,d4,d5,d6,4)
       Call Splitting(alph,beta,gamma,eta,Ie,e2qQ,Hint,uex,unu,Eigenvaluele,Eigenvectorle,ne,
  +              fv0,fv1,fv2,fv3,d1,d2,d3,d4,d5,d6,4)
c Nuclear Geometrical Structure Factor Calculation for H and -H
          ===> Read in from atompos.dat file:  Z
      Do 5 I=1,Z
          ===> Read in from atompos.dat file:  rx, ry, rw       !Coordinate positions of atoms in unit cell
 5      FH(isite) = FH(isite) + Cdexp(ii*2.0*pi*(h(1)*rx + h(2)*ry + h(3)*rw))
      F_H(isite) = Conjg(FH(isite)) ; F0(isite) = Z
c Computation of Nuclear Scattering Amplitude of Photon
      Do 10 iw=1,ne
         Call Polarmix(Eigenvector,Eigenvectorle,CG11,CG23,CG13,Y000,Y100,Coeff*F0(isite),isite,iw,1)
         Call Polarmix(Eigenvector,Eigenvectorle,CG11,CG23,CG13,Y010,Y110,Coeff*FH(isite),isite,iw,2)
         Call Polarmix(Eigenvector,Eigenvectorle,CG11,CG23,CG13,Y001,Y101,Coeff*F_H(isite),isite,iw,3)
         Call Polarmix(Eigenvector,Eigenvectorle,CG11,CG23,CG13,Y011,Y111,Coeff*F0(isite),isite,iw,4)
        If(Real(Eigenvectorig(1,1)) .Gt. 0.0) Then
```

```
c +1/2 corresponds to first eigenvalue of Ground State
          Eigenvalue(1,iw,isite) = Eigenvaluele(iw) - Eigenvalueig(1) + isomer
          Eigenvalue(2,iw,isite) = Eigenvaluele(iw) - Eigenvalueig(2) + isomer
        Else
c +1/2 corresponds to second eigenvalue of Ground State
          Eigenvalue(1,iw,isite) = Eigenvaluele(iw) - Eigenvalueig(2) + isomer
          Eigenvalue(2,iw,isite) = Eigenvaluele(iw) - Eigenvalueig(1) + isomer
        Endif
 10 Continue
c Electronic Structure Factor Calculation
     Call ElectStrFact(Crystal,h(1),h(2),h(3),sinBragg,Lambda,DW,FH(isite),F_H(isite),F0(isite))
    Do 15 N=1,2
      Do 15 M=1,2                    !Photoelectric Scattering Amplitude
        P00(m,n) = eCoeff*F0(isite)*P00(m,n)   ; P10(m,n) = eCoeff*FH(isite)*P10(m,n)
 15   P01(m,n) = eCoeff*F_H(isite)*P01(m,n) ; P11(m,n) = eCoeff*F0(isite)*P11(m,n)
    Return
*****************************************************************************************************************
     Subroutine StrFact(devB,devE,b,g)
c This Subroutine Computes the Scattering Elements of the Dispersion Equation for Dynamical Diffraction
c For the 2x2 matrices: element (1,1) = xx, (1,2) = xy ; (2,1) = yx, (2,2) = yy
c In this Program : x = sigma polarization component ; y = pi polarization component
c VARIABLES:   (see INITIALIZE comments)
c  alpha = deviation from bragg parameter ; b = asymmetry parameter
      Complex g(4,4),g00(2,2),g11(2,2),g01(2,2),g10(2,2),gg00(2,2),gg11(2,2),gg01(2,2),gg10(2,2),P00(2,2),
     1          P01(2,2),P10(2,2),P11(2,2),Eigenvector(2,2,2,4,15,4),Res,ResJ,Go
     Real*8 b ; Real Eigenvalue(2,4,15)
     Common /init/ sin2Brgg,sinBrgg2_E0 ; Common /strf/ P00,P01,P10,P11,Go,Eigenvector,Eigenvalue
     Common /site/ isites
     Res = devE + Go   !Resonance Denominator Term
c Incoming Beam Hits Plane from Above; Scattered beam travels in:
c    g00 ==> transmission channel ; g10 ==> reflection  channel
c Incoming Beam Hits Plane from Below; Scattered beam travels in:
c    g01 ==> transmission channel ; g11 ==> reflection  channel
    Do 1 N=1,2
      Do 1 M=1,2
 1      gg00(m,n) = P00(m,n) ; gg10(m,n) = P10(m,n) ; gg01(m,n) = P01(m,n) ; gg11(m,n) = P11(m,n)
    Do 5 I=1,isites
      Do 5 iw=1,4
        Do 5 J=1,2
          ResJ = Res - Eigenvalue(j,iw,i)
         Do 5 N=1,2
           Do 5 M=1,2
              gg00(m,n) = gg00(m,n) + Eigenvector(m,n,j,iw,i,1)/ResJ
              gg10(m,n) = gg10(m,n) + Eigenvector(m,n,j,iw,i,2)/ResJ
              gg01(m,n) = gg01(m,n) + Eigenvector(m,n,j,iw,i,3)/ResJ
 5            gg11(m,n) = gg11(m,n) + Eigenvector(m,n,j,iw,i,4)/ResJ
    alpha = -2.0*sin2Brgg*devB ; e1   = b*alpha/2.0
c Construction of g-matrix pertaining to dynamical diffraction formula
    g(1,1) = gg00(1,1)    ; g(1,2) = gg01(1,1)          ; g(1,3) = gg00(1,2)    ; g(1,4) = gg01(1,2)
    g(2,1) = b*gg10(1,1) ; g(2,2) = b*gg11(1,1) - e1 ; g(2,3) = b*gg10(1,2) ; g(2,4) = b*gg11(1,2)
    g(3,1) = gg00(2,1)    ; g(3,2) = gg01(2,1)          ; g(3,3) = gg00(2,2)    ; g(3,4) = gg01(2,2)
    g(4,1) = b*gg10(2,1) ; g(4,2) = b*gg11(2,1)       ; g(4,3) = b*gg10(2,2) ; g(4,4) = b*gg11(2,2) - e1
    Return
*****************************************************************************************************************
     Subroutine Polarmat(pii,sigmai,pif,sigmaf,Ki,Kf,Y0,Y1,P)
c  Polarmat Computes Polarization Mixing Matrices
c  VARIABLES:   (See INITIALIZE subroutine for more comments on variables)
c Ki(f) = incoming(diffracted) photon direction (k-unit vector)
c coski(kf) = angle between incoming(diffracted) photon direction and quantum axis
c phiki(kf) = azimuthal phi angle of incoming(diffracted) photon direction in quantum spherical coord. system
c thetai(f) = theta unit vector of incoming(diffracted) photon k-vector in quantum spherical coordinate system
c phii(f)   = phi unit vector of incoming(diffracted) photon k-vector in quantum spherical coordinate system
c sigmai(f) = sigma polarization unit vector of incoming(diffracted) photon ; pii(f) = pi polarization unit vector of
c incoming(diffracted) photon ; Hx,Hy,Hz  = Quantum Basis unit vectors in Lab coord. system
```

```
c Y10i(f)  = Vector Spherical Harmonic for J=1,L=1,M=0 ; Y11i(f)  = Vector Spherical Harmonic for J=1,L=1,M=1
c P  = Polarization matrix for Photoelectric scattering
     Complex Y0(2,2,2),Y1(2,2,2),Y10i(3),Y10f(3),Y11i(3),Y11f(3),P(2,2),ii
     Real*8 Hz(3),Hx(3),Hy(3),Ki(3),Kf(3),sigmai(3),sigmaf(3),pii(3),pif(3),phii(3),phif(3),thetai(3),thetaf(3),
    1       HzLab(3),rad,pi,norm,Pss,Psp,Pps,Ppp,phiki,phikf,theta,sinki,sinkf,coski,coskf
     Common /Bfield/ Hz,HzLab,Hx,Hy ; Common /site/ isites ; Common /conv/ rad,pi,ii
c Nuclear Angular Factors
     Call Dot(Hz,Ki,coski)                  ; Call Dot(Hz,Kf,coskf)       ; sinki = Dsqrt(1.0d0 - coski**2)
     sinkf = Dsqrt(1.0d0 - coskf**2)        ; Call Polar(Ki,Hx,Hy,Hz,theta,phiki)
     Call Polar(Kf,Hx,Hy,Hz,theta,phikf) ; Call Cross(Hz,Ki,phii,norm)
     If(norm .Gt. 1.0d-30) Then  ; Call Cross(phii,Ki,thetai,norm)
     Else
       Do 1 I=1,3                                !If Ki //-H  then phi and theta unit vectors
 1       phii(i) = sigmai(i) ; thetai(i) = pii(i)    !are set to sigma and pi polarizations
     Endif
     Call Cross(Hz,Kf,phif,norm)
     If(norm .Gt. 1.0d-30) Then  ; Call Cross(phif,Kf,thetaf,norm)
     Else
       Do 5 I=1,3
 5       phif(i) = sigmaf(i) ; thetaf(i) = pif(i)     ! If Kf // H then do the same as stated above
     Endif
     Do 10 I=1,3
       Y10i(i) = ii*sinki*phii(i) ; Y10f(i) = ii*sinkf*phif(i) ; Y11i(i) = (thetai(i) + ii*coski*phii(i))*Cdexp(ii*phiki)
 10  Y11f(i) = (thetaf(i) + ii*coskf*phif(i))*Cdexp(ii*phikf)
c Construction of Polarization Matrices
c M = 0
     Call Cdot(Y10i,sigmai,Y0(1,1,1),1) ; Call Cdot(Y10i,pii,Y0(1,2,1),1) ; Call Cdot(Y10f,sigmaf,Y0(2,1,1),0)
     Call Cdot(Y10f,pif,Y0(2,1,2),0)    ; Y0(1,1,2) = Y0(1,1,1) ; Y0(1,2,2) = Y0(1,2,1) ; Y0(2,2,1) = Y0(2,1,1)
     Y0(2,2,2) = Y0(2,1,2)
c M = 1
     Call Cdot(Y11i,sigmai,Y1(1,1,1),1) ; Call Cdot(Y11i,pii,Y1(1,2,1),1) ; Call Cdot(Y11f,sigmaf,Y1(2,1,1),0)
     Call Cdot(Y11f,pif,Y1(2,1,2),0)    ; Y1(1,1,2) = Y1(1,1,1) ; Y1(1,2,2) = Y1(1,2,1) ; Y1(2,2,1) = Y1(2,1,1)
     Y1(2,2,2) = Y1(2,1,2)
c Electronic Angular Factors
     Call Dot(sigmai,sigmaf,Pss) ; Call Dot(sigmai,pif,Psp) ; Call Dot(pii,sigmaf,Pps) ; Call Dot(pii,pif,Ppp)
     P(1,1) = Pss                ; P(1,2) = Psp             ; P(2,1) = Pps             ; P(2,2) = Ppp
     Return
*****************************************************************************************************************
     Subroutine Polarmix(E,Ele,CG1,CG0,CG_1,Y0,Y1,F,isite,iw,igmn)
c  Polarmix Computes Scattering Tensor Elements of Dispersion Equation
c  VARIABLES: (See Comments in Subroutine INITIALIZE)
c  NOTE:   (1) Spherical Harmonic Y1 = Y(M=+1) = Complex Conjugate Y(M=-1)
       Complex E(2,2,2,4,15,4),Ele(4,4),Y0(2,2,2),Y1(2,2,2),F,Ei1,Ef1,Ei2,Ef2
     Do 1 N=1,2                                  ! M = ±2 Not allowed for magnetic dipole scattering
       Do 1 M=1,2
c +1/2 ground state amplitudes
         Ei1 = CG1*Conjg(Ele(1,iw))*Y1(1,m,n) + CG0*Conjg(Ele(2,iw))*Y0(1,m,n) +
    +          CG_1*Conjg(Ele(3,iw))*Conjg(Y1(1,m,n))
         Ef1 = CG1*Ele(1,iw)*Y1(2,m,n) + CG0*Ele(2,iw)*Y0(2,m,n) + CG_1*Ele(3,iw)*Conjg(Y1(2,m,n))
c -1/2 ground state amplitudes
         Ei2 = CG_1*Conjg(Ele(2,iw))*Y1(1,m,n) + CG0*Conjg(Ele(3,iw))*Y0(1,m,n) +
    +          CG1*Conjg(Ele(4,iw))*Conjg(Y1(1,m,n))
         Ef2 = CG_1*Ele(2,iw)*Y1(2,m,n) + CG0*Ele(3,iw)*Y0(2,m,n) + CG1*Ele(4,iw)*Conjg(Y1(2,m,n))
         E(m,n,1,iw,isite,igmn) = F*(Ei1*Ef1)   ! +1/2
 1       E(m,n,2,iw,isite,igmn) = F*(Ei2*Ef2)   ! -1/2
     Return
*****************************************************************************************************************
     Subroutine YIG_basis(Hzlab,Kf,Ki,Hint,Hx,Hy,Hz)
c This subroutine Constructs the Quantum Coordinate System for YIG or similiar systems
c  The Hx-direction is perpendicular to both Hz and the diffracted wavevector.
     Real*8 Hzlab(3),Hx(3),Hy(3),Hz(3),Kf(3),Ki(3),norm
     If(Hint .Lt. 0.0) Then
       Do 1 I=1,3
 1       Hz(i) = -Hzlab(i)
```

```
      Hint = -Hint
    Else
      Do 5 I=1,3
5       Hz(i) = Hzlab(i)
    Endif
c Hx is perpendicular to Hz and Kf; however if Hz is parallel to Kf, Hx is perpendicular to Hz and Ki.
    Call Cross(Hz,Kf,Hx,norm) ; If(norm .Lt. 1.0e-3) Call Cross(Hz,Ki,Hx,norm) ; Call Cross(Hz,Hx,Hy,norm)
    Return
*****************************************************************************************************************
    Subroutine FeBO3_basis(U,canting,Hzlab,Kf,Ki,Hint,Hx,Hy,Hz)
c This subroutine Constructs the Quantum Coordinate System for FeBO3 or similiar systems
*****************************************************************************************************************
    Subroutine Cdot(u,v,w,i)
c This Subroutine computes the Dot product of a Complex vector "u" and a real vector "v". It returns the dot
c product "w".
c  i = 0  ==> w = u*ComplexConjugate(v) = u*v  for v real
c  i = 1  ==> w = v*ComplexConjugate(u)
*****************************************************************************************************************
    Subroutine Splitting(alpha,beta,gamma,eta,I,e2qQ,Ho,u,un,Val,Ham,nH,M,fv1,fv2,fv3,hr,hi,vr,vi,wr,wi,L)
c  This Subroutine determines the Energy Eigenvalues and Eigenvectors for a Nuclear State that has both Static
c Electric Quadrupole and Magnetic Dipole Interaction
c VARIABLES:
c  Ham Contains the Eigenvectors -- original Hamiltonian matrix is destroyed by Subroutine CGG
c  Val Contains the Eigenvalues  ; nH = Order of Hamiltonian Ham(i,j)  ; I = Nuclear Energy Level
c  un = Nuclear Magneton (Ev/Gauss)  ; beta  = angle between Electric Field Gradient and Magnetic Field
c  gamma = azimuthal angle between Electric Field Gradient and Magnetic Field (radians)
c  alpha = Third Euler Angle needed when the Electric Quadrupole Interaction is non-axially symmetric (radians)
c  eta = (Vxx - Vyy)/Vzz --> the asymmetry parameter which describes the deviation of the Electric Field
c  Gradient from axial symmetry.  ; e2qQ  = Electric Quadrupole Splitting Factor e**2*q*Q  (eV)
c  Ho = External Magnetic Field Strength (Gauss)  ; u = Magnetic Moment (nuclear magnetons)
c  LINKING:  Need to link with Subroutine EIS_LIN_PACK
    Complex Val(L),Ham(L,L),ii,exp2a,expg,exp2g,Hmm1,Hmm_1,Hmm2,Hmm_2
     Real M(L),fv1(L),fv2(L),fv3(L),hr(L,L),hi(L,L),vr(L,L),vi(L,L),wr(L),wi(L),I
    ii = (0.0,1.0)  ; nlevels = 2.0*I + 1.0                ; wE = 0.0  ; wH = Ho*u*un/I
    If(I .Ne. 0.5) wE = e2qQ/(4.0*I*(2.0*I - 1.0))       ; y = wH    ; z = wE
    Cos2a = Cos(2.0*alpha)      ; Cosb = Cos(beta)         ; Sinb = Sin(beta)
    Exp2a = Cexp(ii*2.0*alpha) ; Expg = Cexp(ii*gamma) ; Exp2g = Cexp(ii*2.0*gamma)
    Hmm = 0.5*z*(3.0*cosb**2 - 1.0 + eta*sinb**2*cos2a)
    Hmm1 = 1.5*z*sinb*(cosb - (eta/6.0)*((1.0 + cosb)*exp2a - (1.0 - cosb)*Conjg(exp2a)))*expg
    Hmm_1 = 1.5*z*sinb*(cosb + (eta/6.0)*((1.0 - cosb)*exp2a - (1.0 + cosb)*Conjg(exp2a)))*Conjg(expg)
    Hmm2 = 0.75*z*(sinb**2 + (eta/6.0)*((1.0 + cosb)**2*exp2a + (1.0 - cosb)**2*Conjg(exp2a)))*exp2g
    Hmm_2 = 0.75*z*(sinb**2 + (eta/6.0)*((1.0 - cosb)**2*exp2a +
   +              (1.0 + cosb)**2*Conjg(exp2a)))*Conjg(exp2g)
    Do 10 J=1,nlevels
     M(j) = I - (j-1)
     Do 10 K=1,nlevels
10    Ham(k,j) = 0.0
    N = 1
    Do 15 K=N,nlevels
15   Ham(k,k) = -y*M(k) + Hmm*(3.0*M(k)**2 - I*(I + 1.0))
    N = N + 1
    Do 20 K=N,nlevels
     Ham(k-1,k) = Hmm_1*(2.0*M(k-1) - 1.0)*Sqrt((I + M(k-1))*(I - M(k-1) + 1.0))
20   Ham(k,k-1) = Hmm1*(2.0*M(k) + 1.0)*Sqrt((I - M(k))*(I + M(k) + 1.0))
    N = N + 1
    Do 25 K=N,nlevels
     Ham(k-2,k) = Hmm_2*Sqrt((I - M(k-2) + 2.0)*(I - M(k-2) + 1.0)*(I + M(k-2))*(I + M(k-2) - 1.0))
25   Ham(k,k-2) = Hmm2*Sqrt((I + M(k) + 2.0)*(I + M(k) + 1.0)*(I - M(k))*(I - M(k) - 1.0))
    matz = 1   ! Eigenvalue and Eigenvector Calculation
    Call Cgg(L,nH,Ham,matz,Val,fv1,fv2,fv3,hr,hi,vr,vi,wr,wi,ierr)
    Return
*****************************************************************************************************************
DATAFILE   NUCLEAR.DAT
```

```
YIG                    ! Crystal Type
12.3797e-8,12.3797e-8,12.3797e-8  !Lattice spacings a,b,c (cm)
90.0,90.0,90.0                    !Lattice angles alpha,beta,gamma (deg)
14412.5,5.0e-4         ! Incoming photon energy(eV),Crystal thickness(cm)
1,400                  ! (iflg=1=Energy scan,iflg=0=Angle scan) ; # points
10.0e-7,65.0e-6        ! Energy range (Ev),deviation from Bragg (rad)
20.0e-6,-0.0e-7        ! Angle range (rad),deviation from incoming Energy (eV)
TWO RECIPROCAL LATTICE VECTORS, 1st is in LAB_z direction, 2nd is in the SCATTERING PLANE where
hs(dot)Kf > 0, Kf(dot)LAB y > 0.  LAB_x is perpendicular to SCATTERING PLANE.
 0. 0. 2.              ! Hp  Kp  Lp   Reciprocal Lattice vector in LAB_z direction
 1. 0. 0.              ! Hs  Ks  Ls   Reciprocal Lattice vector in scattering plane
 0. 0. 2.              ! Outward Surface Direction (in Reciprocal coordinates)
 0. 1. 0.              ! External Magnetic Field Direction (in LAB coordinates)
RECIPROCAL LATTICE VECTOR of desired reflection
 0. 0. 2.              ! H   K   L  Desired Reciprocal Lattice Vector
AZIMUTHAL ROTATIONS that preserve Bragg Condition. Two Rotations are made. The 1st is about H =
Reciprocal Lattice Vector, the 2nd is about Ki, and the 3rd is about H again
0.0,0.0,0.0            ! Azimuthal rotation about H,Ki,H=(H,K,L) (deg)
0.87,0.8               ! Nuclear: Relative Concentration; Lamb-Mossbauer factor
0.987                  ! Electronic: Debeye Waller factor
1.0,0.0                ! Horizontal Polarization of incoming Photon (real,imag)
0.0,0.0                ! Vertical Polarization of incoming Photon (real,imag)
        ! See INITIALIZE subroutine for a more detailed description of these parameters
*****************************************************************************************************************
DATAFILE  ATOMPOS.DAT
        This Data file contains the positions of the Fe57 atoms corresponding to various sites in YIG and the
         EFG directions of the iron atoms in the sites, and also associated hyperfine field parameters
             (Winkler, Phys.B,Condensed Matter,49,331,83)
$
7                      ! Number of Sites within Unit Cell
 D1-SITE Fe57 ATOMS   [100] SYMMETRY AXIS
 1. 0. 0.    ! Electric Field Gradient Direction [h k l]
 -0.89d0,-3.68d5    !Quadrupole Shift (mm/sec),Magnetic Field (gauss)
 0.0d0,0.0d0    !Isomer Shift (mm/sec),Spin Dipolar Anisotropy (gauss)
0.0d0    !Canting Angle (deg) ; 8    ! # of atoms in this site
Coordinate of Fe57 atoms within unit cell:
 0.375   0.0   0.25 ; 0.875   0.5   0.75 ; 0.625   0.5   0.25 ; 0.125   0.0   0.75
 0.625   0.0   0.75 ; 0.125   0.5   0.25 ; 0.375   0.5   0.75 ; 0.875   0.0   0.25
 D2-SITE Fe57 ATOMS   [010] SYMMETRY AXIS
 0. 1. 0. ; -0.89d0,-3.68d5 ; 0.0d0,0.0d0 ; 0.0d0 ; 8
 0.25   0.375   0.0 ; 0.75   0.125   0.0 ; 0.75   0.875   0.5 ; 0.25   0.625   0.5
 0.75   0.625   0.0 ; 0.25   0.875   0.0 ; 0.25   0.125   0.5 ; 0.75   0.375   0.5
 D3-SITE Fe57 ATOMS   [001] SYMMETRY AXIS
 0. 0. 1. ; -0.89d0,-3.68d5 ; 0.0d0,0.0d0 ; 0.0d0 ; 8
 0.0    0.25   0.375 ; 0.5    0.25   0.625 ; 0.0    0.75   0.125 ; 0.5    0.75   0.875
 0.0    0.75   0.625 ; 0.5    0.75   0.375 ; 0.0    0.25   0.875 ; 0.5    0.25   0.125
 A1-SITE Fe57 ATOMS   [111] SYMMETRY AXIS
 1. 1. 1. ; -0.41d0,4.40d5 ; 0.226d0,-0.035d5 ; 0.0d0 ; 4
 0.00   0.00   0.00 ; 0.25   0.25   0.25 ; 0.50   0.50   0.50 ; 0.75   0.75   0.75
 A2-SITE Fe57 ATOMS   [-111] SYMMETRY AXIS
-1. 1. 1. ; -0.41d0,4.40d5 ; 0.226d0,-0.035d5 ; 0.0d0 ; 4
 0.50   0.50   0.00 ; 0.75   0.25   0.75 ; 0.00   0.00   0.50 ; 0.25   0.75   0.25
 A3-SITE Fe57 ATOMS   [1-11] SYMMETRY AXIS
 1.-1. 1. ; -0.41d0,4.40d5 ; 0.226d0,-0.035d5 ; 0.0d0 ; 4
 0.00   0.50   0.50 ; 0.75   0.75   0.25 ; 0.50   0.00   0.00 ; 0.25   0.25   0.75
 A4-SITE Fe57 ATOMS   [-1-11] SYMMETRY AXIS
-1.-1. 1. ; -0.41d0,4.40d5 ; 0.226d0,-0.035d5 ; 0.0d0 ; 4
 0.50   0.00   0.50 ; 0.25   0.75   0.75 ; 0.00   0.50   0.00 ; 0.75   0.25   0.25
*****************************************************************************************************************
```

8.4 Boundary Conditions and the Thick Crystal Approximation

Since in general the linearized dispersion relations are not decoupled, the dispersion relation given by Eq. 7-4.1 must be modified to

$$\left(\mathbf{G}_{lin} - 2\varepsilon_0 \mathbf{I}\right) \cdot \mathbf{v} = 0 \tag{8-4.1}$$

where $\mathbf{G}_{lin}$ is given by Eq. 7-8.1. Finding the four eigenvectors

$$\mathbf{v}^{\ell} = \begin{pmatrix} T_x^{\ell} \\ R_x^{\ell} \\ T_y^{\ell} \\ R_y^{\ell} \end{pmatrix} \qquad (\ell = 1,\ldots,4) \tag{8-4.2}$$

allows the boundary condition equation, Eq. 7-4.30, to be solved by setting

$$T_x^{\ell} = D_1^{\ell} T_x^{\ell}, \quad R_x^{\ell} = D_2^{\ell} T_x^{\ell}, \quad T_y^{\ell} = D_3^{\ell} T_x^{\ell}, \quad R_y^{\ell} = D_4^{\ell} T_x^{\ell} \tag{8-4.3}$$

where

$$D_n^{\ell} = \left(v^{\ell}\right)_n / \left(v^{\ell}\right)_1 \tag{8-4.4}$$

and $\left(v^{\ell}\right)_n$ is the n^{th} component of $\mathbf{v}^{\ell}$. If $\left(v^{\ell}\right)_1$ is zero, then all of the eigenamplitudes can be expressed in terms of one of the nonzero eigenamplitudes in a similar fashion (that is, in terms of an amlitude other than T_x^{ℓ}). The boundary condition equation can then be explicitly written out as (for $\left(v^{\ell}\right)_1 \neq 0$)

$$\begin{pmatrix} 1 & 1 & 1 & 1 \\ D_2^1 e^{i\kappa^1 d} & D_2^2 e^{i\kappa^2 d} & D_2^3 e^{i\kappa^3 d} & D_2^4 e^{i\kappa^4 d} \\ D_3^1 & D_3^2 & D_3^3 & D_3^4 \\ D_4^1 e^{i\kappa^1 d} & D_4^2 e^{i\kappa^2 d} & D_4^3 e^{i\kappa^3 d} & D_4^4 e^{i\kappa^4 d} \end{pmatrix} \begin{pmatrix} T_x^1 \\ T_x^2 \\ T_x^3 \\ T_x^4 \end{pmatrix} = \begin{pmatrix} E_{0vx} \\ 0 \\ E_{0vy} \\ 0 \end{pmatrix} \tag{8-4.5}$$

where $\kappa^{\ell} = k_{0v}\varepsilon_0^{\ell}/\gamma_0$. This equation is solved by the subroutine TandR_coeff in the EWALD Fortran code.

When the exponential factor $e^{i\kappa^{\ell} d}$ in Eq. 8-4.5 becomes very large (for instance, too large for a computer to handle), numerical solutions can be found by applying a thick crystal approximation. Note that at the exit surface, the transmission channel field is

$$\mathbf{T}\left(\hat{\mathbf{n}} \cdot \mathbf{r} = d\right) = e^{i\mathbf{k}_{0v} \cdot \mathbf{r}} \sum_{l=1}^{4} \sum_{\alpha} T_{\alpha}^{l} e^{i\kappa^{l} d} \hat{\boldsymbol{\varepsilon}}_{\alpha}^{0}. \tag{8-4.6}$$

Then, if $e^{i\kappa^\ell d} \to \infty$, in order for the transmitted field to stay finite, T_α^ℓ must go to zero. This is the heart of the thick crystal approximation:

$$\left\{\begin{matrix} e^{i\kappa^\ell d} \to \infty \ , \quad T_\alpha^\ell \to 0 \\ T_\alpha^\ell e^{i\kappa^\ell d} \to \text{a finite quantity} \end{matrix}\right\}. \tag{8-4.7}$$

This approximation can then be used to modify the boundary condition equations. For instance, let κ^1 be the complex eigenwavenumber that gives rise to exponentially large numbers. Then the boundary value equation to be solved is

$$\begin{pmatrix} 0 & 1 & 1 & 1 \\ D_2^1 & D_2^2 e^{i\kappa^2 d} & D_2^3 e^{i\kappa^3 d} & D_2^4 e^{i\kappa^4 d} \\ 0 & D_3^2 & D_3^3 & D_3^4 \\ D_4^1 & D_4^2 e^{i\kappa^2 d} & D_4^3 e^{i\kappa^3 d} & D_4^4 e^{i\kappa^4 d} \end{pmatrix} \begin{pmatrix} T_x^1 e^{i\kappa^1 d} \\ T_x^2 \\ T_x^3 \\ T_x^4 \end{pmatrix} = \begin{pmatrix} E_{0vx} \\ 0 \\ E_{0vy} \\ 0 \end{pmatrix}. \tag{8-4.8}$$

In the subroutine Dispersion and TandR_coeff, the arrays thick and e keep track of which elements in the boundary condition matrix must be modified.

REFERENCES

[1] G. V. Smirnov, V. V. Sklyarevskii, R. A. Voskanyan, and A. N. Artem'ev, *JETP Lett.* **9**, 123 (1969).

[2] A. I. Chechin, N. V. Andronova, M. V. Zelepukhin, A. N. Artem'ev, and E. P. Stepanov, *JETP Lett.* **37**, 633 (1983).

[3] G. Faigel, D. P. Siddons, J. B. Hastings, P. E. Haustein, and J. R. Grover, *Phys. Rev. Lett.* **58**, 2699 (1987).

[4] S. Kikuta, Y. Yoda, Y. Kudo, K. Izumi, T. Ishikawa, C. K. Suzuki, H. Ohno, H. Takei, K. Nakayama, X. W. Zhang, T. Matsushita, S. Kishimoto, and M. Ando, *Jpn. J. App. Phys.* **30**, L 1686 (1991).

[5] P. P. Kovalenko, V. G. Labushkin, V. V. Rudenko, V. A. Sarkisyan, and V. N. Seleznev, *JETP Lett.* **26**, 85 (1977).

[6] G. V. Smirnov, V. V. Mostovoi, Y. V. Shvyd'ko, V. N. Seleznev, and V. V. Rudenko, *Sov. Phys. JETP* **51**, 603 (1980).

[7] U. van Bürck, G. V. Smirnov, R. L. Mössbauer, H. J. Maurus, and N. A.

Semioschkina, *J. Phys. C: Solid St. Phys.* **13**, 4511 (1980). ; U. van Bürck, R. L. Mössbauer, E. Gerdau, R. Rüffer, R. Hollatz, G. V. Smirnov, and J. P. Hannon, *Phys. Rev. Lett.* **59**, 355 (1987).

[8] E. Gerdau, R. Rüffer, H. Winkler, W. Tolksdorf, C. P. Klages, and J. P. Hannon, *Phys. Rev. Lett.* **54**, 835 (1985).

[9] J. Arthur, G. S. Brown, D. E. Brown, and S. L. Ruby, *Phys. Rev. Lett.* **63**, 1629 (1989).

[10] P. P. Kovalenko, V.G. Labushkin, A.K. Ovsepyan, E. R. Sarkisov, E.V. Smirnov, A. R. Prokopov, and V. N. Seleznev, *Sov. Phys. Solid State* **26**, 1849 (1984).

[11] A. I. Chumakov, G. V. Smirnov, M. V. Zelepukhin, U. van Bürck, E. Gerdau, R. Rüffer, and H. D. Rüter, *Hyp. Int.* **71**, 1341 (1992).

[12] P. J. Black and I. P. Duerdoth, *Proc. Phys. Soc.* **84**, 169 (1964).

[13] R. M. Mirzababaev, G. V. Smirnov, V. V. Sklyarevskii, A. N. Artemev, A. N. Izrailenko, and A. V. Babkov, *Phys. Lett.* **37A**, 441 (1971).

[14] V. S. Zasimov, R. N. Kuz'min, and A. Yu. Aleksandrov, *Sov. Phys. Solid State* **17**, 2044 (1976).

[15] V. K. Voitovetskii, I. L. Korsunskii, A. I. Novikov, and Y. F. Pazhin, *Sov. Phys. JETP* **27**, 729 (1968). ; V. K. Voitovetskii, I. L. Korsunskii, Y. F. Pazhin, and R. S. Silakov, *JETP Lett.* **12**, 212 (1970).

[16] V. A. Belyakov, *Sov. Phys. -Usp.* **18**, 267 (1975).

[17] R. W. G. Wyckoff, *Crystal Structures*, vol. 2 (Robert E. Krieger, Malabar, Florida, 1982)

[18] I. Bernal, C. W. Struck, and J. G. White, *Acta Cryst.* **16**, 849 (1963).

[19] R. Diehl, *Solid St. Commun.* **17**, 743 (1975).

[20] C. G. Shull, W. A. Strauser, and E. O. Wollan, *Phys. Rev.* **83**, 333 (1951).

[21] I. Dzyaloshinsky, *Phys. Chem. Solids* **4**, 241-255 (1958).

[22] M. P. Petrov, G. A. Smolensky, A. P. Paugurt, and S. A. Kizhaev, *Nuclear Magnetic Resonance and Magnetic Properties of* $FeBO_3$*-Type Crystals*, edited by J. C. D. Graham, J. J. Rhynes, Proceedings of the Seventeenth Conference on Magnetism and Magnetic Materials (AIP, New York, 1971), p. 379.

[23] M. Eibschutz and M. E. Lines, *Phys. Rev. B* **7**, 4907 (1973).

[24] M. Brunel and F. D. Bergevin, *Acta Cryst.* **A37**, 324 (1981).

[25] R. Nathans, S. J. Pickart, H. A. Alperin, and P. J. Brown, *Phys. Rev.* **136**, A 1641 (1964).

[26] G. V. Smirnov, V. V. Sklyarevskii, A. N. Artem'ev, and R. A. Voscanyan, *Phys. Lett.* **32A**, 532 (1970).

[27] G. V. Smirnov, Y. V. Shyvd'ko, and E. Realo, *JETP Lett.* **39**, 41 (1984).

[28] R. W. G. Wyckoff, *Crystal Structures*, vol. 3 (Robert E. Krieger, Malabar, Florida, 1982).

[29] D. M. Gualtieri, W. Lavender, and S. L. Ruby, *J. Appl. Phys.* **63**, 3795 (1988).

[30] H. Winkler, R. Eisberg, E. Alp, R. Rüffer, E. Gerdau, S. Lauer, A. X. Trautwein, M. Grodzicki, and A. Vera, *Z. Phys. B* **49**, 331 (1983).

[31] E. Gerdau and R. Ruffer, *Hyp. Int.* **27**, 59 (1986).

[32] J. Arthur, D. E. Brown, S. L. Ruby, G. S. Brown, and G. K. Shenoy, *J. Appl. Phys.* **67**, 5704 (1990).

[33] W. C. Hamilton, *International Tables for X-Ray Crystallography* , edited by J. A. Ibers and W. C. Hamilton (Kynoch Press, Birmingham, England, 1974), vol. 4, p. 275.

[34] J. S. Rollett, *Computing Methods in Crystallography* (Pergamon Press, Oxford, 1965).

[35] W. R. Busing and H. A. Levy, *Angle Calculations for 3- and 4-Circle X-Ray and Neutron Diffractometers,* ORNL Report 4056 (Oak Ridge National Laboratory, Oak Ridge, Tennessee, 1967).

[36] A. I. Borisenko and I. E. Tarapov, *Vector and Tensor Analysis with Applications* (Dover, New York, 1968).

[37] B. S. Garbow, EISPACK (Applied Mathematics Division of Argonne National Laboratory, Netlib%ANL-MCS.ARPA, 1983).

[38] C. Moler and J. Dongarra, LINPACK (Applied Mathematics Division of Argonne National Laboratory, Netlib%ANL-MCS.ARPA, 1978).

[39] W. H. Zachariasen, *Theory of X-Ray Diffraction in Crystals* (Dover, New York, 1945).

[40] B. W. Batterman and H. Cole, *Rev. Mod. Phys.* **36**, 681 (1964).

[41] A. M. Afanas'ev and Y. Kagan, *Sov. Phys. JETP* **21**, 215 (1965).

[42] E. O. Brigham, *The Fast Fourier Transform* (Prentice Hall, Englewood Cliffs, 1974).

[43] C. M. Lederer and V. S. Shirley, *Table of Isotopes* (Wiley, New York, 1978).

[44] P. R. Locher and S. Geschwind, *Phys. Rev.* **139**, A991 (1965).

[45] R. S. Preston, S. S. Hanna, and J. Heberle, *Phys. Rev.* **128**, 2207 (1962).

[46] C. H. MacGillavry and G. D. Rieck, *International Tables for X-Ray Crystallography* (Kynoch Press, Birmingham, England, 1968), vol. 3.

[47] B. E. Warren, *X-Ray Diffraction* (Dover, New York, 1990).

[48] D. T. Cromer and D. Liberman, *J. Chem. Phys.* **53**, 1891 (1970).

[49] W. H. McMaster, N. K. D. Grande, J. H. Mallett, J. H. Hubbell, and National Bureau of Standards, *Compilation of X-Ray Cross Sections*, UCRL Report 50174, Sec. III, Rev. 1 (Lawrence Radiation Laboratory, University of California, Livermore, Ca., 1969).

9. EXPERIMENTAL PROCEDURES

9.1 YIG Epitaxial Films on GGG

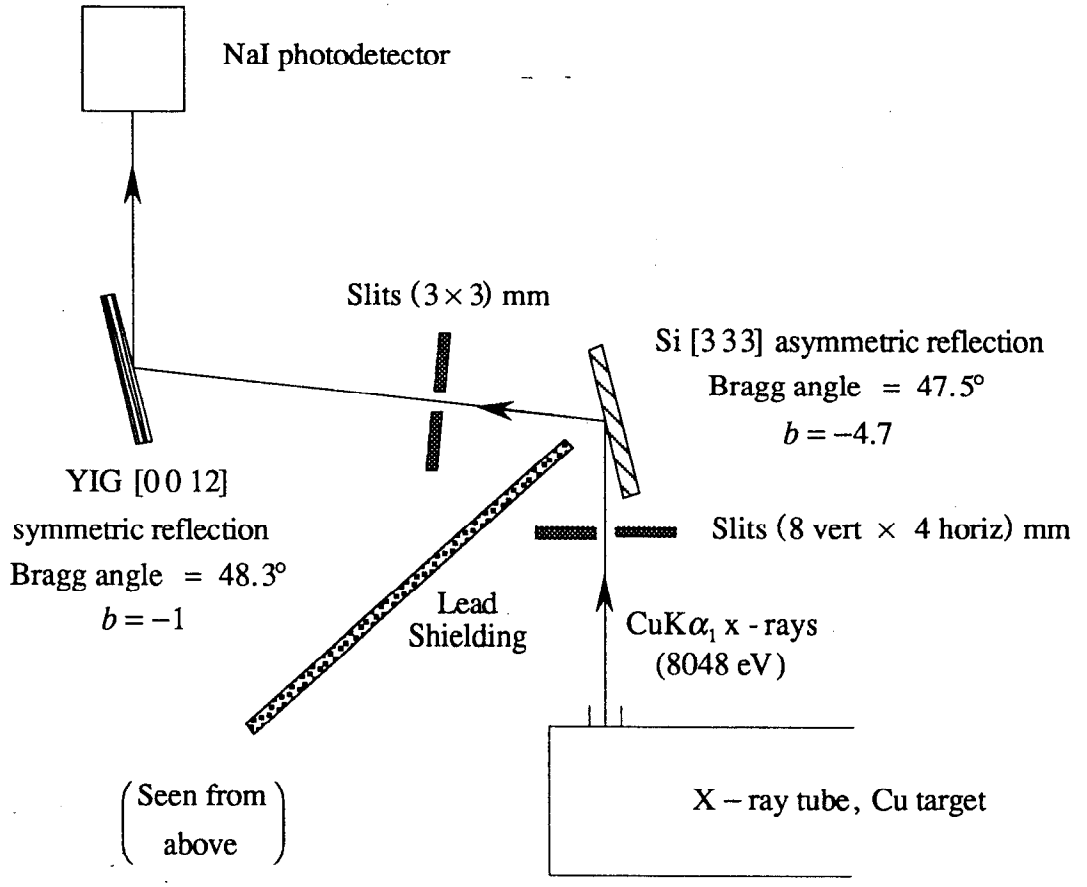

Fig. 9-1.1 Experimental arrangement for high resolution measurements of the YIG Darwin width.

The yttrium iron garnet (YIG) crystals were grown by Gualtieri at Allied-Signal's Electronic Materials and Devices Lab. Each sample was grown using a liquid phase epitaxy method where a (0 0 1) oriented gadolinium gallium garnet (GGG) substrate was inserted into a heated platinum crucible (≈ 890°C) containing yttrium and enriched iron oxides dissolved in a lead oxide-vanadium oxide flux (the isotopic composition of the iron, as measured by Oak Ridge National Lab, was 0.79% ^{54}Fe, 18.24% ^{56}Fe, 80.97% ^{57}Fe, and 0.0% ^{58}Fe). Using techniques very similar to those applied towards growing magnetic bubble memory layers, Gaualtieri was able to epitaxially grow nearly perfect (0 0 1)

oriented YIG crystal films of various thicknesses (2.7 to 9.5 μm) onto six 5 mm thick GGG circular substrates having a diameter of 3 cm. The formula unit for the YIG films, obtained from lattice constant data and Faraday rotation measurements, is

$$(Y_{2.96}Pb_{0.04})Fe_3(Fe_{1.94}Y_{0.06})O_{12}.$$

The lead was incorporated into a few dodecahedral lattice sites normally occupied by yttrium atoms. This was done to alleviate crystal strains by matching the YIG to the GGG lattice spacing. The YIG films are basically free of dislocations and other surface defects (they cover much less than 1% of the surface area), and the films have a thickness variation of only about 0.15 μm (the edges are slightly thicker than the center).[1]

A major area of concern was the degree of crystal perfection of the films--whether the films were composed of a mosaic of small crystal domains or were composed of just a few large crystal domains. Rocking curve measurements were performed to ascertain how perfect the crystal films were using the setup shown in Fig. 9-1.1. An x-ray generator provided a CuKα_1 x-ray source beam (8048 eV) for the measurements. An asymmetric Si [3 3 3] crystal was used as a nondispersive monochromator (the surface normal pointed in the [2 2 0] direction). By reflecting from the (3 3 3) planes in asymmetric geometry, the monochromator produced a highly collimated beam having an angular divergence of about 4.3 μrads. This collimated beam was used to measure any small features in the rocking curves of the YIG films that may be due to crystal imperfections.

Fig. 9-1.2 show the [0 0 12] rocking curves for the six YIG crystals labeled 57-1 to 57-6. The rocking curves are only for YIG films on the side of the GGG substrate that was facing downwards in the crucible melt. The YIG [0 0 12] reflection was chosen so that the incident beam would penetrate deep into the film allowing the entire thickness of the film to be probed (Rocking curve measurements were initially done when the crystals were first received from Gualtieri. However, in these measurements the YIG crystals were rocked against each other for the [0 0 4] reflection. Thus, the angular resolution was 25 to 50 μrads depending upon which YIG crystal was used as the monochromator rather than the 4.3 μrads resolution of the asymmetric Si [3 3 3] crystal, and the YIG [0 0 4] reflection enabled an examination of only the first 2 μm of the YIG film due to primary extinction effects). The GGG substrate reflection, which is less prominent for thick films, is the peak at the lowest angle (which has been set at a deviation angle of 0 μrads) since GGG has a larger lattice spacing than YIG. The figures show that the attempt at matching the YIG to the GGG lattice spacing by substituting a few yttrium atoms with lead has produced unexpected problems. The difference in lattice spacing between bulk GGG

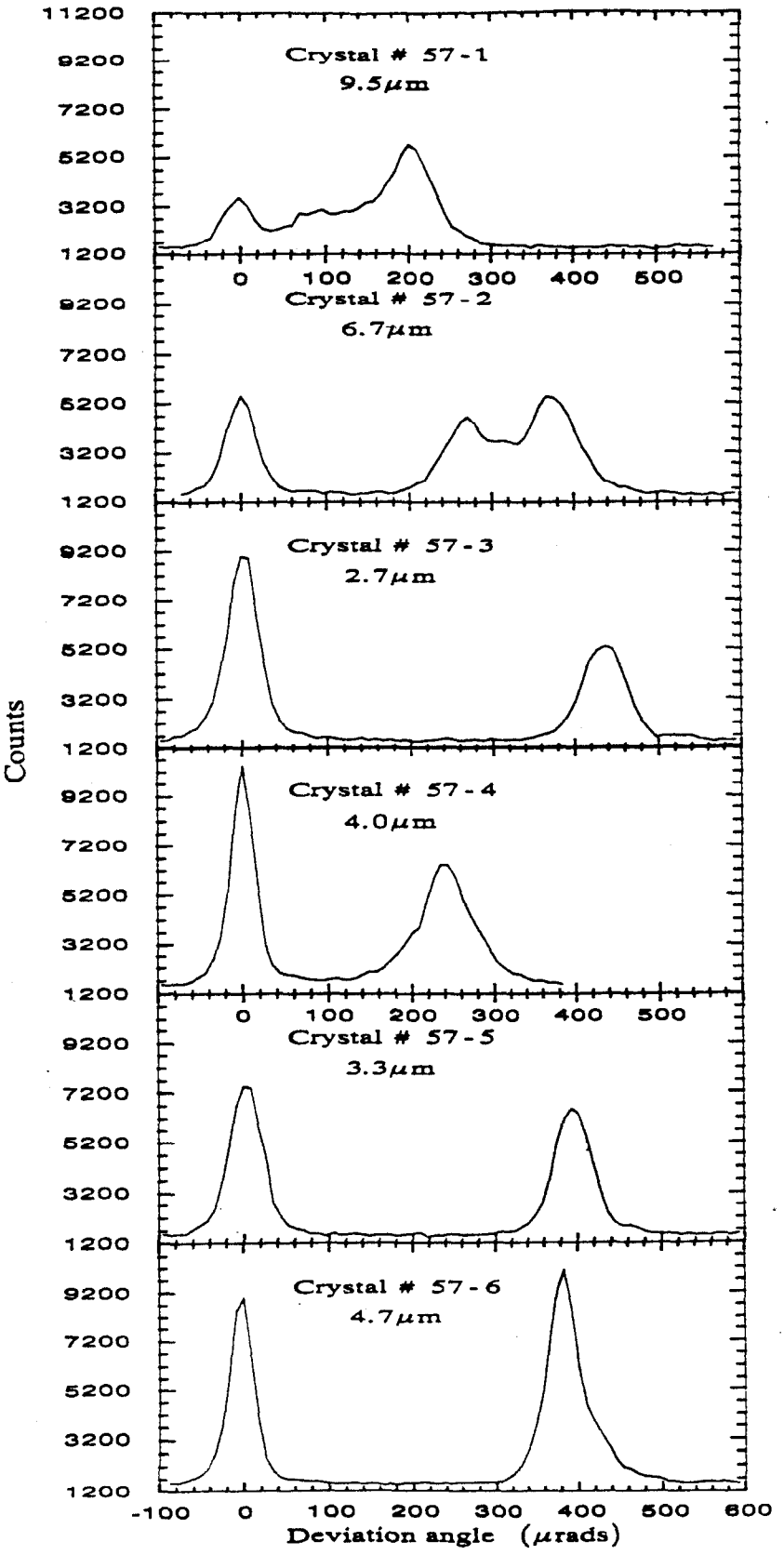

Fig. 9-1.2 Rocking curves for six YIG films 2.7 μm to 9.5 μm thick.

$(12.3840\,\text{Å})$ and bulk YIG $(12.3780\,\text{Å})$ is 6×10^{-3} Å. For the crystals 57-6, 57-5, and 57-3 where the lead had the smallest effect, the lattice mismatch was successfully reduced by 30% without significantly distorting the rocking curves. For the other crystals where the lattice mismatch was reduced by 50-60%, the YIG films separated into two or more regions, or sublayers. Substituting too many yttrium atoms with lead to further increase the YIG lattice spacing appears to lead to the formation of composite YIG films having crystal layers with different lattice spacings. The remarkable feature about this effect, which is noticeable for crystal 57-2, is the tendency for the YIG crystal to form nearly perfect crystals for each sublayer rather than a single layer composed of a homogeneous distribution of mosaic crystals or lattice spacings which would form a single broadened rocking curve.

The difference between the perfect crystal rocking curve and the measured rocking curve gives the degree of crystal perfection of the crystal sample. The silicon crystal used as the monochromator in the rocking curve measurements is of the same stock as those used as SSRL beamline monochromators. They generally have Darwin widths (full width at half maximum) that are not more than 10% greater than the ideal perfect crystal Darwin width--the silicon monochromators are essentially perfect crystals. The YIG crystal films, on the other hand, are not as perfect. The Ewald computer code discussed in Chapter 8 was used to evaluate the rocking curve for a perfect YIG crystal rocked against a fixed asymmetric Si [333] perfect crystal (the asymmetry parameter is $b=-4.7$). For perfect YIG crystals having thicknesses of 4.7, 3.3, and 2.7 μm, the Darwin widths were 24, 34, and 39 μrads respectively. The measured Darwin widths were 43, 55, and 60 μrads. Thus, the Darwin widths for the YIG films were roughly $1\frac{1}{2}$ to 2 times greater than the ideal widths. The YIG crystal perfection, though not up to par with the silicon crystals, is still quite good. One cause for the rocking curve broadening may be due to the incorporation of lead into the crystal in the attempt to create strain free films. The lead increases the lattice constant of the unit cell, and, with lead atoms interspersed throughout the YIG film, this would lead to a nonuniform lattice constant throughout the film which would contribute towards broadening the rocking curve.

9.2 General Experimental Setup

Time resolved nuclear resonance experiments were done at three different beamlines: a 15 period 1.05 m wiggler beamline 10-2 at the 3-3.5 GeV SPEAR storage ring, a 26 period 2 m undulator beamline PBF 1 at the 5-15 GeV PEP storage ring, and a

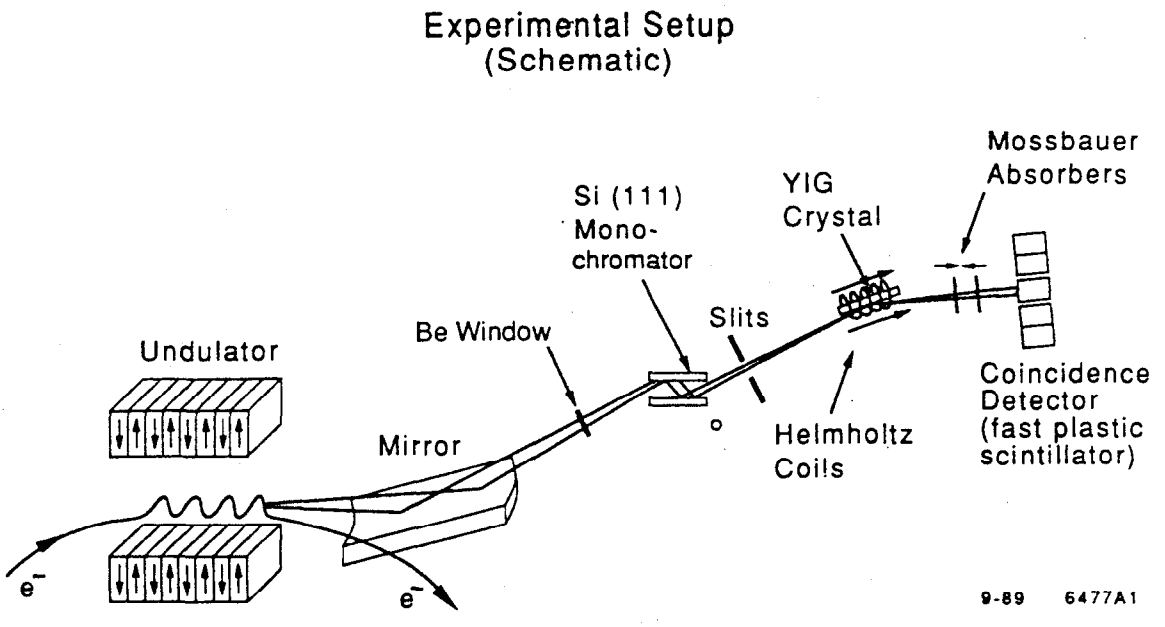

Fig. 9-2.1. General experimental setup. Mirror focusing was done in the horizontal (perpendicular to this page), not vertical, direction.

48 period wiggler beamline F2 at the 5.5 GeV CESR storage ring. The experimental setup at each of these beamlines was similar to that shown in Fig. 9-2.1.

The wiggler or undulator consisted of a periodic dipole arrangement of permanent magnets (Nd-Fe-B magnets for the beamline at SPEAR and Sm-Co magnets for the beamlines at PEP and CESR). The arrangement of magnetic dipoles forces any electron that travels down the axis to oscillate (or wiggle) about the nominal orbit and emit radiation with a range of frequencies that is tunable by varying the magnetic field strength or the dipole period length. The deflection parameter, K, is a measure of this tunability,

$$K = eB_0\lambda_u/2\pi m_e c, \qquad (9\text{-}2.1)$$

where B_0 is the magnetic field strength at the nominal electron orbit, and λ_u is the dipole period length. For $K > 5$ the magnet dipole array is considered to operate as a wiggler, and the characteristic energy spectrum of the wiggler radiation is broadband up to the critical energy

$$\varepsilon_c = 0.665E^2[GeV]B_0[T] \qquad (9\text{-}2.2)$$

where E is the electron beam energy. For $K \lesssim 2$ the array is considered to operate as an undulator, and the energy spectrum is composed of harmonics that are narrowband for the odd harmonics. By changing K one of the narrowband harmonics can be tuned to a desired operating energy and, to a degree, achieve energy monochromatization.

Tuning was done for the permanent magnetic arrays by changing the magnet gap spacing which changes the magnetic field strength at the nominal electron orbit. For instance, the desired operating energy at PEP was 14.4 keV. Placing the first harmonic at an energy slightly greater than 14.4 keV ensured operation on the safe low energy side of the harmonic peak that varied more slowly with energy than the edge-like high energy side. A magnetic gap spacing of 5.5 cm resulted in a magnetic field of 1.4 kG, a K value of 1.0, and placed the first harmonic at 14.8 keV.

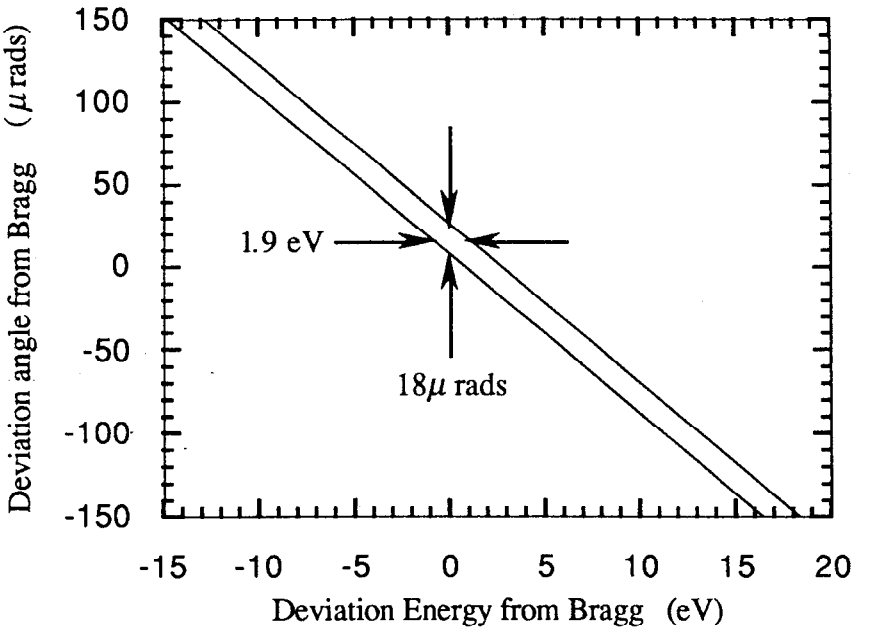

Fig. 9-2.2. DuMond diagram for the Si [1 1 1] monochromator at the SPEAR 10-2 beamline. The angular divergence of the photons arriving at the monochromator spans the 300 μrad range in the figure (the energy ranges over thousands of eVs), but the monochromator allows only those photons having angles and energies lying within the narrow strip having a width of 18 μrads and 1.9 eV.

A double crystal Si [1 1 1] monochromator was used to provide a source beam having a 2 eV wide bandwidth for a given scattering angle (two crystals were used to produce an output beam parallel to the incident beam). The DuMond diagram for such a

crystal arrangement is shown in Fig. 9-2.2. Since the energy spectrum of the radiation impinging upon the monochromator covers thousands of eVs, the monochromator substantially reduces the photoelectric background. However, a Si monochromator has the shortcoming of having a narrow vertical angular acceptance of 18 μrads at a given energy.

Electrons traversing a synchrotron bending magnet or a wiggler emit radiation in a narrow cone having a half angle of $1/\gamma$ where $\gamma = E/m_e c^2$. Depending upon the lattice design of the synchrotron, the electrons also have a vertical angular divergence at the wiggler of $2\sigma_\beta$. The net vertical angular divergence of the photons at the beamline is then the quadrature of the synchrotron radiation and electron half widths

$$2\sigma_T = 2\sqrt{\sigma_\beta^2 + \sigma_s^2} \tag{9-2.3}$$

For a bending magnet or a wiggler

$$\sigma_s = 2/\gamma\sqrt{2\pi} \tag{9-2.4}$$

is the effective rms half width of the synchrotron radiation. For the beamlines used at SPEAR and CESR, the net photon angular divergence was about 300 and 150 μrads respectively (for electron vertical half widths of roughly 50 and 30 μrads respectively for the high energy physics colliding beam mode of running). Clearly the Si monochromator, having an angular acceptance of 18 μrads, blocks out, in angular space, a sizable portion of the beam and, thereby, reduces the beam intensity by a factor of 15 to $7\frac{1}{2}$. The undulator beamline at PEP produces somewhat better results because an undulator collimates the harmonics. The first harmonic lies in a cone with a half angle of

$$\sigma_s = \frac{1}{\gamma}\sqrt{\frac{1+K^2/2}{2N}} \tag{9-2.5}$$

where N is the number of periods. For PEP the electron beam energy was 13.5 GeV, thus $\sigma_s \approx 5$ μrads ($N = 26$ and $K = 1$). The net photon angular divergence of about 100 μrads is then dominated by the electron angular divergence (the vertical half width is roughly 40 μrads for colliding beam operation). The monochromator then reduces the beam intensity by a factor of 5. If PEP were operated in a dedicated low-emittance lattice mode, the electron beam vertical half width could be reduced to as low as 5 μrads. The net photon divergence would then be only about 15 μrads, and all of the beam would pass through the monochromator. Unfortunately, PEP was mothballed before such remarkably brilliant beams could be used for experiments, and it is expected to be replaced by an asymmetric B factory for studying the possibility of CP violation in the B meson system.

At the PEP and SPEAR beamlines, a bent cylinder, fused quartz, platinum coated mirror was a standard instrument positioned upstream of the monochromator. The

cylindrical mirror provided focusing in the horizontal direction to increase the photon flux. The mirror could also be used to focus the photon beam in the vertical direction, however, because this would increase the angular divergence of the beam and result in less photons passing through the narrow vertical angular acceptance width of the Si monochromator, vertical focusing was avoided.

Unfortunately, the monochromator also allowed higher order harmonics from the [3 3 3], [5 5 5], [7 7 7], etc., reflections to pass through. The mirror again proved useful in eliminating these higher order harmonics through grazing angle scattering. By setting the grazing angle of the mirror to be near the critical angle of the [3 3 3] harmonic (29 keV), the intensity of all the harmonics was significantly diminished. The mirror then acts as a low pass filter. At the CESR beamline, there was no standard mirror upstream of the monochromator, so a portable, flat, gold coated mirror was placed downstream of the monochromator (inside the experimental hutch station). Without the mirror the photoelectric background from the harmonics overwhelmed the photodetector, thus making the mirror a critical component to do experiments.

Another typical piece of equipment was a 4 circle diffractometer. The crystals were attached to the ϕ circle of the diffractometer which in turn was attached to a χ circle which in turn was attached to a θ circle. The ϕ-axis could be rotated by rotating the χ circle, and the χ-axis could in turn be rotated by rotating a θ circle. The detector was attached to the 2θ circle which rotates independently of the other circles. These combinations of possible rotations allowed the crystals to be oriented for precision diffraction experiments.[2]

For low temperature experiments a cryogenic refrigerator assembly was attached to the ϕ circle. The assembly consisted of a two stage displex expander (Air Products DE202 expander) that cools by decompressing helium gas. On the tip of this displex unit sat the YIG crystal, and the unit was covered by a vacuum shroud having a cylindrical beryllium window. A water-cooled rotary compressor (Air Products HC-2 compressor) supplied high pressure helium gas to the displex expander. Before the refrigerator was turned on, a roughing pump was used to get the expander down to a low vacuum ($\approx 10^{-6}$ torr). A temperature controller along with a thermistor for feedback and a small heater coil inside the shroud was used to fix the temperature to a desired operating point.

Also attached to the ϕ circle was a magnet assembly that provided a uniform magnetic field of about 100 Gauss across the crystal. At the PEP and SPEAR beamlines a pair of Helmholtz coils provided the uniform magnetic field (the coils were actually attached to an unused ϕ circle on the opposite side of the χ circle). At the CESR beamline a set of Sm-Co permanent bar magnets provided the uniform magnetic field. In all cases, the magnetic field was parallel to the (0 0 1) planes (that is, parallel to the crystal surface).

9.3 Detector and Fast Timing Electronics

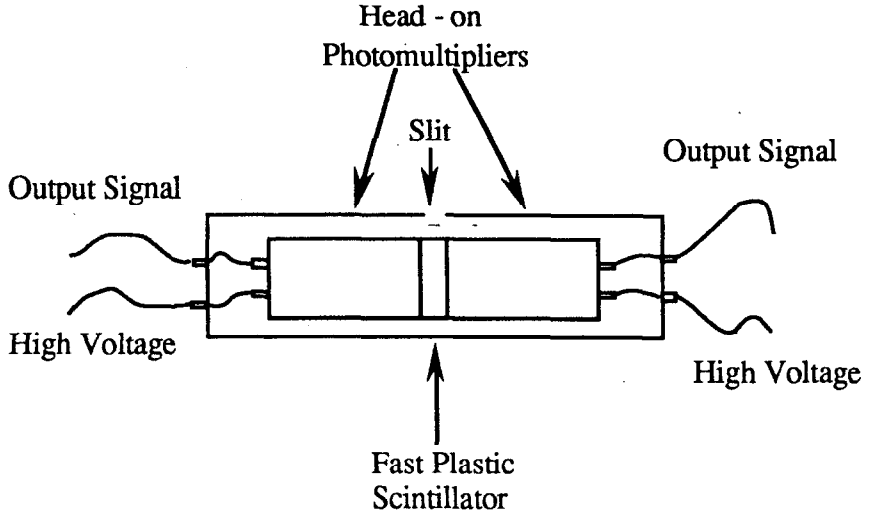

Fig. 9-3.1. General schematic of the coincidence photodetector.

Fast plastic coincidence photodetectors were used to measure the scattered x-rays. Each photodetector consisted of two head-on photomultipliers coupled to a fast plastic scintillator material (Bicron 420) via an index of refraction matching layer of silicon grease (GE Viscasil 600M silicone fluid) as shown in Fig. 9-3.1. The fast plastic is a polyvinyltoluene based organic scintillator that fluoresces with a lifetime of 1.5 nsec. An early photodetector used RCA 8575 photomultipliers borrowed from the Stanford Linear Accelerator Center's (SLAC) high energy physics group (these tubes were leftover photomultipliers used for the SLAC Mark II detector). They were old tubes, and they had significant afterpulses (possibly due to a small amount of residual gases leaking into the tubes) 460 and 540 nsecs after a prompt pulse. Even in coincidence geometry, for every 10 prompt pulses there was 1 afterpulse. However, the tubes could still be used by carefully subtracting out the afterpulse background or by ensuring that the delayed resonant signal was examined in a time window well short of the afterpulses. These photomultipliers were later abandoned in favor of mu-metal shielded Hamamatsu R329 photomultipliers having 12 dynode stages and a rise time of 2.6 nsecs. These tubes had an insignificant afterpulse rate. As measured against a NaI detector, they also had an efficiency for detecting 14.4 keV radiation of about 40%.

The fast electronics signal processing circuitry for a general experiment is shown in Fig. 9-3.3. The electronic modules were capable of processing nanosecond pulse width signals. After the amplified photomultiplier pulses pass through discriminators properly biased to reject low level background, a 2-way logic module examines the signals to see if

they are coincident (it has a double-pulse resolution of 3.3 nsecs). If the pulses are coincident, another logic module checks to see whether the coincident pulses are prompt pulses.

The timing pulse is appropriately delayed or advance in time (using cables lengths or electronic circuitry not shown in the figure) so that it corresponds to the prompt pulse that initiated the nuclear resonant response. The timing pulse is sent to a gate generator which responds by sending out a fixed 10 nsec wide delayed pulse. This 10 nsec wide pulse is the prompt window, and it is sent to veto the 1-way coincidence logic module. Thus, if a coincidence occurs within the prompt time window, it is vetoed and no further action occurs. This was done to prevent the TAC from being triggered by every prompt pulse which would overwork the TAC and lower its performance. Performing this check improved the time resolution of the resonance signal from 5 nsec to 2.5 nsec.

The prompt window is then further delayed by 250 nsec to act as the stop input to the TAC. Thus, the delayed nuclear resonance signal starts the TAC anytime from 10 nsec to 250 nsec after the prompt pulse, and the TAC is always stopped 250 nsec after the prompt pulse (see Fig. 9-3.2). The TAC sends out a signal between 0 to 10 volts that is proportional to the time difference between the stop and start signals. The MCA receives this output signal for data analysis and storage.

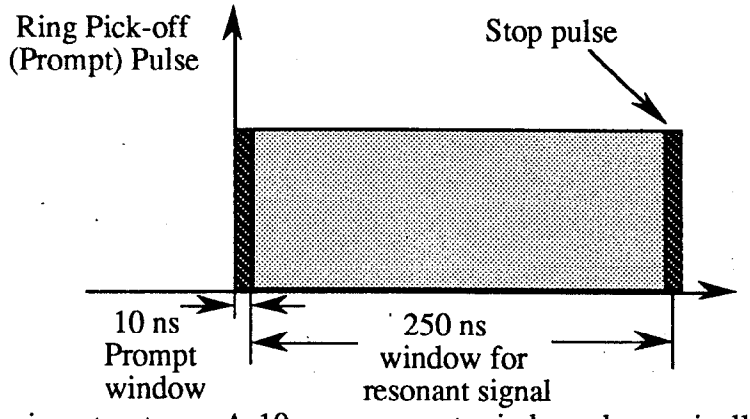

Fig. 9-3.2. Timing structure. A 10 nsec prompt window electronically gates out the prompt pulses. A 250 nsec window is constructed for measuring delayed resonant counts, and the same 10 nsec prompt window delayed by 250 nsec is used as the stop pulse to the TAC.

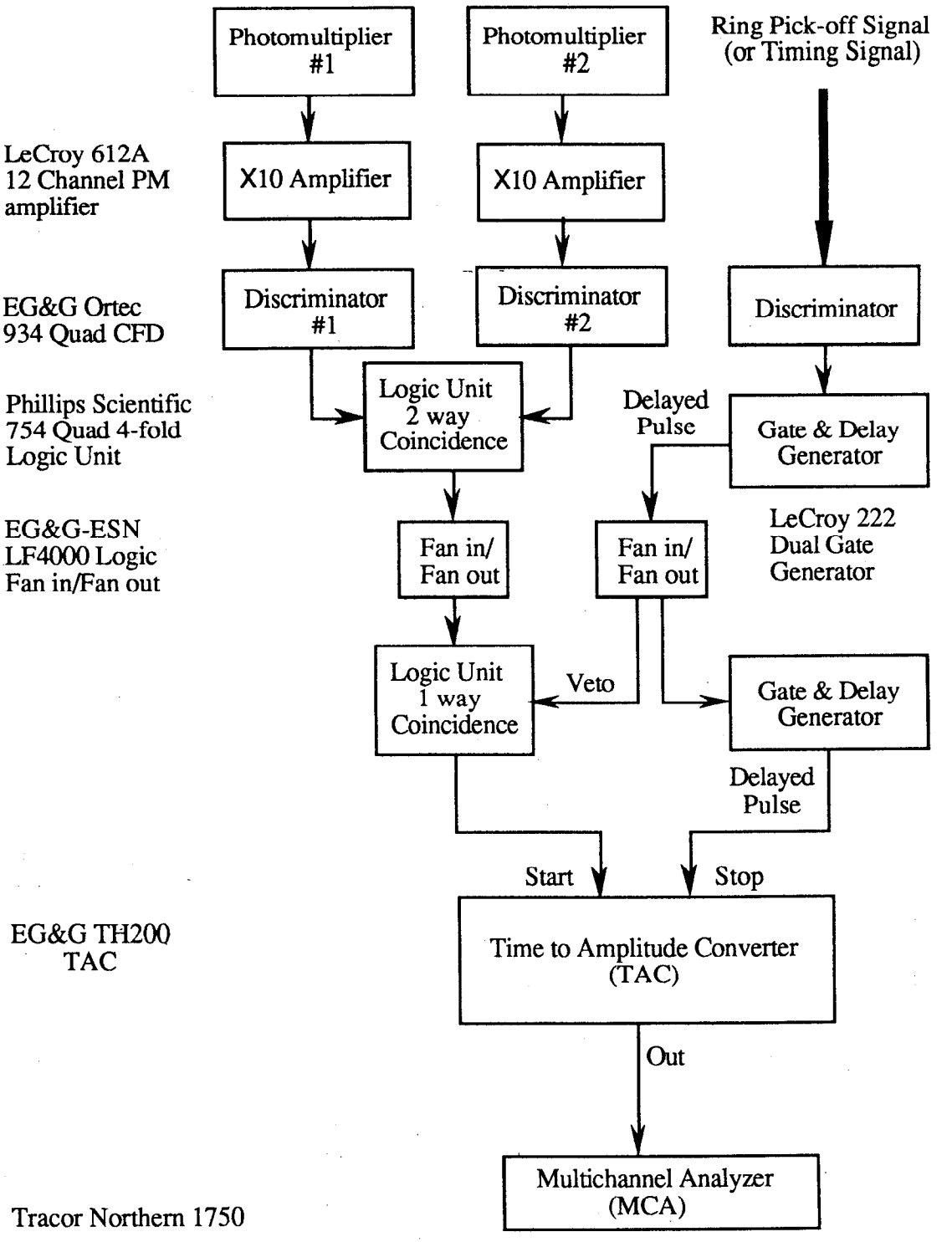

Fig. 9-3.3. General schematic of the fast electronics circuitry.

9.4 Mössbauer Experimental Setup

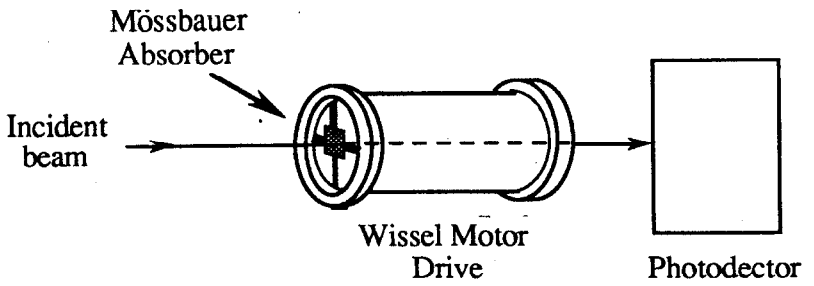

Fig. 9-4.1. General schematic of the Mössbauer experimental setup.

The general setup for doing Mössbauer experiments is shown in Fig. 9-4.1. The hollow core Wissel motor drive was well adapted for doing experiments on synchrotron beamlines. A conventional motor drive is usually designed for moving radioactive sources against a stationary absorber, and it does not need a hollow core. For synchrotron experiments hollow core drives were quite convenient because absorbers must be vibrated against a fixed source. The drive works by vibrating a hollow cylinder using electromagnetic driver coils. Attached to the end of the hollow cylinder is a sturdy diaphragm onto which an absorber can be mounted.

A synchrotron experiment was performed to measure the energy spectra of the hyperfine YIG resonance. To do this a single line sodium ferrocyanide, $Na_4Fe(CN)_6$, absorber was used as an analyzer. In Fig. 9-4.1 the incident beam is the YIG diffracted beam. The electronics set up to measure both the time spectra and the energy spectra is shown in Fig. 9-4.2. The TAC and MCA for measuring the time spectra are taken from Fig. 9-3.3. To measure the energy spectra, a gate having a time window of 250 nsec (positioned 10 nsec after the timing signal) activated the MCA for measuring resonant photons. For each valid start signal, the velocity of the motor drive was measured.

To calibrate the YIG energy spectra, Mössbauer spectroscopy was performed on an enriched ^{57}Fe thin foil using a ^{57}Co radioactive source. Obtaining the well known positions of the Fe hyperfine lines gives the calibration of the velocity drive and enables one to determine the energies of the YIG resonances. The energy spectra of the ferrocyanide absorber was also analyzed to get information on how the absorber disturbs the YIG resonant time signal. The electronics for doing these measurements is shown in Fig. 9-4.3. The transmitted beam through the absorbers was measured by a NaI inorganic scintillator detector, and the resulting signal was sent to a pulse height analyzer. The analyzer output signal was amplified (×20) and sent to the input of the MCA. The pulse

height analyzer was selected to provide an energy window for only 14.4 keV photons. If a photon had the right energy to lie within the window, the analyzer sent a gate signal to the MCA to enable it for receiving the valid input signal (along the way the pulse is shaped to be about 1.5 μsec long and 5 V high by a gate generator so that the MCA could easily handle it).

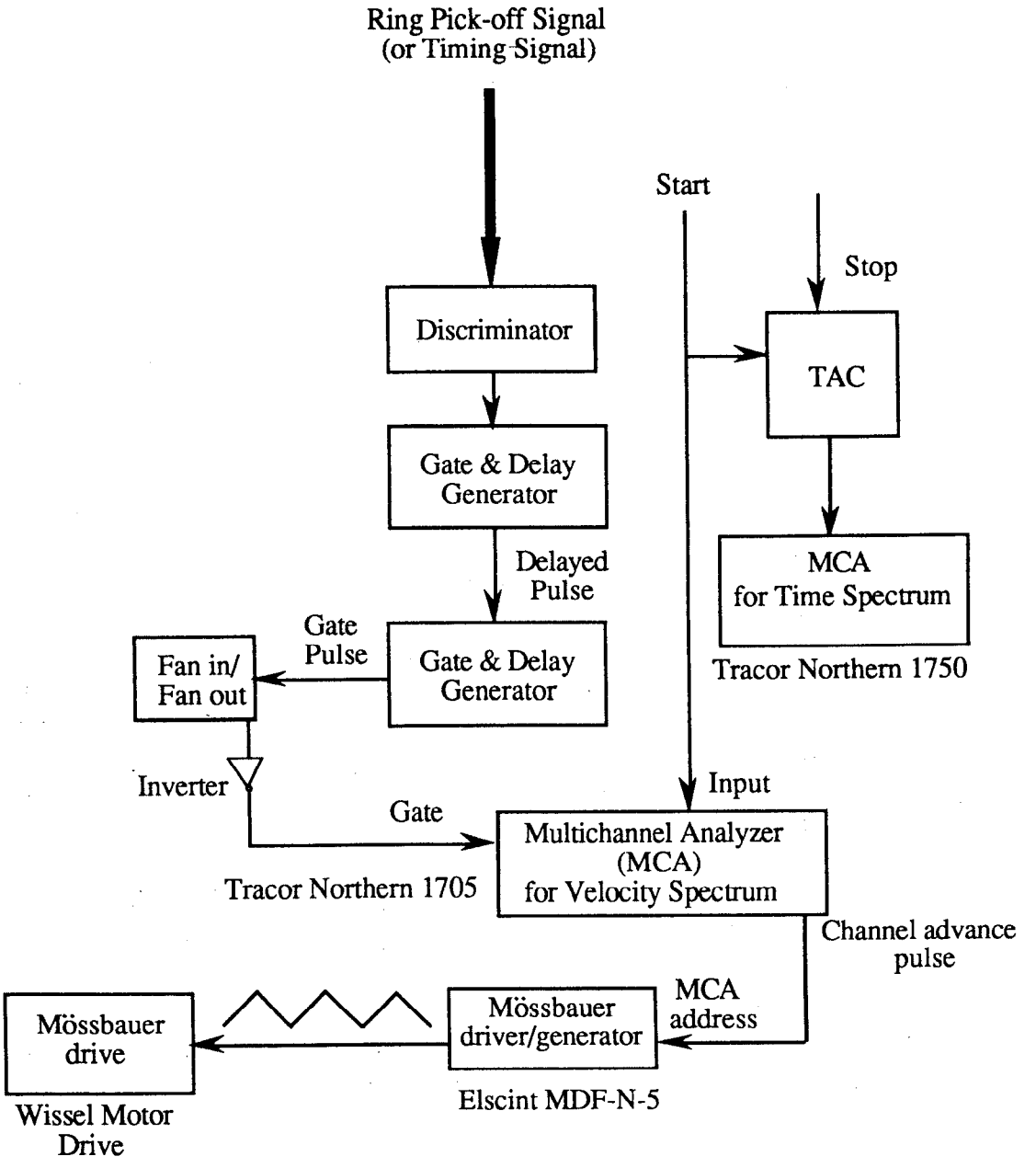

Fig. 9-4.2. General schematic of the electronics for simultaneous measurements of both Mössbauer velocity spectra and quantum beat time spectra. The start and stop signal come from the schematic in Fig. 9-3.2.

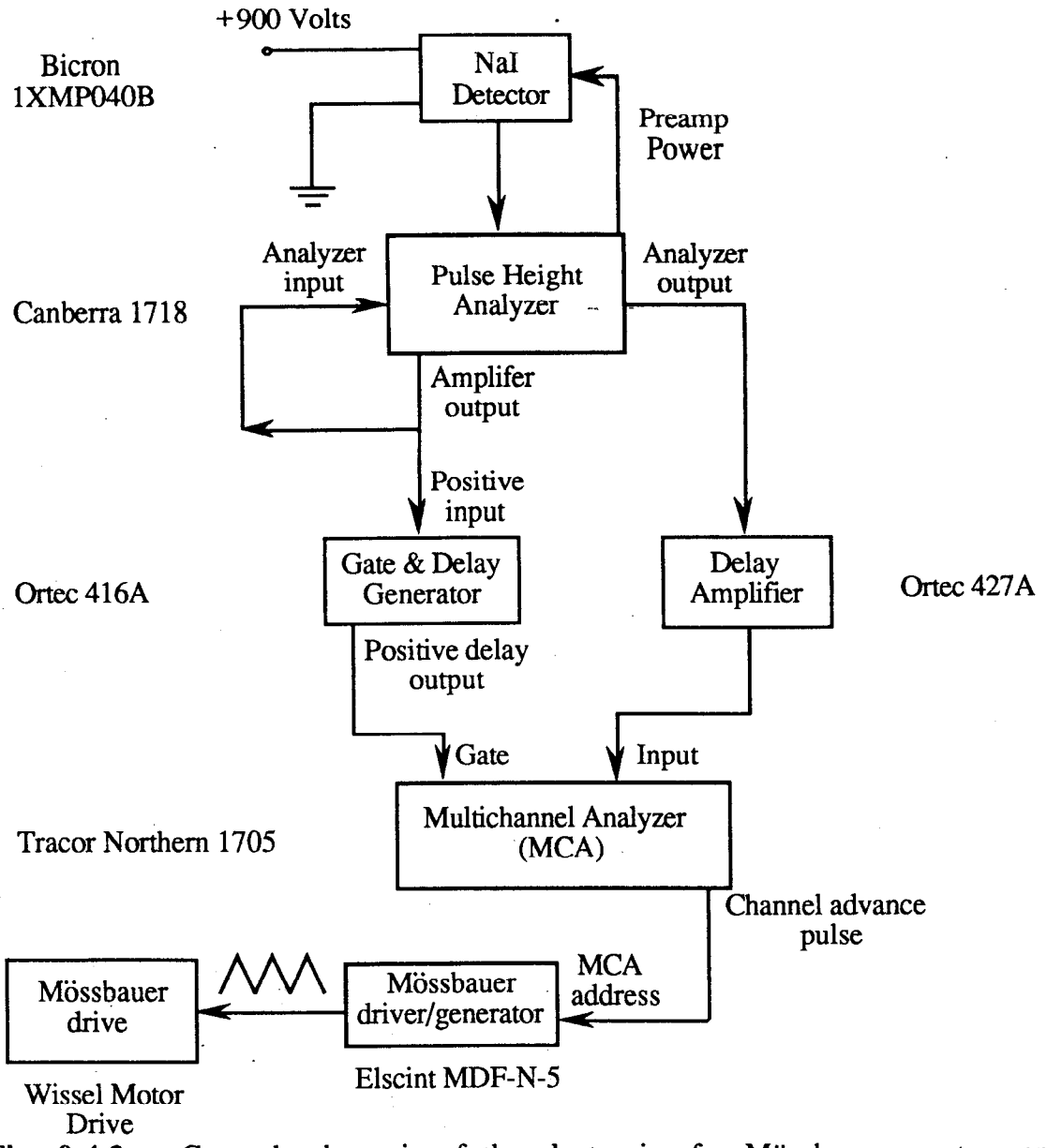

Fig. 9-4.3. General schematic of the electronics for Mössbauer spectroscopy measurements using a radioactive source.

An early Mössbauer experiment is shown in Fig. 9-4.4. This was a push-pull experiment where two black, single line, ammonium lithium ferroflouride absorbers enriched to 91.2% ^{57}Fe were used as notched filters having approximately a 2.5 mm/sec wide absorption line (They were made by Gopal Shenoy and Ersin Alp at Argonne National Labs--they were close collaborators on this experiment). The absorbers were Doppler shifted to filter out the inner two lines (lines 3 and 4) of YIG. To accomplish this, a function generator sent square wavetrains to the Mössbauer drivers. The peak-to-peak amplitude of the square waves was adjusted so that, at any instant of time, one absorber

was Doppler shifted to filter out one of the inner two lines while the other was shifted to filter out the other. The square waves arriving at the drives were in phase, so in order to make the drives operate in an antiphase, or push-pull, mode, the absorbers were fixed onto the opposite ends of the drives (one absorber was fixed to the end where the driver coil was [labeled DC in Fig. 9-4.4] and the other was fixed to the end opposite the driver coil). In this early experiment, Elscint solid core motor drives were used. Therefore, to do transmission experiments they were equipped with long paddles attached to the driver shaft. At the tips of the paddles were attached the Mössbauer absorbers. This arrangement was awkward to do synchrotron experiments, and the instrumentation was susceptible to

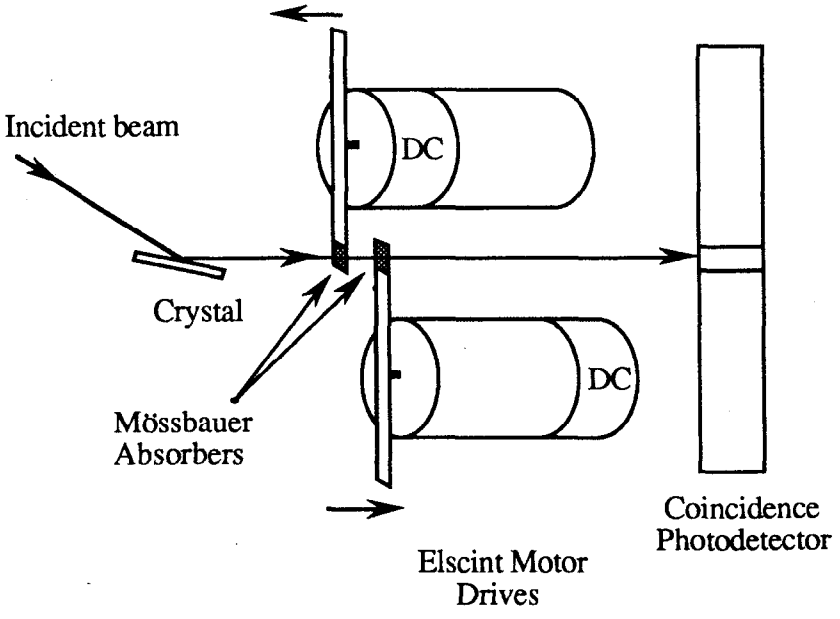

Fig. 9-4.4 Push-pull Mössbauer experiment designed to filter out the inner two hyperfine lines of YIG

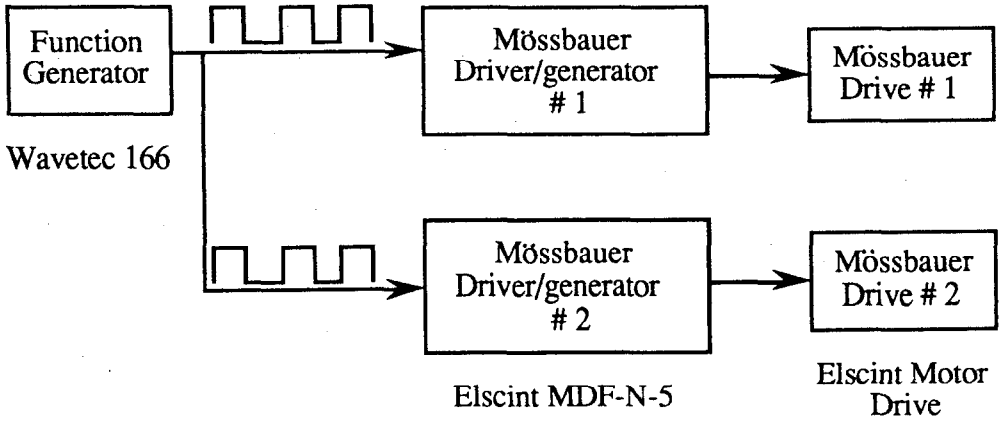

Fig. 9-4.5 Associated electronics for the push-pull Mössbauer experiment.

extraneous vibrations arising from the slippage of the paddles at the joint where they were attached to the driver shaft, the flexure of the paddles themselves, and the movement of the mount holding the absorbers to the paddles. These drives were later abandoned in favor of the hollow core Wissel motor drives.

9.5 Energy Calibration Techniques

The energy width of each of the hyperfine lines of ^{57}Fe is 4.67×10^{-9} eV with the outer two lines separated by about 6×10^{-7} eV (excluding dynamical effects such as linewidth broadening and energy shifts). The 2 eV wide energy bandpass at a given angle from the Si [1 1 1] monochromator easily covers the full range of the hyperfine spectrum. The huge photoelectric scattering (or prompt) background of around 10^{12} counts/sec resulting from the wide bandpass is reduced by 7 orders of magnitude by using a forbidden electronic but allowed nuclear reflection from the YIG crystal. The photomultipliers are not shielded from the resultant prompt pulses (the prompts are gated out electronically from triggering the TAC). Prompt rates greater than 10^6 counts/sec tend to blind the photomultipliers preventing them from seeing the delayed resonant signals--the fluorescent tails of the plastic scintillator combined with the recovery period of the photomultipliers start to become a major problem. For prompts rates of 10^5 counts/sec and nuclear signal rates of 10 to 100 counts/sec, the nuclear resonance is found by performing a monochromator energy scan. This scan is simply a measurement of the coincident delayed resonant counts (the starts in Fig. 9-3.3) versus the monochromator energy setting--the prompts time window in Fig. 9-3.2 is still used to electronically gate out the prompt signal.

To reduce the range in energy that must be searched to locate the resonance, an energy calibration is done using the krypton absorption edge. Since the krypton edge is rather broad (see Fig. 9-5.1), the monochromator can be initially calibrated to only within ± 10 eV. For experiments having a counting rate of 10 to 100 counts/sec, searching over 20 eV for the resonant signal can take a few hours. For low count rate experiments of one count/sec or less and for background rates of the same order of magnitude, a 20 eV search can take an excessive amount of time. However, once the resonance has been found, the krypton edge energy is known precisely. The krypton edge energy of 14326 eV is demarcated in Fig. 9-5.1 where the uncertainty comes from the 2 eV resolution of the monochromator. Gold also has an edge near the iron resonance. The position of its 14353

eV edge is shown in Fig. 9-5.2 and was also calibrated using the ^{57}Fe resonance. Gold also has some near edge oscillatory structure which can be useful for calibration purposes.

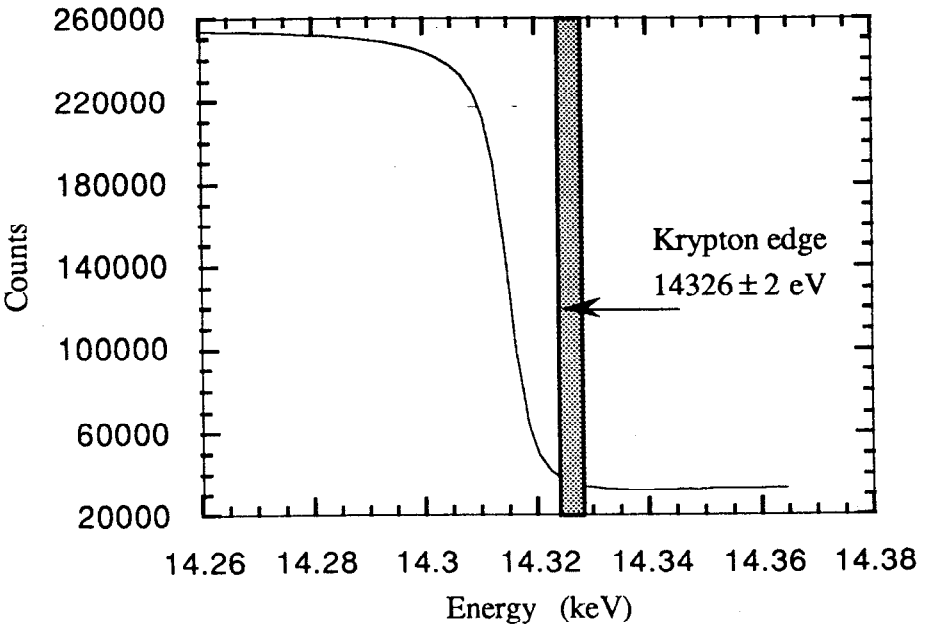

Fig. 9-5.1 Krypton edge energy scan.

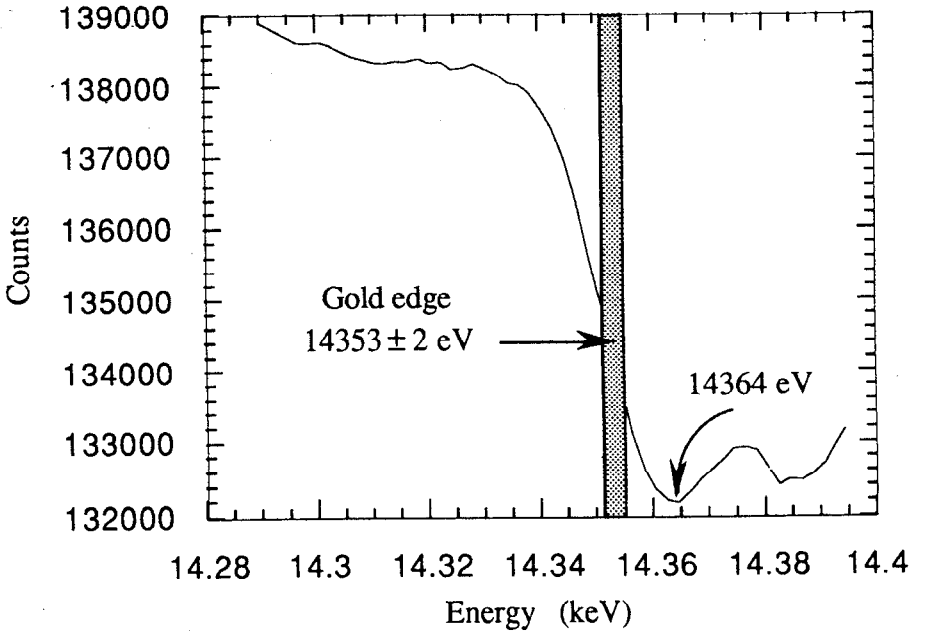

Fig. 9-5.2 Gold edge energy scan. The first minimum of the near edge structure occurs at roughly 14364 eV.

Another method of obtaining an energy calibration is to use noticeable features (or glitches) in the energy spectrum of the monochromator. The silicon monochromator has a strong primary reflection off a particular set of similar crystal planes. From two or more sets of crystal planes, it also has simultaneous weaker reflections that travel in the same direction as the primary reflection. Interference between these simultaneous, or umweganregung, reflections and the primary reflection results in noticeable glitches in the energy spectrum of the monochromator. Since the lattice spacing of Si is known very well (to within 2×10^{-4} Å), these glitches can be used as accurate energy markers. The intensity of the umveg reflections, however, is small compared to the primary reflection, so the glitches show up as small dips in the primary energy spectrum. Finding prominent, narrow glitches at high energies near 14.4 keV is also a problem. Fig. 9-5.3 shows a good candidate near 5931 eV along with its azimuthal ϕ plot. The nearly vertical reflection at 5931 eV in Fig. 9-5.3 (a) corresponds to the deep central 2 eV wide glitch in Fig. (b). This glitch actually consists of two umveg reflections lying on top of each other: the $[2\ 2\ -4]$ and $[3\ 3\ -3]$ reflections. The $[2\ 2\ -4]$ umveg reflection dominates though since it has a larger structure factor. Another good candidate closer to the resonance energy is shown in Fig. 9-5.4. The nearly vertical reflection at 11358 eV in Fig. 9-5.4 (a) corresponds to the small central dip in Fig. (b). The width of this glitch is about 8 eV--four times wider than the 5931 eV glitch. This 11358 eV glitch consists of four umveg reflections: the $[-1\ -1\ -3]$, $[4\ 4\ -8]$, $[5\ 5\ -7]$, and $[6\ 6\ -4]$ reflections. The $[-1\ -1\ -3]$ umveg reflection dominates because of its larger structure factor. A major source of broadening of the glitches comes from the nature of the monochromator. Since the monochromator consists of two parallel Si crystals, there are always two sets of umveg reflections, and this serves to broaden the glitches for Si crystals that are misoriented azimuthally in ϕ.

One of the first tries at finding the nuclear resonance signal was attempted at the SPEAR beamline 10-2. The 11358 eV glitch was used as the energy calibration even though this glitch had a broad energy width. The 5931 eV glitch was too far from the resonance to be reliable for energy calibration. A krypton edge energy scan was done to check the calibration results. The nuclear resonance was precisely right where it was expected to be (Unfortunately, by accident the glitch was labeled an 11364 eV glitch, so the first search was off by precisely the 6 eV error. This mistake was uncovered only after analyzing the beamline experiment results).

The YIG crystal produces much more noticeable umveg reflections since only forbidden reflections are used--they show up as prominent peaks rather than small dips (see Fig. 9-5.6). These umveg reflections are a major problem when searching for the nuclear

resonance because they contribute to the prompt background (the forbidden reflection is only nearly forbidden), and the strong umveg reflections easily reach the saturation limit of 5.12×10^6 counts/sec (the frequency of the electron pulses in the SPEAR storage ring). At high energies, they densely pack $\phi - E$ space as shown in Fig. 9-5.5 (Only the largest umveg reflections are shown where $F_S F_{H-S} \geq 10{,}000$ (F_S is the structure factor described in Section 7.10). Had all nonzero reflections been drawn, the figure would be nearly black). Searching for the resonance then involves finding a good, deep valley in $\phi - E$ space.

The YIG crystals can also be used for energy calibration by making ϕ-cuts and E-cuts in $\phi - E$ space and accurately mapping out the contours of all the prominent umveg reflections. An attempt was made to do this, but, because of the dense thicket of umveg reflections, more confusion resulted than progress. Of all the ways of making energy calibrations, using the krypton edge (after it was calibrated once and for all using the nuclear resonance line) was the simplest and fastest way of finding the ^{57}Fe resonance energy.

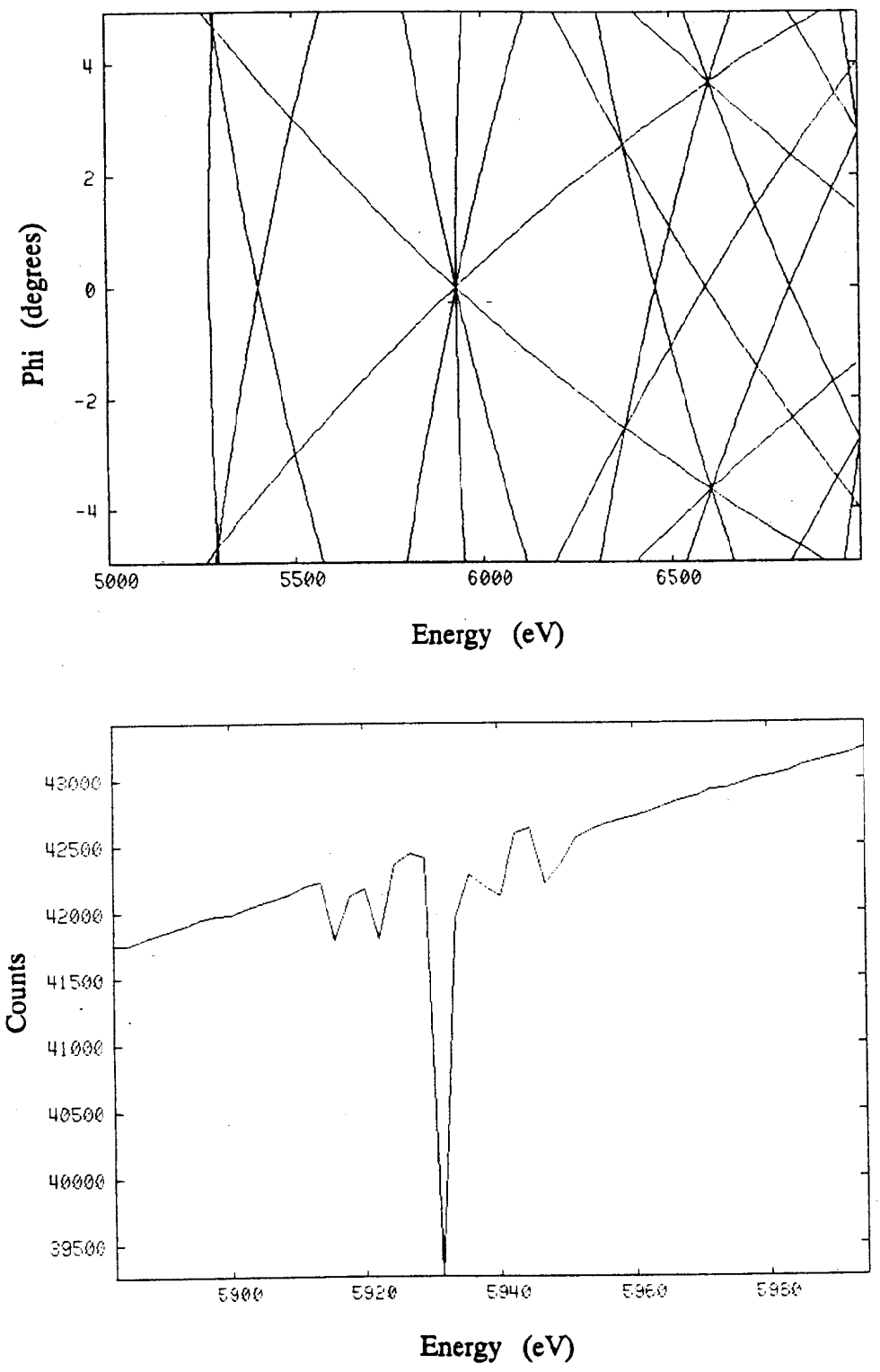

Fig. 9-5.3 (a) ϕ-plot if Si [1 1 1]. (b) Phi scan of the 5931 eV glitch of Si [1 1 1]. The prominent dip at 5931 eV is mainly due to the $[2\,2\,-4]$ umveg reflection. Since the monochromator was not precisely oriented to the $\phi = 0$ position, there was extra structure in the wings due to other nearby umveg reflections.

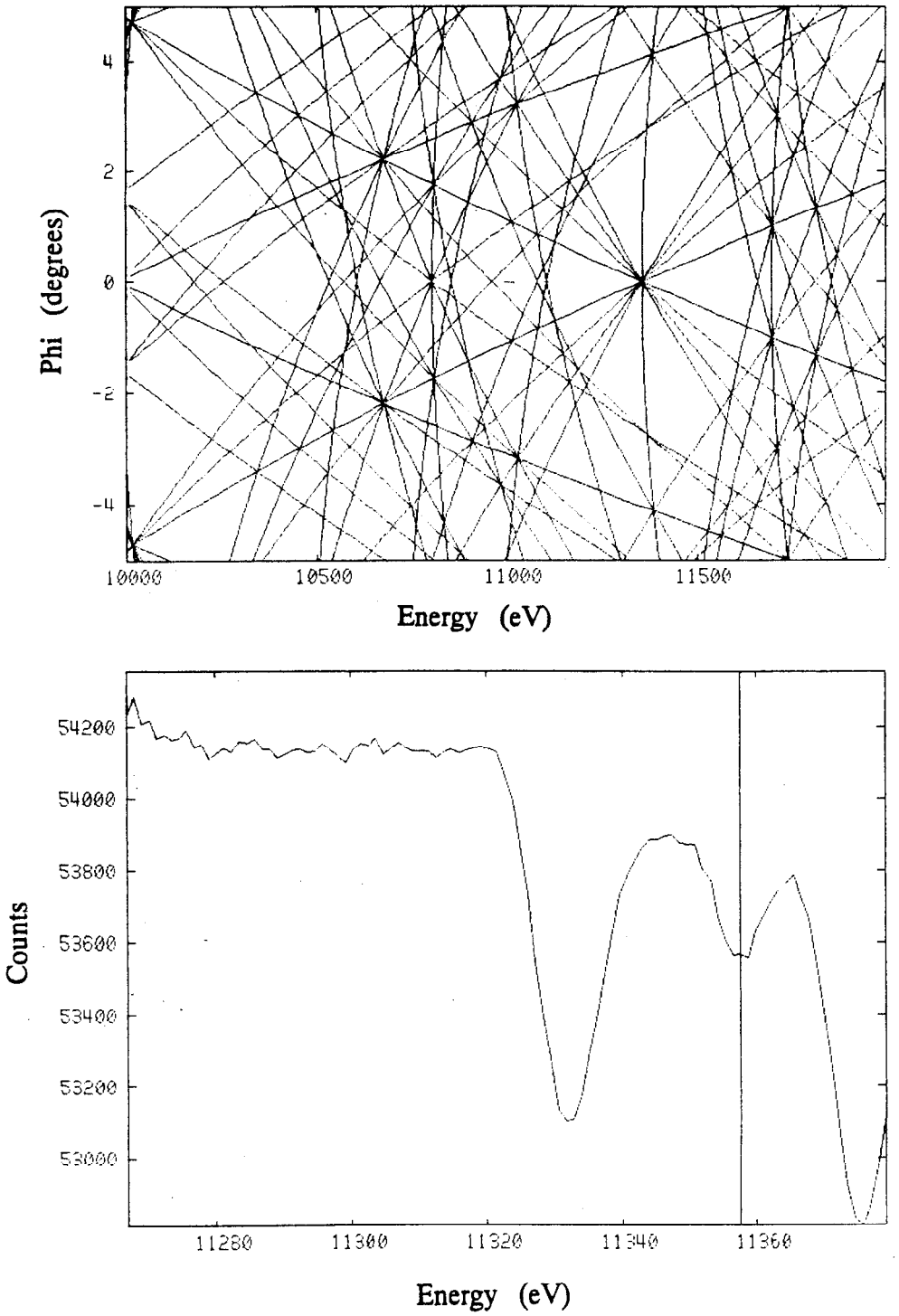

Fig. 9-5.4 (a) Phi plot of Si [1 1 1]. These plots become more densly populated with umveg reflections as the energy increases. However, occasionally there are reasonable clearings having a vertical umveg reflection surrounded by only a few nearby reflections. Vertical umveg reflections are desirable because their energy widths are narrow and give good energy markers. (b) Phi scan of the 11358 eV glitch of Si [1 1 1]. The small central dip at 11358 eV is mainly due to the $[-1\,-1\,-3]$ umveg reflection--this is the nearly vertical reflection in Fig. (a).

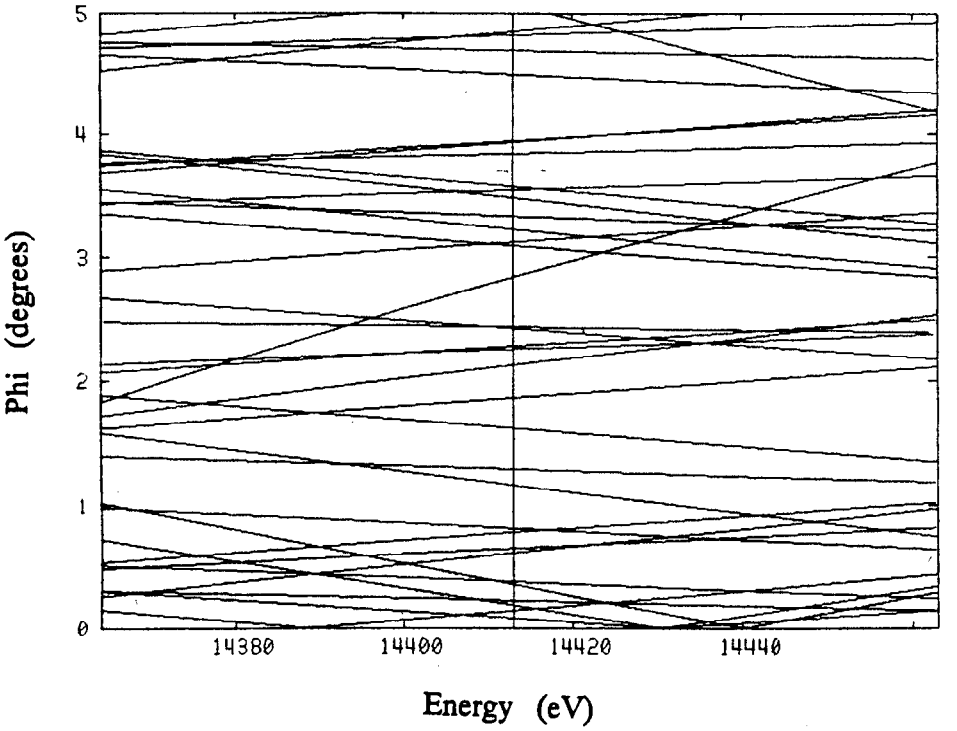

Fig. 9-5.5 ϕ-plot for YIG [0 0 2] reflection. There are no longer any convenient vertical umveg reflections to serve as energy markers (the vertical line in the figure is a marker for the 14412.5 eV nuclear resonance energy). Only the most intense umveg reflections are shown (if all nonzero reflections were shown, they would cover the figure so densly that it would be nearly black). Trying to navigate across such a terrain to find the nuclear resonance becomes a difficult task because most of the reflections are nearly horizontal.

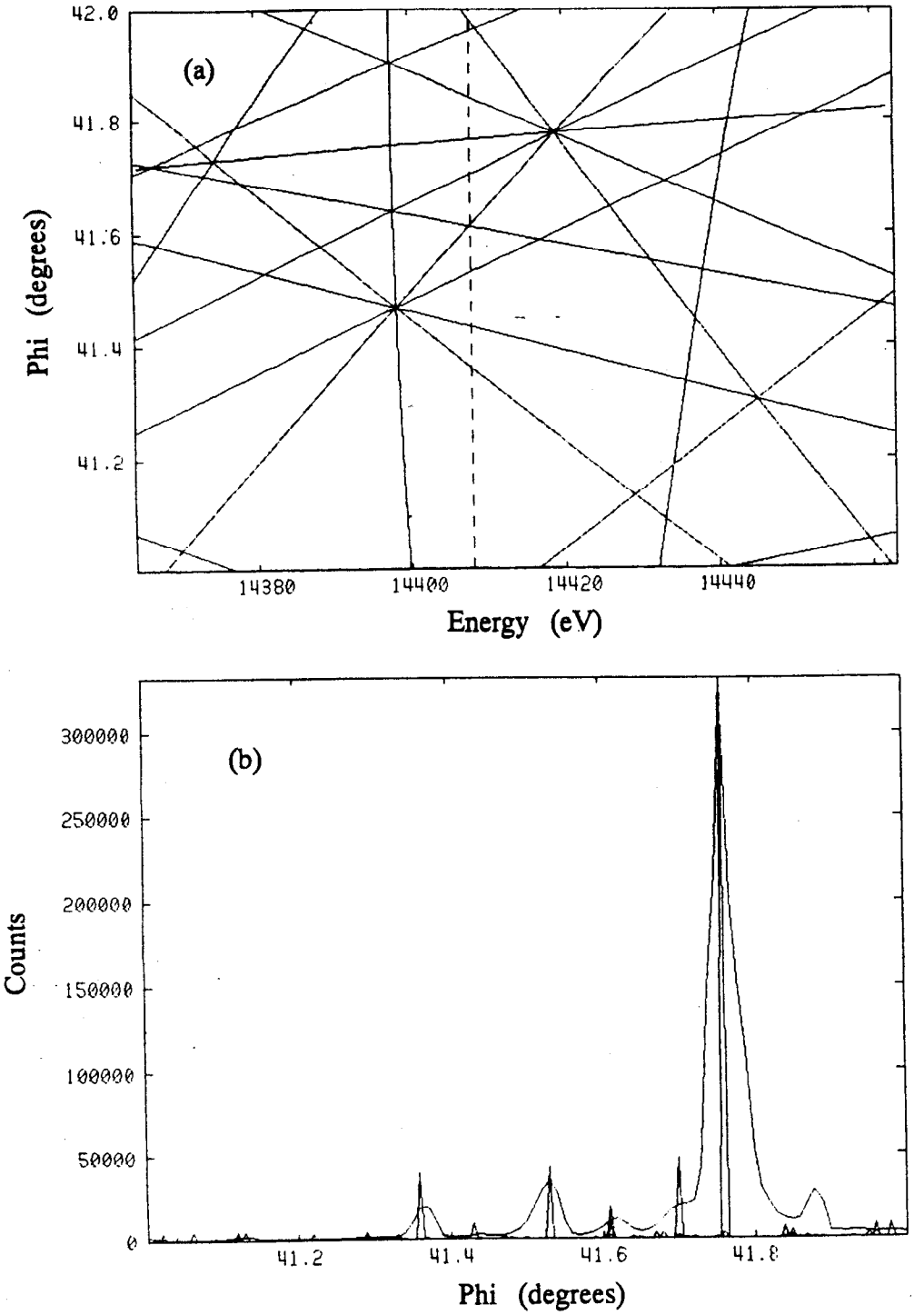

Fig. 9-5.6 (a) ϕ-plot for the YIG [0 0 2] reflection. (b) Phi scan of the [0 0 2] reflection. For forbidden primary reflections the umveg reflections show up as peaks (sometimes called antiglitches) rather than as dips (or glitches) typical in energy scans of allowed primary reflections. The markers where the umveg reflections lie are shown as sharp triangles. The position of these markers indicate that the energy of the incident beam is 14411 ± 1 eV (the dotted line). However, phi angles near 45° are not good operating points because the diffracted nuclear signal goes to zero there (the quadrupole splitting between the different iron sites in YIG goes to zero).

REFERENCES

[1] D. M. Gualtieri, W. Lavender, and S. L. Ruby, *J. Appl. Phys.* **63**, 3795 (1988).

[2] W. R. Busing and H. A. Levy, *Angle Calculations for 3- and 4-Circle X-Ray and Neutron Diffractometers*, ORNL Report 4056 (Oak Ridge National Laboratory, Oak Ridge, Tenn., 1967).

10. KINEMATICAL EFFECTS

10.1 Nuclear Hyperfine Structure Quantum Beats

The kinematical effects described in this chapter can be understood without a thorough knowledge of dynamical diffraction theory. They can be adequately described by single particle interactions rather than by the many particle, collective interactions occuring in the dynamical effects. One such striking kinematical effect is the quantum beat patterns that show up in the nuclear resonant, time-resolved measurements. These quantum beats arise from the interference between a coherent superposition of quantum states. For the case of ^{57}Fe, the coherent states are the set of hyperfine states excited when the nucleus is bombarded with an intense, broadband x-ray pulse. These excited states then fall back to the ground state and emit photons that coherently interfere with each other to produce the quantum beats. The coherence results from the scattering process remaining upon the energy shell--the nuclear state before and after the photon-nucleus interaction is identical.

Quantum beats were first observed in the early 1960's independently by Alexandrov and Dodd in the Zeeman beats arising from a superposition of electronic quantum states.[1-3] Here an external magnetic field was applied to split excited states and produce Zeeman components which could interfere with each other. Hyperfine structure beats arising from excited states naturally split by an internal magnetic field were observed in the early 1970's by Haroche.[4, 5] Also in this same time period, fine structure beats were seen by Haroche and Fabre,[6, 7] and in the late 1970's Hese used an electric field to split excited states to produce Stark quantum beats.[8] The first observation of nuclear hyperfine structure beats resulting from the excitation of nuclear quantum states was made by Gerdau in the late 1980's.[9] One should note that all of the electronic quantum beats described above were measured using gas samples while all measured nuclear quantum beats were done using solid samples. Thus the dynamical collective effects, such as resonance frequency shifts and decay rate speedups, present in nuclear systems have not been observed in electronic systems.

Nuclear hyperfine structure quantum beats are dramatic features in all of the time-resolved measurements of ^{57}Fe enriched YIG. Recall from Section 8.1 that YIG has a complicated antiferrimagnetic sublattice structure capable of producing 7 sets of 6-line hyperfine spectra (42 lines altogether). By using $[0\,0\,(4n-2)]$ YIG reflections $(n=1,2,3,\ldots)$, electronic reflections are forbidden along with nuclear reflections from all

the a-sites and the $d3$-site. The hyperfine spectra then simplifies to 2 sets of 6-line spectra from the $d1$ and $d2$-sites.

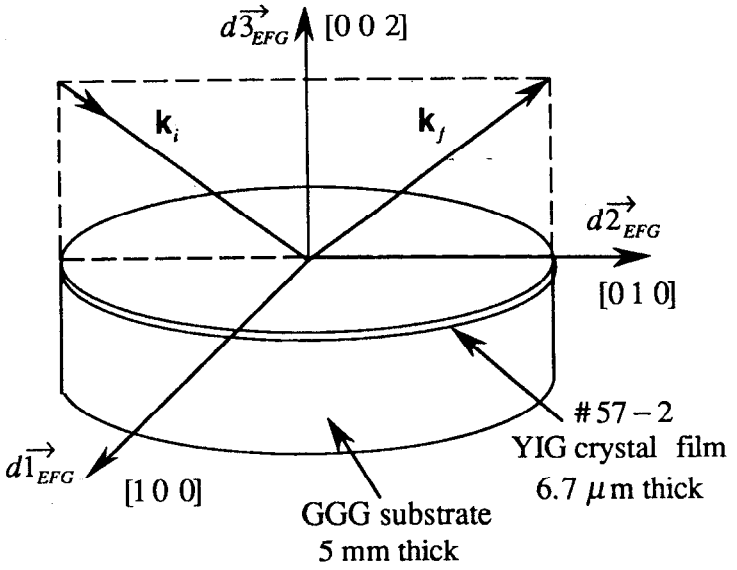

Fig. 10-1.1. Scattering geometry for nuclear resonance diffraction. The electric field gradients in the YIG crystal lie in the cubic $\langle 1\ 0\ 0 \rangle$ symmetry directions. When the applied magnetic field is perpendicular to the scattering plane formed by $\mathbf{k}_i$ and $\mathbf{k}_f$, it lies in the [1 0 0] direction parallel to the electric field gradient of the nuclear $d1$-site. When the applied magnetic field is parallel to the scattering plane, it lies in the [0 1 0] direction parallel to the electric field gradient of the nuclear $d2$-site. The incident beam is horizontally polarized perpendicular to the scattering plane.

For incident horizontally polarized x-rays and for an applied magnetic field perpendicular to the scattering plane (parallel to the polarization direction), each 6-line spectrum reduces to a 4-line spectrum (Case 1 in Section 5-1). Under such conditions, the $M = \pm 1$ transitions are allowed (see Fig. 5-3.1) and the $M = 0$ transitions are not allowed--they would be if the incident x-rays were vertically polarized. The scattering geometry is shown in Fig. 10-1.1, and a simplified hyperfine diagram along with the polarization of each line is shown in Fig. 10-1.2. Since the emitted x-rays from each line all have the same polarization, there will be quantum beats resulting from the interference of x-rays from all the resonance lines. The possible combinations of pairing the 8 lines in Fig. 10-1.2 gives 8 choose 2, or $\binom{8}{2} = 28$, possible beat frequencies. The corresponding beat periods are given in Table 10-1.1.

An experimentally measured time-resolved spectrum for such a scattering geometry is shown in Fig. 10-1.3 (using the YIG [0 0 2] reflection). Since lines 1 and 6 have the largest Clebsch-Gordan coefficients, the amplitude of their beats dominate the overall quantum beat pattern--the beating between lines 1 and 6 gives rise to the fast 7 nsec

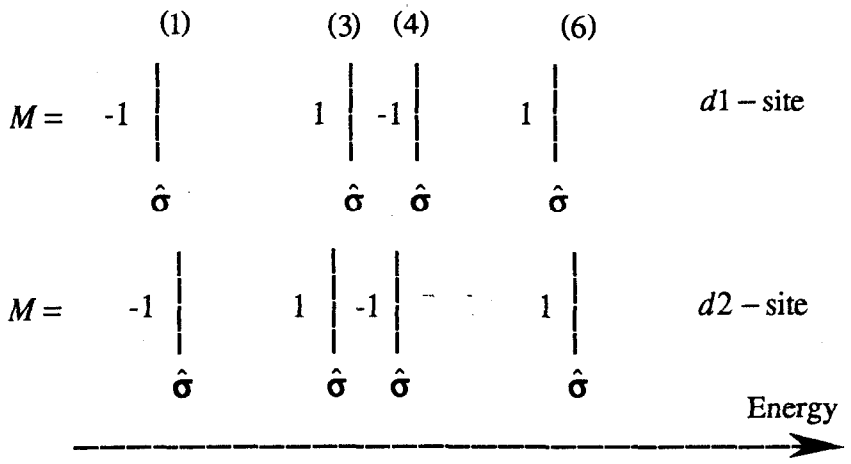

Fig. 10-1.2. Hyperfine energy spectrum illustrating the case where the applied magnetic field is perpendicular to the scattering plane. Each hyperfine line is horizontally, or sigma, polarized: $\hat{\sigma}$.

	ℓ_1	ℓ_3	ℓ_4	ℓ_6	ℓ'_1	ℓ'_3	ℓ'_4	ℓ'_6
ℓ_1								
ℓ_3	18.6							
ℓ_4	13.4	47.6						
ℓ_6	**7.22**	11.8	15.6					
ℓ'_1	**135**	16.4	12.2	**6.85**				
ℓ'_3	16.4	135	73.3	12.9	14.6			
ℓ'_4	12.1	34.4	124	17.9	11.1	46.0		
ℓ'_6	**7.66**	13.0	17.9	**124**	**7.25**	14.4	20.9	

Table 10-1.1. Hyperfine structure quantum beat periods (in nsecs) for the case of an applied magnetic field perpendicular to the scattering plane. Lines ℓ_n are from the nuclear $d1$-site, and the primed lines ℓ'_n are from the $d2$-site. The internal magnetic field strength is -3.69×10^5 Gauss and the electric quadrupole splitting is -0.89 mm/sec. The dominant quantum beats are in bold face. The average fast magnetic quantum beat seen in Fig. 10-1.3 is 7.2 nsec and the average slow electric quadrupole quantum beat is 130 nsec.

magnetic beat period seen in Fig. 10-1.3. There is also a quadrupole beat period of 130 nsec due to the electric quadrupole splitting between lines ℓ_1 and ℓ'_1 of the $d1$ and $d2$-sites (and also between lines ℓ_6 and ℓ'_6 of the two sites). This gives rise to the overall slow modulation of the beat pattern in Fig. 10-1.3. All of the other quantum beats show up as small perturbations upon the overall quantum beat pattern. The fit to the data in Fig. 10-1.3 utilizes the full dynamical diffraction theory for resonant scattering, but it relies heavily upon the energy separation of the hyperfine lines that gives rise to the quantum beat periods given in Table 10-1.1. The dynamical resonance frequency shifts discussed in Sections

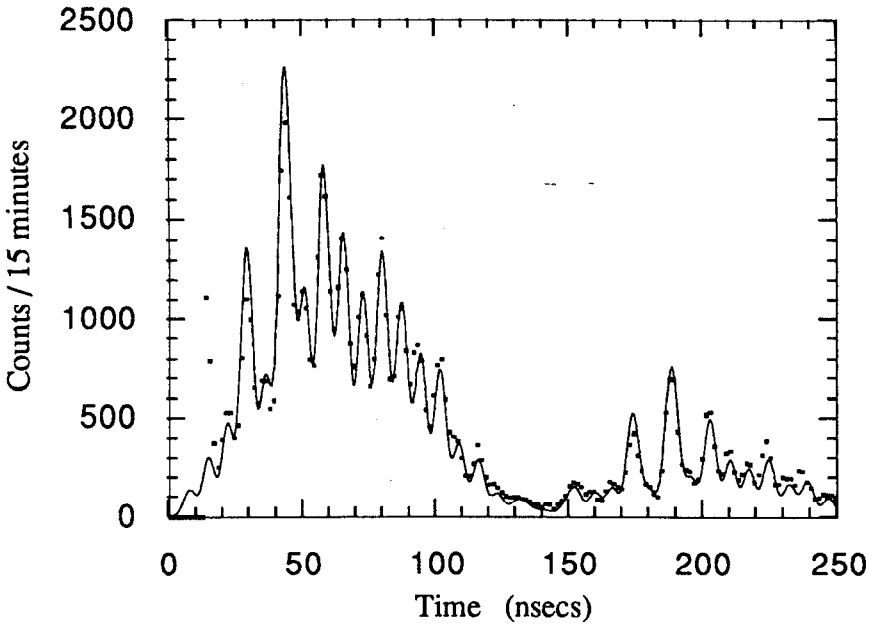

Fig. 10-1.3. Hyperfine structure quantum beat pattern for the case where the applied magnetic field is perpendicular to the scattering plane. Full dynamical diffraction theory has been applied to obtain the fit using the quantum beat periods given in Table 10-1.1. The operating angle was set at -25 μrads below the Bragg peak. Operating off the Bragg peak lessens the decay rate speedup and allows the slow electric quadrupole quantum beat to be seen.

7.6 and 7.7 slightly change these quantum beat periods--these small changes can lead to drastic changes in the quantum beat patterns and are further examined in Chapter 11.

When the applied magnetic field is parallel to the scattering plane and parallel to the crystal surface, all 12 lines from the d-sites are allowed (Case 3 in Section 5-1). For small Bragg angles, the $M = 0$ lines can be neglected, and the 12 lines reduce to 8 (the magnetic field is then nearly parallel to the incident and scattered photon directions). The simplified hyperfine diagram for such a case was discussed earlier and is shown in Fig. 8-1.4. The $M = +1$ lines emit left circularly polarized photons (polarization $\hat{\mathbf{e}}_+$) while the $M = -1$ lines emit right circularly polarized photons (polarization $\hat{\mathbf{e}}_-$). Since photons of orthogonal polarizations do not interfere with each other, the total number of beat frequencies is twice 4 choose 2 combinations of pairs of lines, or 12 possible beat frequencies. The beat periods for such a case are given in Table 10-1.2.

The experimentally measured time-resolved spectrum for such a scattering geometry is shown in Fig. 10-1.4. There are far fewer different beat periods than in the previous case where the magnetic field was perpendicular to the scattering plane. However, there is

	ℓ_1	ℓ_4	ℓ'_4	ℓ'_1	ℓ_6	ℓ_3	ℓ'_3	ℓ'_6
ℓ_1								
ℓ_4	11.1							
ℓ'_4	12.2	124						
ℓ'_1	135	12.1	13.4					
ℓ_6								
ℓ_3					14.4			
ℓ'_3					13.0	135		
ℓ'_6					124	12.9	11.8	

Table 10-1.2. Hyperfine structure quantum beat periods (in nsecs) for the case of an applied magnetic field parallel to the scattering plane. Lines ℓ_n are from the nuclear $d1$-site, and the primed lines ℓ'_n are from the $d2$-site. The internal magnetic field strength is -3.69×10^5 Gauss and the electric quadrupole splitting is -0.89 mm/sec. The upper left-hand and lower right-hand sections of the table represent quantum beats for right and left hand circularly polarized x-rays respectively. The average fast magnetic quantum beat in Fig. 10-1.4 is 12.2 and 13.0 nsec for right and left circularly polarized x-rays respectively. The slow electric quadrupole quantum beat is 135 and 124 nsec for right and left circularly polarized x-rays respectively.

the additional complication of two superimposed quantum beat patterns of two different polarizations (right and left circular polarizations) having slightly different beat periods (about 12 nsec for the right and 13 nsec for the left circular polarization). Due to the slightly different beat periods for the two overlapping beat patterns, they go into and out of phase as time goes on. In Fig. 10-4.1, the point in which the overlapping beat patterns get out of phase is around 60 to 70 nsec and gives rise to the anomalous feature present there where the overall beat pattern is nearly washed out. This null point is one of the most difficult features of the beat pattern to fit because it is very sensitive to a wide host of kinematical and dynamical effects.

In the sections to follow, the quantum beat patterns will be examined to investigate interesting physical properites such as the polarization of the incident beam, the Lamb-Mössbauer factor, and the internal hypefine crystalline fields at room and low temperatures. In the final section angular interferometry is used to explore the phase shift of a rotated quantum state. Quantum beats are seen to be a very useful effect that can be used to understand and explore many fascinating physical phenomena in resonant scattering physics.

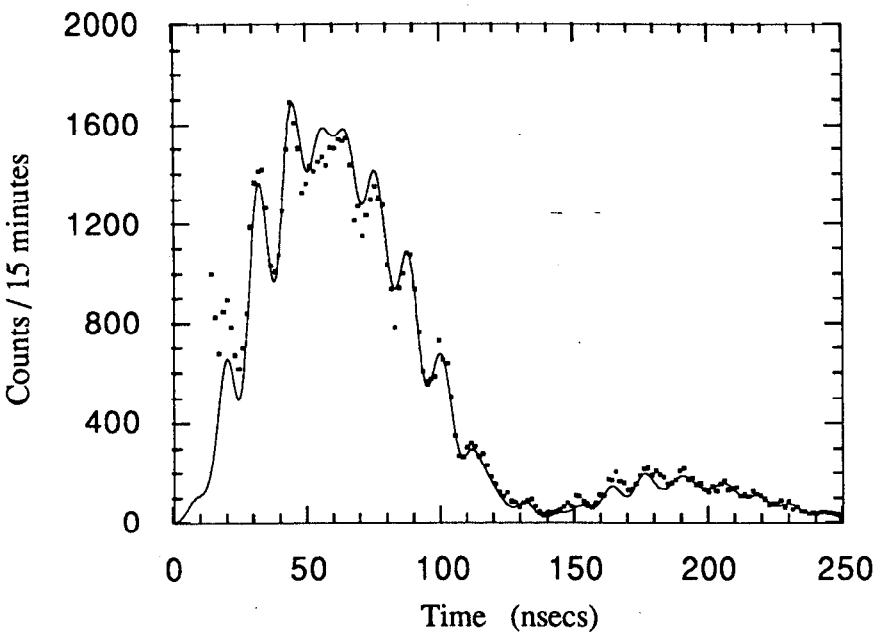

Fig. 10-1.4. Hyperfine structure quantum beat pattern for the case where the applied magnetic field is parallel to the scattering plane. Full dynamical diffraction theory has been applied to obtain the fit using the quantum beat periods given in Table 10-1.2. The operating angle was set at -20 μrads below the Bragg peak.

10.2 Analysis of Internal Hyperfine Fields

Time and frequency lie in dual spaces that are the reciprocal of each other. The decision to examine a scattering process in either temporal or frequency space will not change the underlying physics of that process. A Mössbauer velocity measurement should yield the same information as a time-resolved measurement. However, the collected information may be more difficult or easier to interpret depending upon what type of measurement is made. For instance, the phase information in a scattering process is more easily seen in a time-resolved measurement while the hyperfine resonance energies are more easily seen in a Mössbauer velocity measurement.

In this section, the internal magnetic dipole and electric quadrupole fields are investigated through time-resolved spectroscopy. The main utility this method has over Mössbauer velocity spectroscopy is the length of time needed to take sufficient data for low count rate experiments. For counting rates of around 100 counts/sec, the time spectra can be collected in about 1 minute to get enough statistics to determine the hyperfine field

parameters adequately, while a Mössbauer velocity spectra would need several hours of collection time to get the same information. One reason for this is because the velocity measurement is an absorption measurement collecting information about missing resonant photons, and it therefore has a larger background problem. Also, the velocity analyzer must be a reasonably thin-line absorber in order to scan the hyperfine spectra of the sample without significantly distorting, or modifying, the sample's spectra--this further increases data collection times.

To acquire an intuitive grasp of how the time spectra vary with changing hyperfine field parameters, multiple graphs are given in Figs. 10-2.1, 10-2.2, and 10-2.3. Each plot is normalized to unity and covers the first 250 nsec after the prompt excitation. The YIG [0 0 2] spectra were calculated at an angle -40 μrad below the Bragg peak in order to clearly show the electric quadrupole quantum beat. The higher order YIG [0 0 10] spectra were calculated at an angle right at the Bragg peak. The difference in operating angles gives rise to the difference in intensities between the [0 0 2] and [0 0 10] reflections--operating far off the Bragg peak significantly reduces the reflected intensity. The spectra were calculated for an internal magnetic field, $\mathbf{B}_{int}$, perpendicular and parallel to the scattering plane. When the internal magnetic field strength was varied in steps of 2 kGauss from 364 to 374 kGauss, the electric quadrupole splitting, $e^2qQ/2$, remained fixed at 0.89 mm/sec. When the electric quadrupole splitting was varied in steps of 0.02 mm/sec (or 1 neV) from 0.84 to 0.94 mm/sec (or 40 to 45 neV), the internal magnetic field strength remained fixed at 369 kGauss. The incident x-rays were fixed to be 100% horizontally polarized, and the full dynamical diffraction theory was used to perform the calculations. (The curve in bold-face in the figures is pointed to by the graphic arrow ⇓.)

Increasing the internal magnetic field strength increases the magnetic energy level splitting thus forcing the hyperfine lines to be spaced further apart in energy. Increasing the energy spacing between the hyperfine lines decreases the beat period and causes the beat pattern to be compressed in time. This accordion effect is clearly shown in Fig. 10-2.1 where increasing the internal magnetic field strength compresses the beat pattern and decreasing the field strength expands the pattern. The accordion effect is most dramatic during the second peak of the electric quadrupole beat occurring after 130 nsec. When operating far off the Bragg peak, changes in the internal magnetic field strength of 2 kGauss can be unambiguously seen in the time spectra (this is even more revealing in the fast beat spectra where the internal magnetic field is perpendicular to the scattering plane).

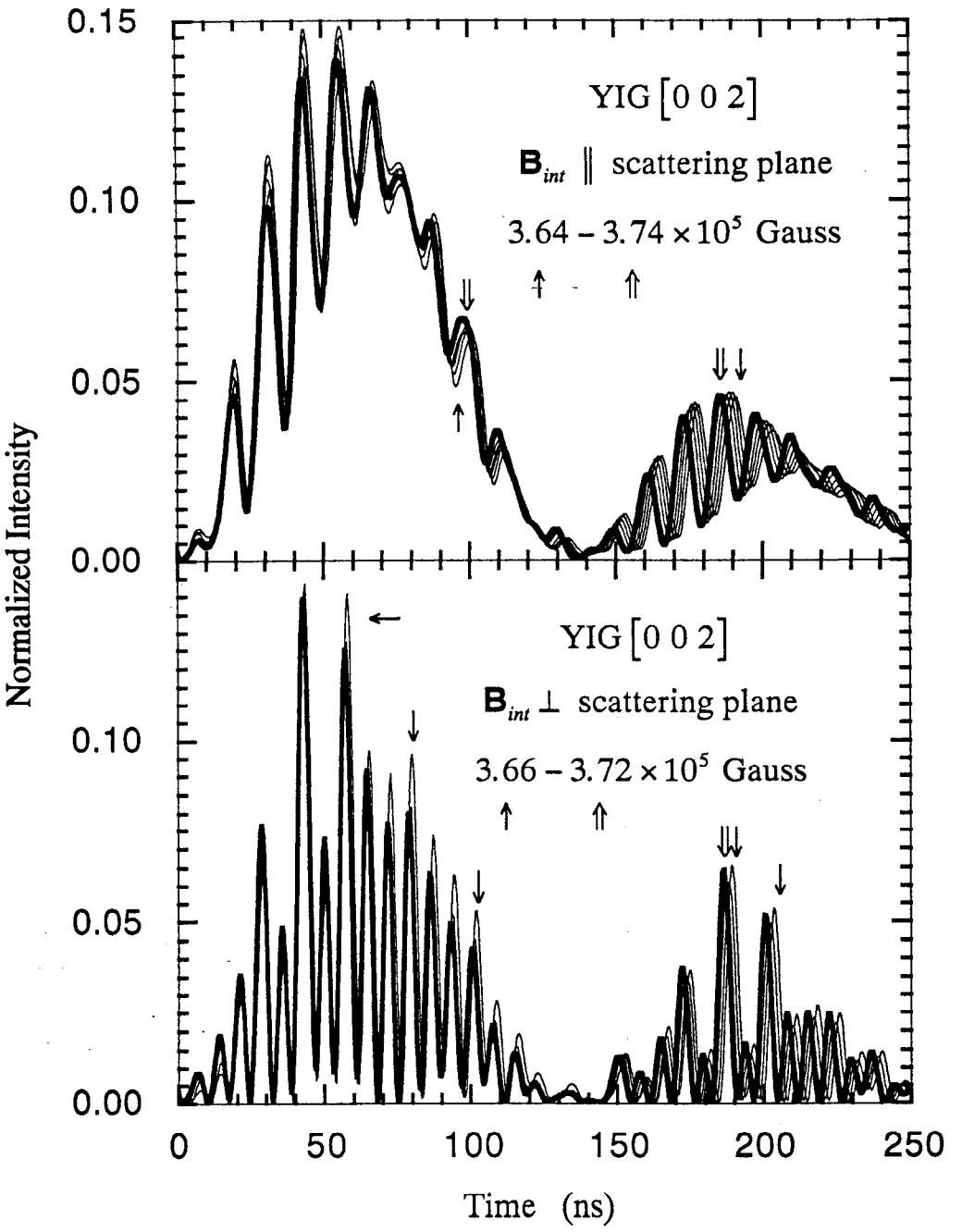

Fig. 10-2.1. YIG [0 0 2] time spectra for various internal magnetic field strengths.

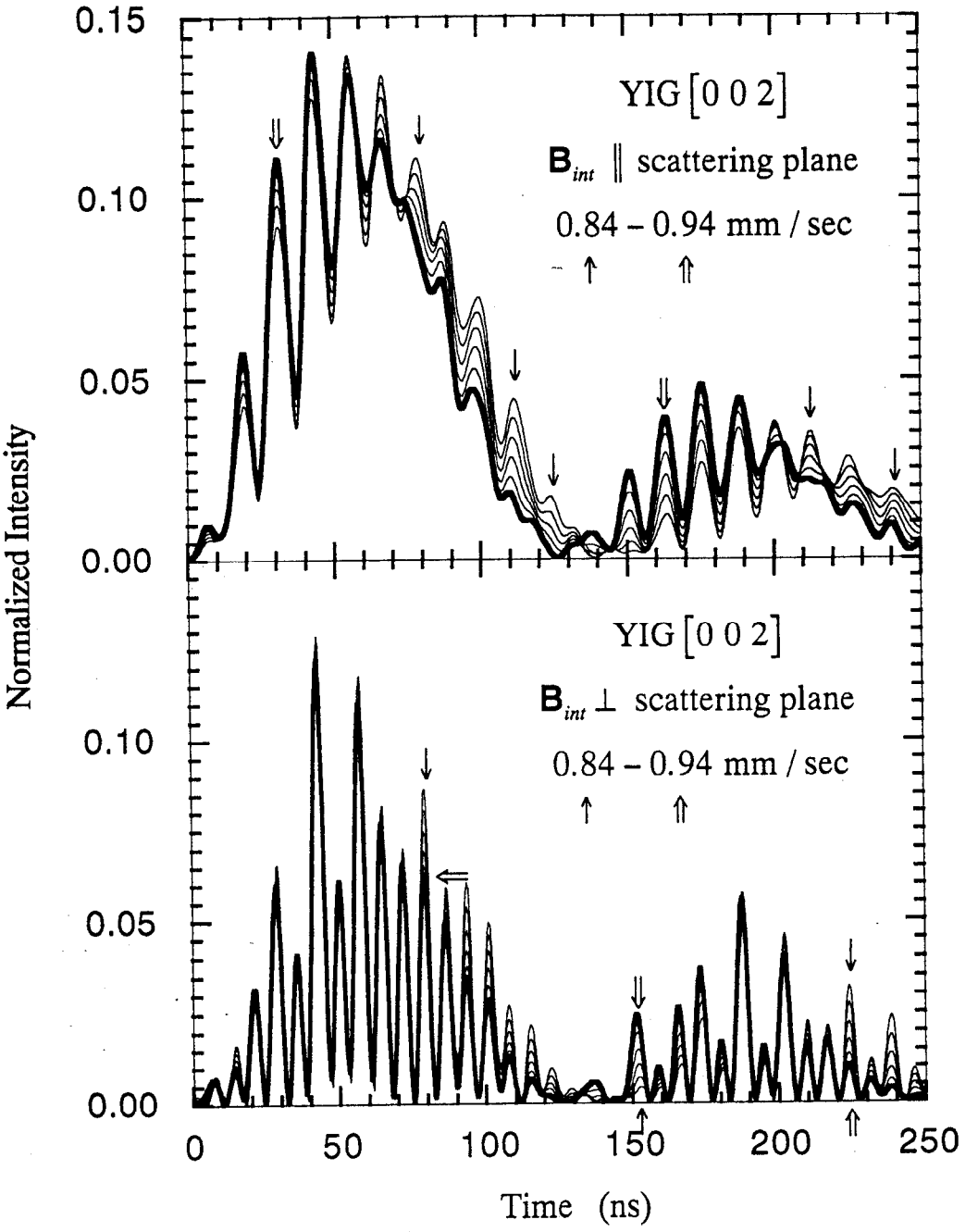

Fig. 10-2.2. YIG [0 0 2] time spectra for various electric quadrupole energy level shifts.

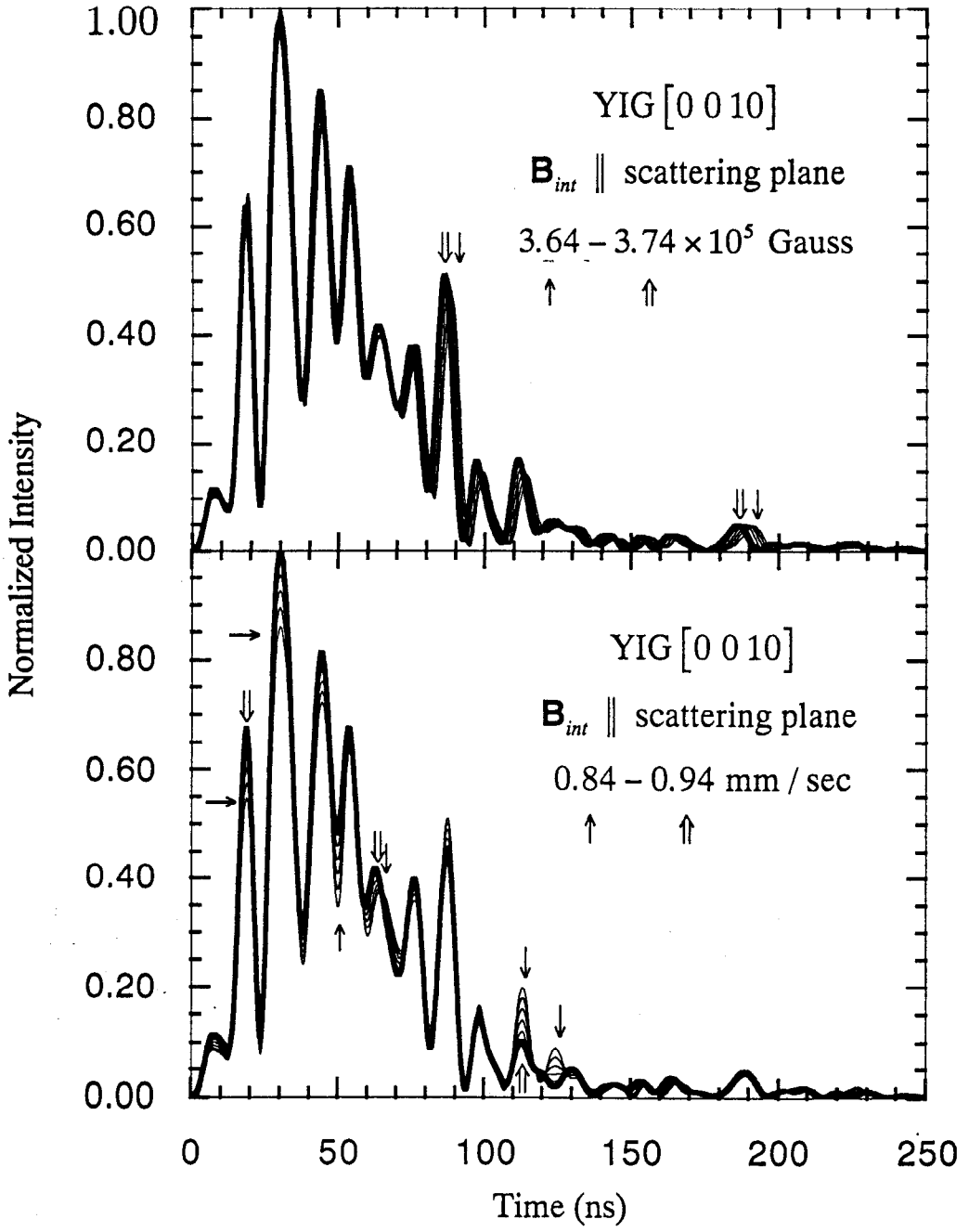

Fig. 10-2.3. YIG [0 0 10] time spectra for various magnetic field strengths and electric quadrupole energy level shifts.

Changes in the internal magnetic field strength dramatically affects the fast magnetic beat pattern. Changes in the electric quadrupole splitting factor, $e^2qQ/2$, dramatically affects the slow electric quadrupole beat pattern. Increasing the quadrupole splitting increases the energy spacing between lines ℓ_1 and ℓ_1' of the $d1$ and $d2$ iron sites (and also between lines ℓ_6 and ℓ_6' of the two d-sites). This leads to a decrease in the quadrupole beat period, and this shows up in Fig. 10-2.2 as a compression of the modulation envelope over the fast magnetic beats. Again, when operating far off the Bragg peak, small changes in $e^2qQ/2$ lead to striking changes in the overall beat pattern. Changes in the beat pattern due to changes in $e^2qQ/2$ of 1 neV are quite evident.

Many other factors can play a role in modifying the quantum beat patterns: variation of the magnitude of the internal hyperfine fields throughout the crystal film, nonuniformity of the applied magnetic field, depolarization of the magnetic dipoles, nonuniformity of the electric field gradient directions at each nuclear site, nonuniformity of the lattice spacing within the crystal film, the mosaic crystal spread, and the polarization of the incident field to name a few. One could probably fit any set of experimental data by varying an unlimited number of parameters. So, only a few factors that were known to have a significant effect were considered.

The polarization of the incident beam had to be considered in certain cases. Since the experiments were done on wiggler or undulator beam lines, elliptically polarized beams were not a problem (Furthermore, there was no strong evidence for elliptically polarized beams in the data. The result may have been different if a bending magnetic beam line was used since elliptically and even circularly polarized x-rays exist when operating above or below the plane of the electron orbit.). A partially unpolarized mix of horizontally polarized x-rays with a small amount of uncorrelated vertically polarized x-rays was considered in the hyperfine field analysis. A few examples of such a mixture containing 70 to 100% horizontally polarized x-rays is shown in Fig. 10-2.4. When the internal magnetic field is parallel to the scattering plane, an admixture containing up to 30% vertically polarized x-rays barely changed the beat pattern--only the sensitive null region near 70 nsec is affected. The beat pattern is significantly affected when the magnetic field is perpendicular to the scattering plane. This is not an unexpected result. When $\mathbf{B}_{int}$ is parallel to the scattering plane, both horizontally and vertically polarized x-rays can excite lines 1,3,4, and 6 which in turn radiate circularly polarized x-rays--horizontally and vertically polarized x-rays do about the same thing. When $\mathbf{B}_{int}$ is perpendicular to the scattering plane, horizontally polarized x-rays can excite lines 1,3,4, and 6, but vertically polarized x-rays can excite only lines 2 and 5. The beat period between lines 2 and 5

The other major factors considered were the mosaic spread of the crystal film and the angular distribution of the incident beam. Both of these factors were treated in a simple

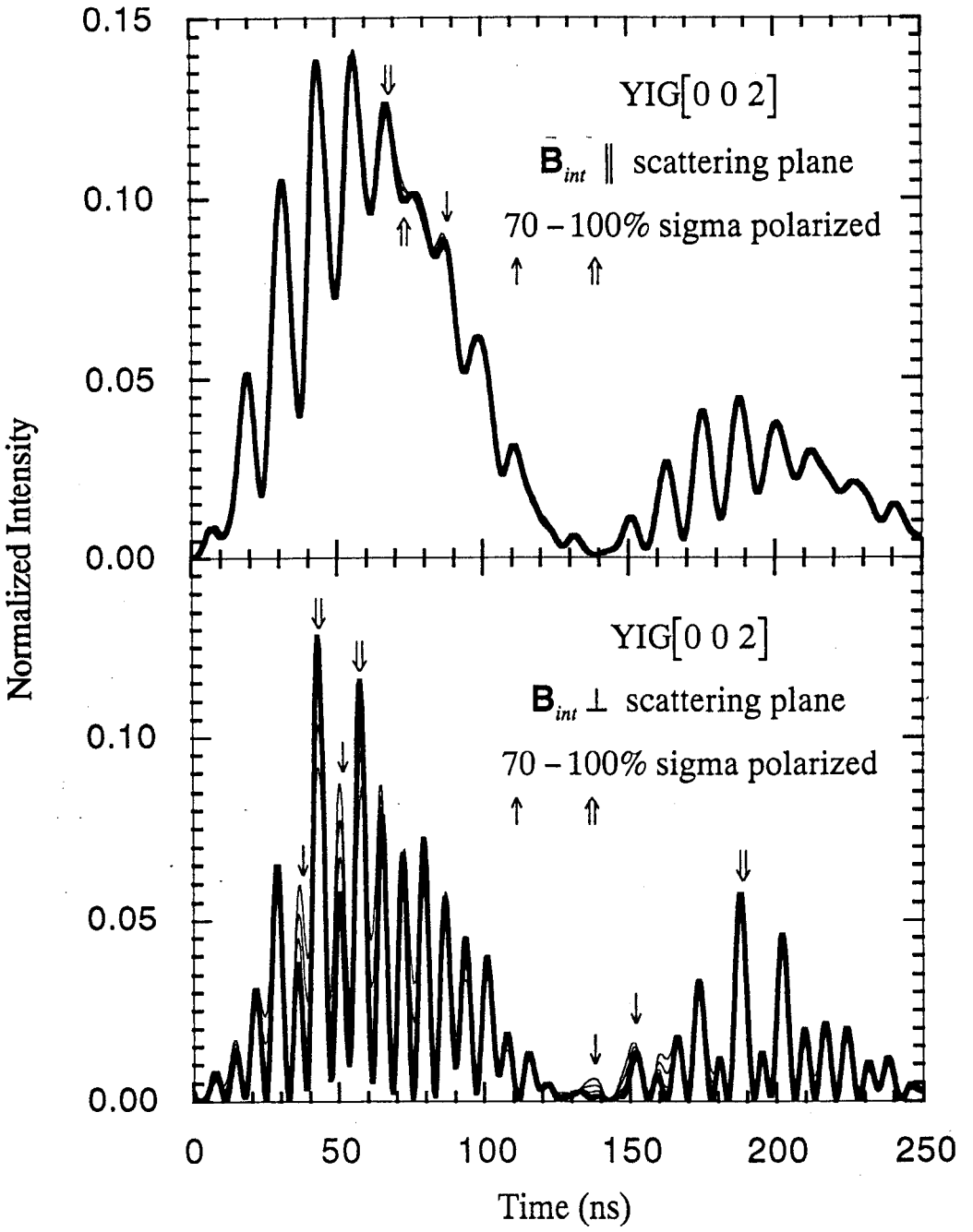

Fig. 10-2.4. Time spectra for various amounts of horizontally and vertically polarized x-rays.

The other major factors considered were the mosaic spread of the crystal film and the angular distribution of the incident beam. Both of these factors were treated in a simple fashion by performing a Gaussian angular average centered over the incident angle. Multiple time spectra were calculated at various incident angles, and the final fit was a Gaussian weighted average of each spectrum. This method takes into account both the angular divergence of the incident beam and the mosaic crystal spread of the YIG thin film.

The time resolution of the detector apparatus was handled by convolving a Gaussian pulse with the beat patterns. This is simply a Gaussian weighted time average, and its main effect is to partially wash out the oscillations in the beat pattern.

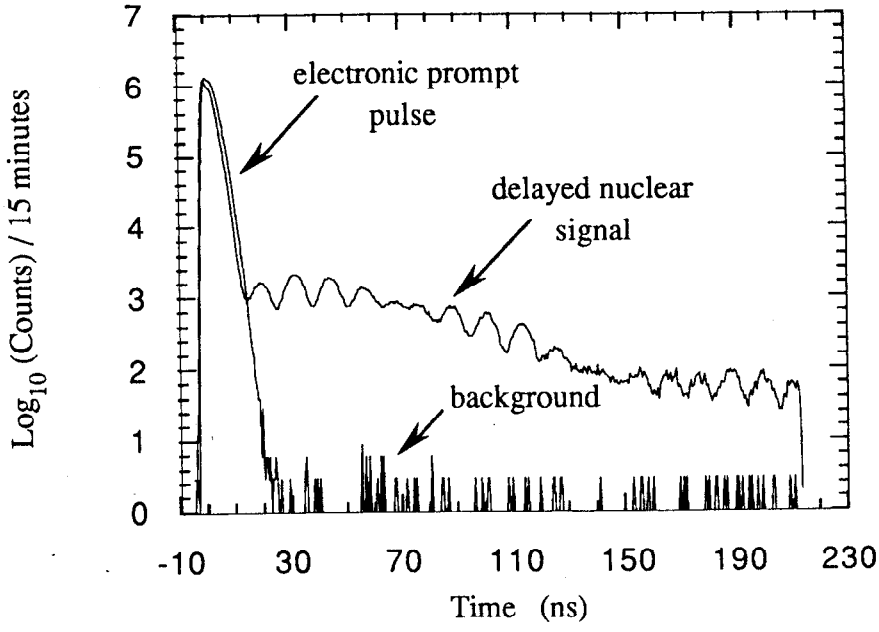

Fig. 10-2.5. Time spectrum along with the background. The background measurement was taken 5 eV above the 14412.5 eV nuclear resonance energy. The YIG [0 0 2] time spectrum was taken about 10 μrad above the Bragg peak with $\mathbf{B}_{int}$ parallel to the scattering plane. This is the second time spectrum ever to be taken at the PBF1 beamline at PEP (the very first was a rough demonstration measurement and was not used in the hyperfine field analysis).

No background subtraction was done to the data. The data was analyzed at a time long enough after the prompt excitation that the fluorescent signal from the photodetector's plastic scintillator was negligible--this was ensured by analyzing the data 25 nsec from the prompt pulse. Fig. 10-2.5 shows a typical beat pattern together with the prompt pulse. The width of the prompt pulse is quite wide (FWHM $\approx$ 4.3 nsec), but this was later found

out to be due to the TAC being overworked trying to process data at a prompt rate of 12,000 counts/sec. When the prompt rate fell to around 5,000 counts/sec, the prompt pulse width fell to a more respectable 2.5 nsec. The background run was done by tuning the monochromator energy 5 eV above the nuclear resonance energy. The background rate beyond 25 nsec was about 0.23 counts/sec. Compared to the delayed nuclear signal rate of roughly 190 counts/sec, the background can be safely ignored.

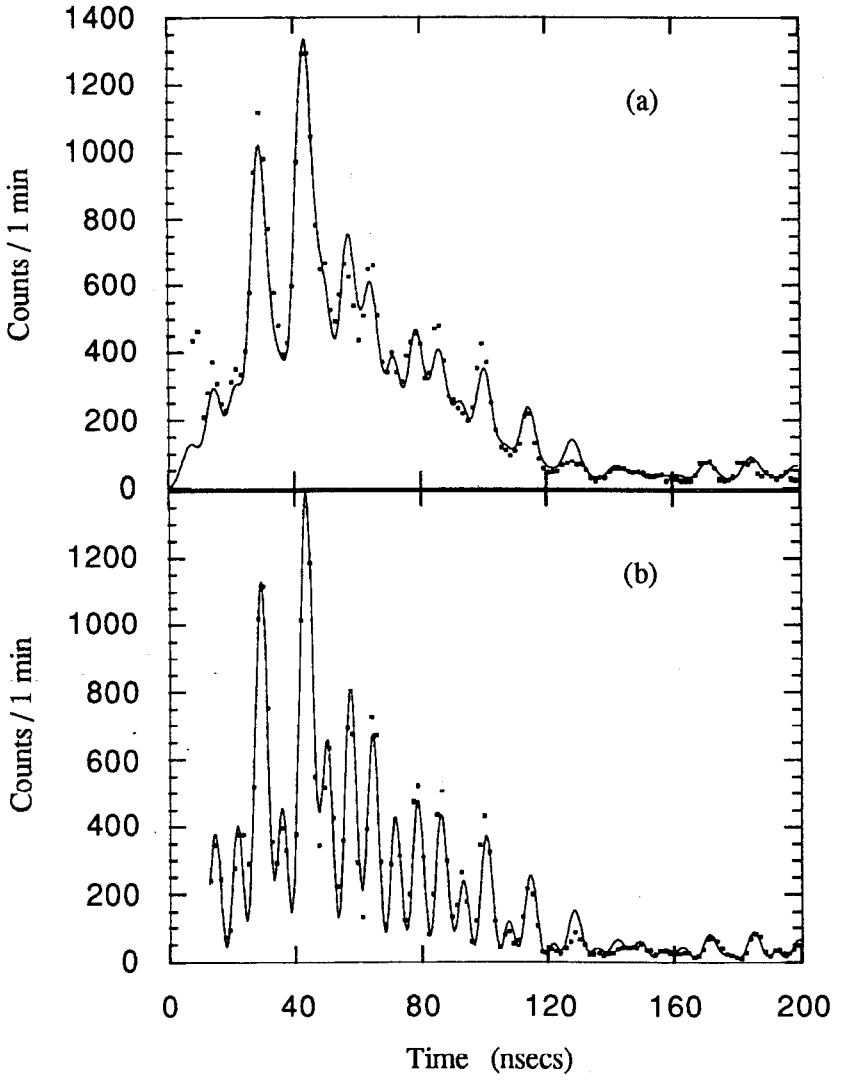

Fig. 10-2.6. Dramatic improvement in the time resolution of the measurements. Fig. (a) is a measurement without the veto signal in Fig. 9-3.3 to the coincidence logic unit; Fig. (b) is a measurement with the veto signal. By not overworking the TAC the time resolution was improved by a factor of two from 5 nsec to 2.5 nsec.

The data shown in Fig. 10-2.5 was taken without the veto signal to the coincidence logic unit shown in Fig. 9-3.3. This resulted in the TAC being overworked at high

counting rates and contributed towards broadening the time resolution of the measurements. By using the veto signal which allowed the TAC to be triggered only at times 10 nsec after the prompt pulse, the TAC could be used at high prompt rates without worsening the inherent time resolution of the photomultipliers. In such an arrangement, data as far back as 10 nsec after the prompt pulse can be measured with very low background rates, and the time resolution improves to around 2.5 nsec. This is shown in Fig. 10-2-6. The improvement in time resolution by a factor of two, however, did not change the values of the hyperfine field parameters used to fit the data. The improvement enabled small subtle effects to be seen in the time distribution. For instance, for data having a 7 nsec beat pattern blurred with a 5 nsec time resolution (see Fig. 10-2.6), the polarization content of the incident beam could not be determined when the crystal was positioned at the Bragg peak. However, he incident polarization content could be measured when the time resolution was reduced to 2.5 nsec.

For the hyperfine field parameters given in Tables 10-2.1 and 10-2.2 (B_{int} is the internal magnetic field strength and $e^2qQ/2$ is the electric quadrupole splitting factor), χ^2 fits were performed. Using a Fortran subroutine, VA02A, acquired from the Argonne National Labs computer center, a grid-gradient search algorithm for minimizing χ^2 was employed by varying 5 to 7 parameters: B_{int}, $e^2qQ/2$, the incident polarization distribution, the Gaussian angular and time resolution, the deviation angle from Bragg, and the starting time.

An analysis of 25 time spectra (from the Run #1 set in Table 10-2.1) where the deviation angle from the Bragg peak was less than $\pm 20\mu$rad and where 6 parameters were varied (the incident polarization was fixed to be 100% horizontally polarized) resulted in a Gaussian angular width (FWHM) of 21 ± 3 μrad--about 17% greater that the perfect Si crystal Darwin width. The fitting routine had a difficult time determining the angular resolution for time spectra taken at deviation angles greater that 20 μrad beyond the Bragg peak giving angular widths of up to 50 μrad, thus these spectra were omitted. The net angular resolution appears to be largely limited by the Darwin width of the Si monochromator (which is 18 μrad for perfect crystals) rather than by the mosaic spread of the YIG crystal.

For fits to all of the data in the tables below, the Gaussian angular resolution was fixed at 20 μrad, and only 6 parameters were varied (Except for the case where $\mathbf{B}_{int}$ was parallel to the scattering plane. The incident polarization was simply fixed to be 100% horizontally polarized since, as shown in Fig 10-2.4, such time spectra are insensitive to the polarization distribution). There was little coupling between the parameters--the

variation of one parameter to minimize χ^2 had little effect upon the value of the other parameters that minimized χ^2.

For data taken without the coincidence logic veto signal blocking out the prompt signal from the TAC, the time resolution was 4.1±0.8 nsec (This was compiled from the Run #1 data in Table 10-2.1 and from some of the Run #2 data in the same table. The Run #2 data was taken during a beamline run were the improvement in time resolution was tested and implemented). When the coincidence logic veto signal was used, the time resolution improved to 2.4±0.1 nsec (This was compiled from the data in Tables 10-2.1 and 10-2.2).

The polarization of the incident radiation differed at the PEP and CESR synchrotron ring beamlines. The polarization of the incident beam at the PBF1 undulator beamline at PEP was found to consist of 93±3% horizontally polarized radiation (the data in Table 10-2.1 taken during the two different runs gave the same result). At the F2 wiggler beamline at CESR the incident beam consisted of 84±2% horizontally polarized radiation. This decrease in polarization of the source beam may be due to the use of a wiggler rather than an undulator, and because the electron beam energy was lower at CESR than at PEP (5.5 GeV versus 14 GeV).

The hyperfine field parameters for the crystals labeled 57-2 and 57-6 are given in the Tables 10-2.1 and 10-2.2. An extensive investigation of the combined hyperfine interactions in YIG was made by Winkler through Mössbauer transmission spectroscopy measurements.[10] He found that for YIG single crystals 60 μm thick:

$$B_{int} = -399.9 \pm 1.5 \text{ kGauss} \quad \text{and} \quad e^2qQ/2 = -0.89 \pm 0.01 \text{ mm / sec}.$$

The YIG thin crystal films exhibit somewhat different hyperfine properties. For crystal #57-2, B_{int} is roughly 6% to 8% less than B_{int} for a pure single crystal, and, for crystal #57-6, B_{int} is smaller by 4%. The reduction in B_{int} is primarily due to the films being impregnated with a small amount of lead occupying the yttrium lattice sites. This has changed the local electrostatic and magnetostatic environment around the iron atoms and has resulted in a decrease in the internal magnetic field at the iron nuclei.

There is an interesting problem with crystal #57-2. For two different beamline runs different hyperfine fields were measured. B_{int} has increased by 2% and $e^2qQ/2$ has increased by 6% between Runs #1 and #2. Recall from Section 9.1 (see Fig. 9-1.2) that crystal #57-2 is a 6.7 μm thick crystal consisting primarily of 2 layers of YIG films having different lattice spacings. However, the data indicates that this crystal nonuniformity is not the reason for the difference in hyperfine fields between the two runs. The [0 0 2] reflection has a primary extinction length of 1.1 μm, thus these reflections probe only the

first micron of the crystal film. The χ^2 fits to the higher order reflections in both runs found that these reflections were probing a crystal film sublayer roughly 2.6 μm thick (see Section 11.4). Crystal #57-2 is then composed of two films 2.6 and 4.1 μm thick. Since the first micron of the crystal is uniform, the difference in B_{int} between Runs #1 and #2 for the [0 0 2] reflections is not due to thickness nonuniformity.

There is also reason to believe that a nonuniformity in the local hyperfine field environments across the surface area of the crystal is not responsible for the differences. As a result of the focusing properties of the upstream cylindrical mirror and the small Bragg angle, the incident beam lit up a stripe across the crystal 3 mm wide by 3 cm long for the [0 0 2] reflection. For the higher order reflections the area of this stripe substantially decreases--the [0 0 14] reflection lights up a stripe 3 mm wide by 1 mm long (the incident beam area was roughly 3×0.5 mm). However, the higher order reflections scanning ever smaller sections of the crystal area gave the same hyperfine parameters as the [0 0 2] reflection (as shown in Run #2). Nonuniformity of hyperfine fields across the crystal surface area is not evident in the data.

What may have occurred between the runs (which occurred $1\frac{1}{2}$ years apart) is that the crystal deteriorated to some degree. Some of the iron may have oxidized to become Fe_2O_3. The change in B_{int} is in the right direction (B_{int} for pure Fe_2O_3 is -515 kGauss) but the change in $e^2qQ/2$ is in the wrong direction ($e^2qQ/2$ for pure Fe_2O_3 is -0.12 mm/sec). The reason for the change remains unclear, but what is impressive is that 2% changes in the hyperfine field parameters is easily detectable through examining the quantum beat patterns.

Unlike crystal 57-2, crystal 57-6 is composed of a single layer of YIG (see Fig. 9-1.2). The χ^2 fit to the data yielded a thickness of 4.3±0.4 μm which is reasonably close to the expected value of 4.7 μm. The difference in hyperfine parameters between crystal 57-2 and 57-6 should be mainly due to the difference in lead concentrations in the two crystals. As a result of the odd behavior displayed by the other crystal, the effect of the lead upon the local electric quadrupole field is not readily determinable. $e^2qQ/2$ is 4% greater than Winkler's value for YIG, but there are large variations in this value stated throughout the literature (measured values varied from 0.78 to 1.03 mm/sec).[11-14]

Time-resolved spectroscopy is just as sensitive as Mössbauer velocity spectroscopy towards measuring hyperfine field parameters. They both can measure the hyperfine field values to within 1-2%. As a result, time-resolved spectroscopy was able to reveal subtle differences in the hyperfine properties of YIG between various thin film samples, and that these properties may slightly change over time for each thin film. Time-resolved spectroscopy using synchrotron x-rays may become more useful than Mössbauer spectroscopy when trying to measure the hyperfine fields of extremely small or very thin

Reflection	$\mathbf{B}_{int}$ direction	B_{int} (kGauss)	$e^2qQ/2$ (mm/sec)	# of time spectra
PEP Beamline Run #1				
[0 0 2]	∥	-369±2	-0.88±0.02	27
[0 0 2]	⊥	-369±1	-0.88±0.02	9
[0 0 6]	∥	-373±3	-0.87±0.02	1
[0 0 10]	∥	-373±2	-0.88±0.02	1
[0 0 10]	⊥	-370±2	-0.87±0.02	1
All reflections		-369±2	-0.88±0.02	39
PEP Beamline Run #2				
[0 0 2]	∥	-377±4	-0.93±0.04	1
[0 0 2]	⊥	-377±2	-0.94±0.01	7
[0 0 6]	∥	-374±3	-0.93±0.03	1
[0 0 6]	⊥	-376±2	-0.91±0.03	1
[0 0 10]	∥	-377±2	-0.92±0.01	2
[0 0 10]	⊥	-376±1	-0.93±0.02	1
[0 0 14]	∥	-376±2	-0.92±0.02	1
[0 0 14]	⊥	-376±1	-0.94±0.02	1
All reflections		-376±1	-0.93±0.01	15

Table 10-2.1. Hyperfine field parameters for crystal # 57-2. The uncertainties for each set of data represent the square root of the variance in the data using a weighted average for the mean. For each individual time spectrum the uncertainty in the parameters represents what it takes to produce a 10% change in the χ^2 minima. $\mathbf{B}_{int}$ is either parallel or perpendicular to the scattering plane.

Reflection	$\mathbf{B}_{int}$ direction	B_{int} (kGauss)	$e^2qQ/2$ (mm/sec)	# of time spectra
[0 0 2]	∥	-384±2	-0.95±0.01	2
[0 0 2]	⊥	-384±4	-0.96±0.04	1
[0 0 10]	⊥	-383±1	-0.96±0.01	2
All reflections		-383±1	-0.95±0.01	5

Table 10-2.2. Hyperfine field parameters for crystal # 57-6. The data was taken at the CESR F2 wiggler beamline.

materials consisting of just a few nuclei or a few layers of nuclei. Such materials would produce signals that are too weak to be measurable by Mössbauer spectroscopy techniques. However, time-resolved spectroscopy performed at future third generation synchrotrons having high powered undulator or wiggler insertion devices will provide way of probing such exotic materials.

10.3 Low Temperature Measurements

A low temperature experiment was performed to examine the scattering and hyperfine properties of YIG.[15] The crystal was mounted in a cryostat centered on a four circle diffractometer as explained in Section 9.2. Measurements were made at room temperature and at 150°K. A temperature controller was used to stabilize the temperature during the course of the measurements. The results are shown in Fig. 10-3.1.

One unexpected result can be quickly noticed in the two measurements shown in Fig. 10-3.1. Both measurements were taken for the same length of time, but the low temperature measurement has a much lower count rate than the room temperature measurement (17 counts/sec versus 110 counts/sec, or a factor of $6\frac{1}{2}$ times less). What was expected was an increase in counting rate as the temperature decreases because the Lamb-Mössbauer factor, or recoilless fraction of resonant nuclei, increases to the limit of unity as the number of phonon modes goes to zero. A cause for this discrepancy may be because the YIG crystal is a thin film epitaxially grown on a GGG substrate. There is naturally some strain in the film since YIG and GGG have different lattice constants. Going to low temperatures may have magnified these strains and caused the film to distort, or warp, resulting in the much lower counting rates. The measurement was done with crystal #57-2 before having any accurate knowledge of its structure. During or after the fabrication process, the crystal bifurcated due to lattice mismatching problems. What these results suggest is that YIG films thinner than 2.5 μm grown on GGG are not good samples to do low temperature perfect crystal diffraction experiments.

Though the crystal diffracts poorly at low temperature, the hyperfine parameters could still be measured and were found to be very different than the room temperature values. The internal magnetic field strength increased by 15% to 429 ± 4 kGauss when the temperature was lowered to 150°K. The value of B_{int} at low temperatures does not significantly depart from measurements made by others--Mössbauer transmission measurements at 85°K yielded values of B_{int} ranging from 460 to 467 kGauss, and a nuclear magnetic resonance measurement at 77°K yielded 468 kGauss (these were all done

on pure YIG polycrystalline samples).[16-18] Extrapolating to 150°K using the careful NMR measurements of Ogawa gives a value of 452 kGauss.[18] This is about 5% greater than the thin film measurement, and, since the room temperature measurements are about 7% greater than the thin film measurements, this difference is not unreasonable.

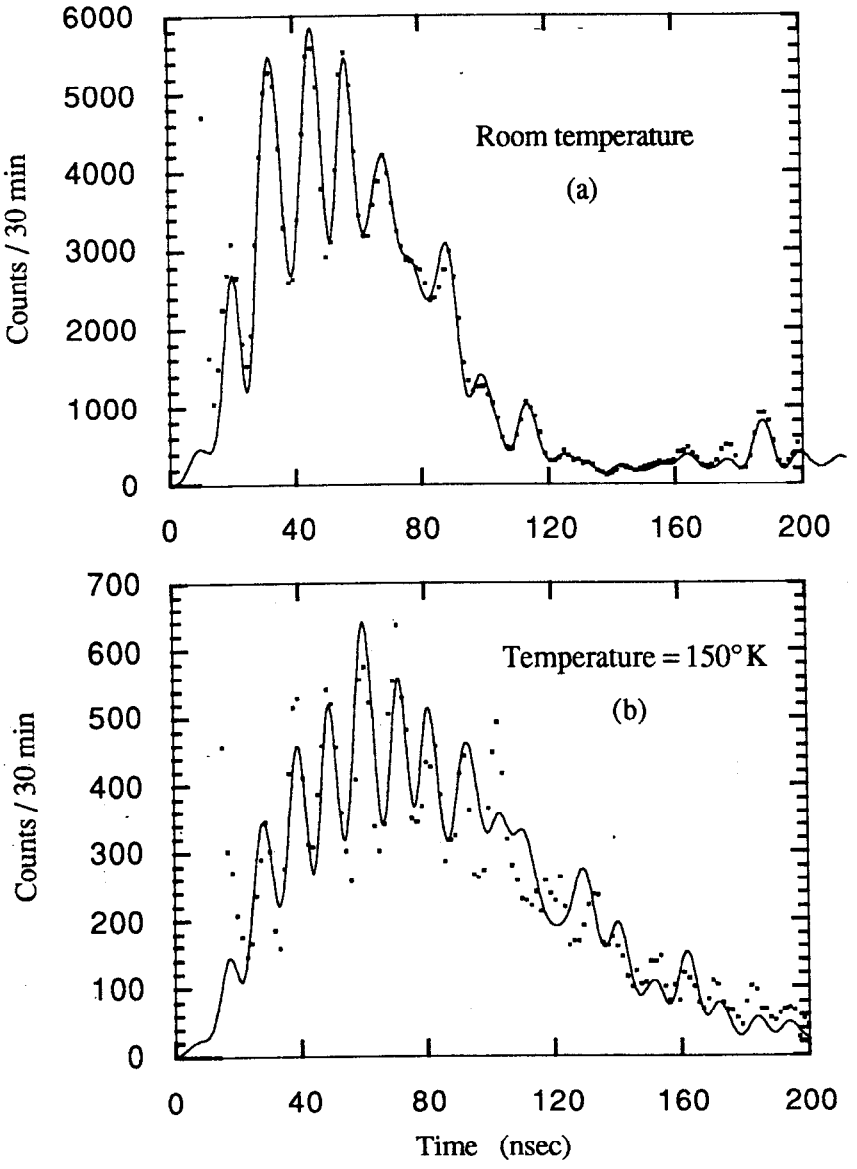

Fig. 10-3.1. Time spectra for [0 0 10] reflection at (a) room temperature and at (b) 150°K. $\mathbf{B}_{int}$ is parallel to the scattering plane and the crystal surface. At room temperature $B_{int} = -373 \pm 2$ kGauss and $e^2qQ/2 = -0.88 \pm 0.02$ mm / sec. At 150°K $|B_{int}|$ increased 15% to 429 ± 4 kGauss and $|e^2qQ/2|$ decreased 61% to 0.54 ± 0.04 mm / sec.

The electric quadrupole splitting factor decreased almost by half (61%) to 0.54 ± 0.04 mm/sec when the temperature was lowered to 150°K. The temperature dependence of $e^2qQ/2$ has apparently not been explored in detail experimentally since there is little information about it in the literature. Most early temperature dependence experiments have been done with polycrystals since they were easier to obtain, and these experiments examined the behavior of only the internal magnetic field. Since the direction between the electric field gradient and the magnetic field is completely random for a polycrystal, the electric quadrupole splitting should average to zero, thus no reliable value of $e^2qQ/2$ can be measured. This problem can be overcome by applying a sufficiently strong external magnetic field to remagnetize the polycrystal--in this case the angle between $\mathbf{B}_{int}$ and the electric field gradients is random and can be averaged over to obtain fits to the data. This was done to YIG polycrystals at room temperature (the external magnetic field strength was 20 kGauss), and quite accurate values of $e^2qQ/2$ were extractable from the data.[13] However, there is no account in the literature of using this procedure to find the temperature dependence of $e^2qQ/2$.

10.4 Angular Interferometry: Observation of the Phase Shift of a Rotated Quantum State

Scattering angle dependent quantum beat interference has been used to examine the phase shift of a quantum state that has undergone a rotation. A physical interpretation of this effect using the scattering theory formalism developed in Chapter 4 is given in Section 5.5. From a different perspective, the angular phase shift can be understood from basic rotational and mirror symmetry properties of free space[19] (see Appendix A.1).

The YIG $[0\,0\,10]$ reflection was chosen to get the maximum effect. In the experiment at the CESR beamline, the internal magnetic field was oriented, by using an external guide field, in the two antiparallel directions perpendicular to the scattering plane, and the net phase difference between the time beat patterns for the two orientations of the magnetic field was measured. Changing the direction of the magnetic field was equivalent to performing a $[0\,0+10]$ and a $[0\,0-10]$ reflection. This was observed during experiments at the PEP beamline where upward and downward reflecting experiments (without changing the direction of the magnetic field) gave phase shifts equivalent to orienting an internal magnetic field in the two antiparallel directions perpendicular to the scattering plane (without changing the orientation of the crystal).

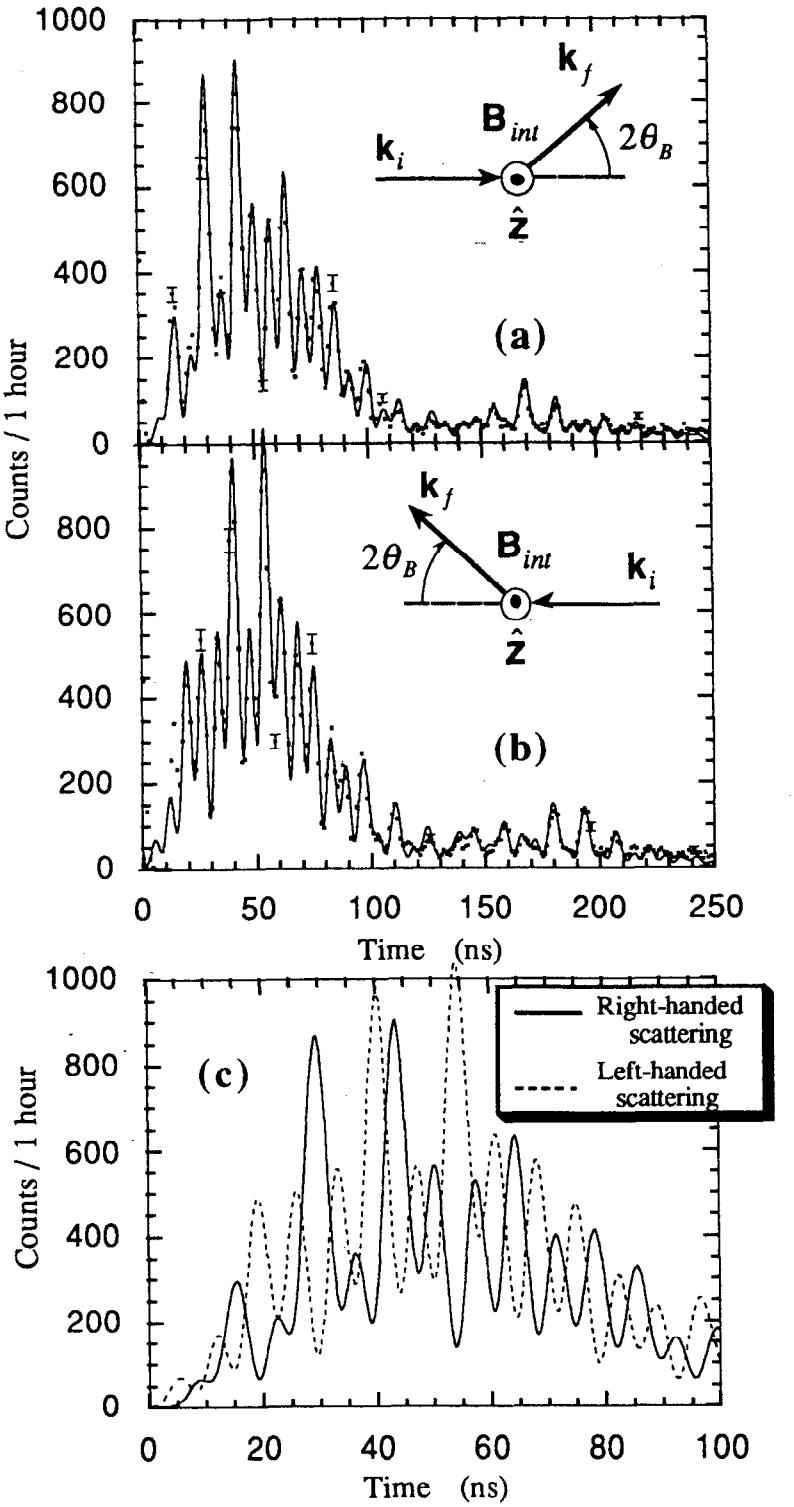

Fig. 10-4.1. Quantum beat patterns of YIG [0 0 10] reflections for (a) right-handed scattering and (b) left-handed scattering. (b) Calculated fits to the data are shown superimposed and expanded. The nearly 180° phase shift is clearly evident.

The results of the CESR beamline experiment is shown in Fig. 10-4.1. Note that in the diagram in Fig. 10-4.1 (a) the incident photon is rotated in a right-handed sense in going from $\mathbf{k}_i$ to $\mathbf{k}_f$--this will be called right-handed scattering. Left-handed scattering is illustrated in the diagram in Fig. (b) where the incident photon is rotated in a left-handed sense in going from $\mathbf{k}_i$ to $\mathbf{k}_f$. The Bragg angle for the YIG [0 0 10] reflection is about 20°. Diffraction from this reflection results in a net phase difference, $\Delta\varphi = 8\theta_B$, of 160° between the quantum beat patterns of left and right-handed scattering. As can be seen in Fig. 10-4.1 (c), the peaks of one beat pattern lie almost in the valleys of the other beat pattern. This dramatically illustrates the angular phase a photon acquires upon undergoing an angular momentum conserving rotation.[19]

As can be seen in Fig. 10-4.1, more is going on than the phase shifts discussed above, for the overall shapes of the beat patterns for left and right-handed scattering are not the same. The reason for this can be understood by examining Table 10-1.2. The quantum beats with the largest amplitudes comes from the interference between lines 1 and 6 having a beat period of 7 nsec (averaging over the two iron d-sites in the crystal). Since these lines have a total angular momentum component of $M = \pm 1$, they contribute to the $4\theta_B$ phase shift of the right or left-handed scattered photons that is observed in the experiment. However, there are 24 other beats affecting the net quantum beat pattern. Of these, 12 occur from pairs of lines having the same value of M. There is no phase shift for pairs of lines having identical M values, thus the phase shifted, dominant 7 nsec beat pattern is modulated by unshifted, though less dominant, beat patterns (having an average beat period of 130 nsec and 11 nsec). This additional unshifted amplitude modulation causes the difference in the shape of the beat patterns for right and left-handed scattering. For the [0 0 2] reflection where the net phase shift is negligible ($8\theta_B = 32°$ corresponds to a shift in time of $\frac{1}{2}$ nsec which is unobservable for detectors having a resolution of 2.5 nsec), these amplitude variations are the only predominant differences between left and right-handed scattering (see Fig. 10-4.2).

In addition to the perturbations upon the 7 nsec beat pattern, there are dynamical effects, such as resonance frequency shifts and decay rate speedups, that modify the beat pattern. Thus, to get good fits to the data, the full nuclear dynamical diffraction theory was applied. However, as can be noticed in Section 5.5, the angular phase shifts can be calculated using kinematical, or single particle, scattering theory.

Note that the scattering diagram in Fig. 10-4.1 (a) shows a scattering interaction that appears to be time reversed from that shown in the scattering diagram in Fig. 10-4.1 (b). A physical process and its time reversed process should give identical experimental results unless time reversal symmetry is broken. Since the time beat patterns

for the two scattering processes are different, time reversal symmetry appears to be violated. This perplexing problem is resolved by noting that the magnetic field behaves as a pseudovector that is odd under time reversal. Thus, the actual time reversed process of the diagram in Fig. (a) is the diagram in Fig. (b) with the magnetic field changed in sign to point in the opposite direction (into the page instead of out of it)--this gives back the scattering diagram in Fig. (a), and time reversal invariance is upheld.

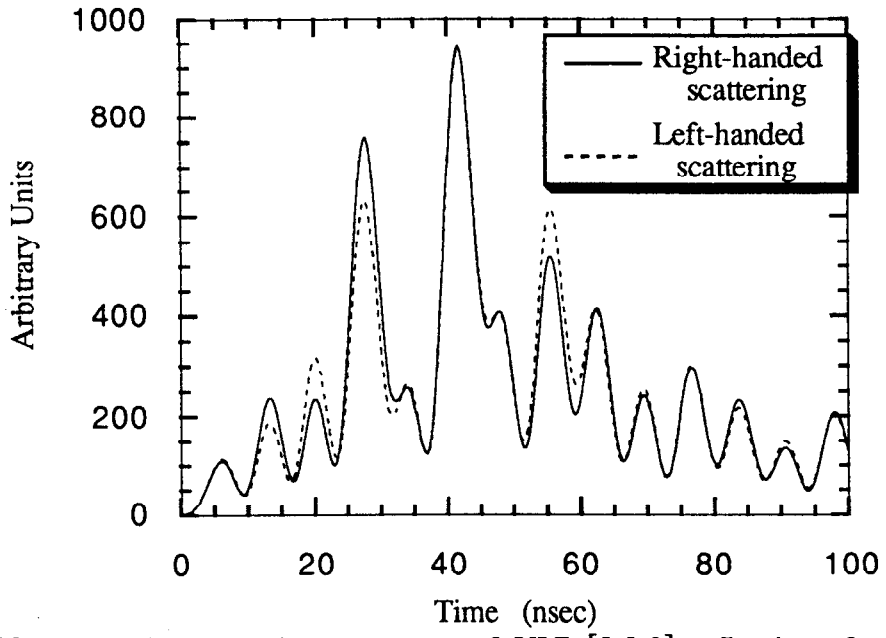

Fig. 10-4.2. Quantum beat patterns of YIG [0 0 2] reflections for right-handed scattering and left-handed scattering. The phase shift is imperceptible, but the amplitude variations between the patterns are noticeable.

This characteristic of magnetic fields makes them a common source of problems when trying to investigate the breaking of time reversal symmetry in physical interactions.

One interesting result from these angular interferometry experiments is that the sign of the internal magnetic field can be uniquely determined. Right-handed rotations of the photon quantum state about the quantization axis (which is the internal magnetic field direction) gives rise to quantum interference patterns that are phase retarded by $4\theta_B$. Left-handed rotations lead to quantum interference patterns that are phase advanced by $4\theta_B$. Finding which pattern is advanced or retarded in phase immediately gives the sign of the internal magnetic field. Upon careful examination of the [0 0 10] data in Fig. 10-4.1, the internal magnetic field at the iron d-sites was verified to be oriented antiparallel to the

externally applied magnetic field (this would have been more easily seen by going to a reflection that did not give nearly 180° net phase shifts).

REFERENCES

[1] E. B. Alexandrov, *Opt. Spectrosc.* **17**, 957 (1964).

[2] J. N. Dodd, R. D. Kaul, and D. M. Warrington, *Proc. Phys. Soc. (London)* **84**, 176 (1964).

[3] W. Gornik, D. Kaiser, W. Lange, J. Luther, and H. H. Schulz, *Opt. Comm.* **6**, 327 (1972).

[4] S. Haroche, J. A. Paisner, and A. L. Schawlow, *Phys. Rev. Lett.* **33**, 948 (1974).

[5] S. Haroche, *High-Resolution Laser Spectroscopy* , edited by K. Shimoda, (Springer Verlag, Berlin, 1976), p. 253.

[6] S. Haroche, M. Gross, and M. Silverman, *Phys. Rev. Lett.* **33**, 1063 (1974).

[7] C. Fabre, M. Gross, and S. Haroche, *Opt. Comm.* **13**, 393 (1975).

[8] A. Hese, A. Renn, and H. S. Schweda, *Opt. Comm.* **20**, 385 (1977).

[9] E. Gerdau and R. Rüffer, *Hyp. Int.* **27**, 59 (1986).

[10] H. Winkler, R. Eisberg, E. Alp, R. Rüffer, E. Gerdau, S. Lauer, A. X. Trautwein, M. Grodzicki, and A. Vera, *Z. Phys. B* **49**, 331 (1983).

[11] C. Alf and G. K. Wertheim, *Phys. Rev.* **122**, 1414 (1961).

[12] I. I. Nikolaev, L. S. Pavlyukov, and V. P. Mar'in, *Sov. Phys. Solid State* **17**, 1016 (1975).

[13] G. N. Belozerskii, Y. P. Khimich, and V. N. Gitsovich, *Phys. Stat. Sol. (b)* **79**, K125 (1977).

[14] V. N. Belogurov, V. A. Bylinkin, and V. I. Mosel, *Izv. Akad. Nauk. Latv. SSR* **3**, 3 (1979).

[15] J. Arthur, D. E. Brown, S. L. Ruby, G. S. Brown, and G. K. Shenoy, *J. Appl. Phys.* **67**, 5704 (1990).

[16] R. Bauminger, S. G. Cohen, A. Marinov, and S. Ofer, *Phys. Rev.* **122**, 743 (1961).

[17] S. S. Bashkirov, N. G. Ivoilov, and V. A. Chistyakov, *Sov. Phys. Solid State* **13**, 570 (1971).

[18] S. Ogawa and S. Morimoto, *J. Phys. Soc. Jpn.* **17**, 654 (1962).

[19] D. E. Brown, J. Arthur, A. Q. R. Baron, G. S. Brown, and S. Shastri, *Phys. Rev. Lett.* **69**, 699 (1992).

11. DYNAMICAL EFFECTS

11.1 Radiative Speedup

The nuclear hyperfine quantum beats are one of the most striking kinematical effects seen in the nuclear resonance time spectra. Similarly, one of the most dramatic dynamical effects seen in the nuclear resonance time spectra is the nuclear decay rate speedup. Rather than decaying with the lifetime of an isolated excited-state ^{57}Fe nucleus (which is 141 nsec), a group of ^{57}Fe nuclei, for a single photon interaction, behaves as an excited collective state that decays much faster than an isolated nucleus. This single photon quantum effect has been discussed in Sections 7.6 and 7.7.

As shown in Figs. 7-6.6 to 7-6.8, the collective total nuclear decay rate varies as a function of time. This is due to the non-Lorentzian nature of the collective nuclear resonance frequency response. Actually, there are two decay rate speedup factors: Γ_s resulting from forward scattering in the crystal and is important at early times, $\Omega_{s\alpha}$ resulting from Bragg diffraction and is important at intermediate times, and both speedup factors are important at later times. Also, the definition of short, intermediate, and long times varies as a function of the deviation from the Bragg diffraction peak. An additional complication arises from hyperfine split nuclei. As shown in Fig. 7-7.1, the speedup factors are different for lines possessing different Clebsch-Gordan coefficients (see Eqs. 7-7.1 and 7-7.2). Thus, in the frequency domain, different lines can be homogeneously broadened in a non-Lorentzian fashion by different amounts at different deviation angles from Bragg.

The YIG crystal increases the complexity one notch further. Even for the simplest scattering geometries described in Section 10.1, there are up to 8 different resonance lines. Unambiguously clear dynamical speedup effects are therefore unobtainable from the YIG quantum beat spectra (to date, no single line crystals have been fabricated--such crystals would enormously simplify the task of observing clear dynamical effects).

Rather than trying to extract dynamical speedup factors such as $\Omega_{s\alpha}$ or Γ_s from the data, an effective average speedup rate is determined. To do this, the time spectra for YIG [0 0 2] reflections at different deviation angles were fitted with a simple function

$$I(t) = I_0 e^{-(s+\Gamma)t/\hbar} \sin^2\left(\Delta\omega_{EQ} t/2\right) \qquad (11\text{-}1.1)$$

where $s/\hbar$ is the effective average speedup rate, and $\Delta\omega_{EQ}$ is the average electric quadrupole beat frequency due to the electric quadrupole splitting between the $d1$ and $d2$-sites (scattering geometries, described in Section 10.1, were chosen to make these the only sites contributing to a diffracted field). In this simple approximation to the time spectra, the magnetic hyperfine quantum beats are averaged away.

Typical fits for deviation angles below, at, and above the Bragg diffraction peak are shown in Fig. 11-1.1 where the internal magnetic field was oriented perpendicular to the scattering plane. The full nuclear dynamical diffraction theory was used to get the best fit to the data, and the fit is shown by the solid curve that closely follows the fast magnetic beats in the data. The modulation envelope that is characterized by a slow electric quadrupole beat is the fit of Eq. 11-1.1 to the data. The third curve presented in each figure characterizes what would happen if there were no magnetic dipole or electric quadrupole beats and no speedup. This curve is essentially the resonance exponential decay curve for an isolated nucleus:

$$I(t) = I_0 e^{-\Gamma t/\hbar}. \tag{11-1.2}$$

When there is no speedup, the single nucleus decay curve is tangent to the peaks of the electric quadrupole beat curve, Eq. 11-1.1. This can be almost seen in Fig. 11-1.1 (a) where the speedup is only about a third of the single nucleus total decay rate.

All of the curves have been normalized to the data closest to the Bragg peak (Fig. 11-1.1 (b) where $\delta\theta = +2\mu$rad). At the Bragg peak, the diffracted intensity and the speedup maximizes. This is where the spatial phases of the electric fields scattered from the lattice of nuclei are all the same, and thus the collective, cooperative effect becomes prominent. As the crystal is rotated off the Bragg peak, spatial dephasing among the scattered fields occurs, and this results in diminishing the collective, cooperative effect among the nuclei--the speedup is therefore reduced.

The variation of speedup with angle is shown in Fig. 11-1.2 for the scattering geometries where the internal magnetic field is parallel and perpendicular to the scattering plane. The decay rate speedup tends to be greater when $\mathbf{B}_{int}$ is parallel to the scattering plane rather than perpendicular to the scattering plane. This occurs because the polarization matrices for the two orientations are different and give a larger nuclear structure factor when $\mathbf{B}_{int}$ is parallel to the scattering plane (see Eqs. 7-2.1, 5-1.22, and 5-1.28).

Since, in theory, the dynamical speedup factor follows a Lorentzian distribution as a function of deviation angle from Bragg, the data was fitted with a Lorentzian function. For the perpendicular (parallel) case the fit yielded a Bragg peak at $68 \pm 8\mu$rad ($67 \pm 3\mu$rad) which, within the uncertainty, agrees with the predicted value of 68μrad --

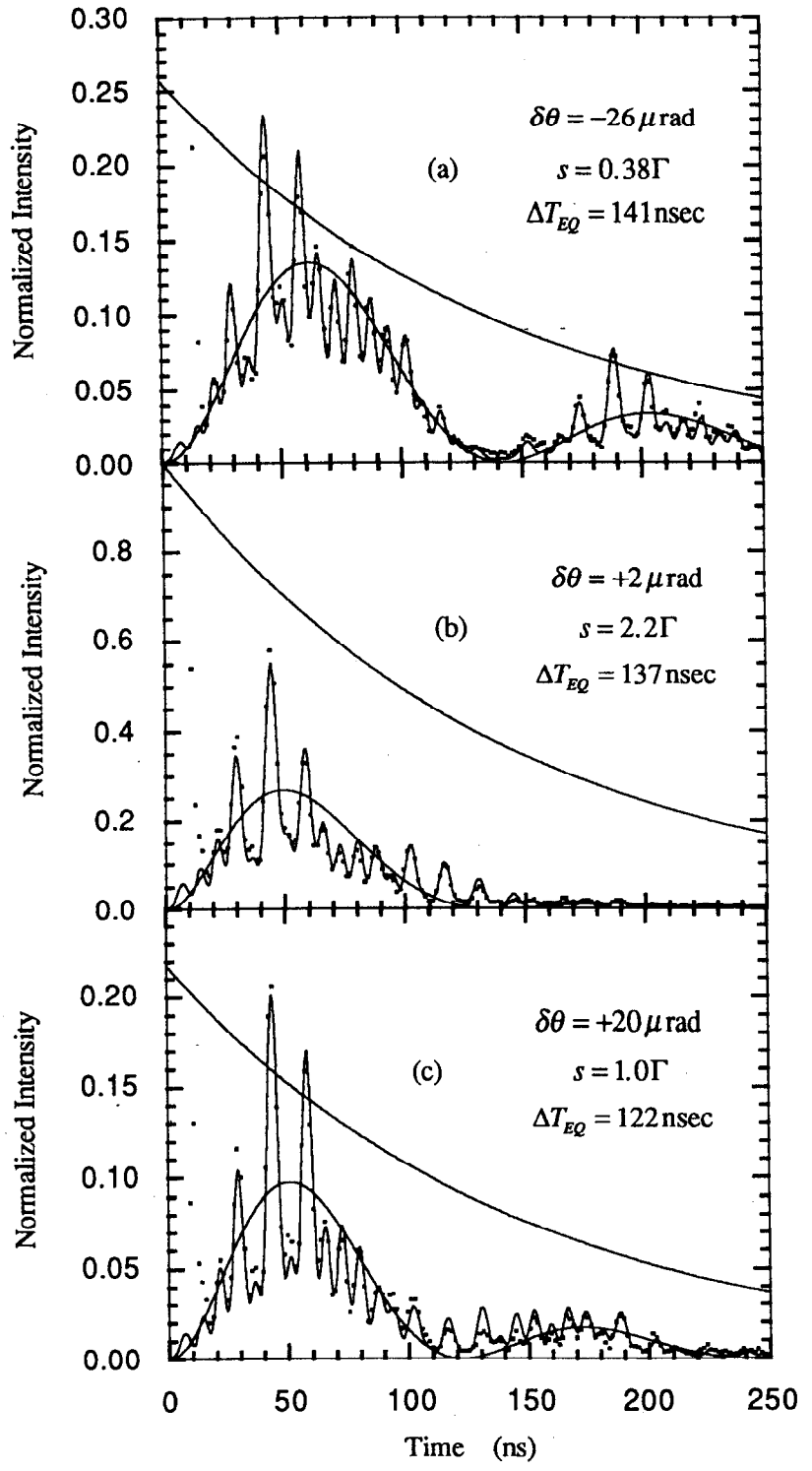

Fig. 11-1.1. YIG [0 0 2] quantum beat patterns for various angles near the Bragg peak: (a) -26μrad (b) $+2\mu$rad, and (c) $+20\mu$rad from the angle corresponding to the Bragg peak. The exponential decay curve is Eq. 11-1.2, the curve with slow beats is Eq. 11-1.1, and the data is fit using the full nuclear dynamical diffraction theory. The average electric quadrupole quantum beat period is ΔT_{EQ}, and s is the average decay rate speedup.

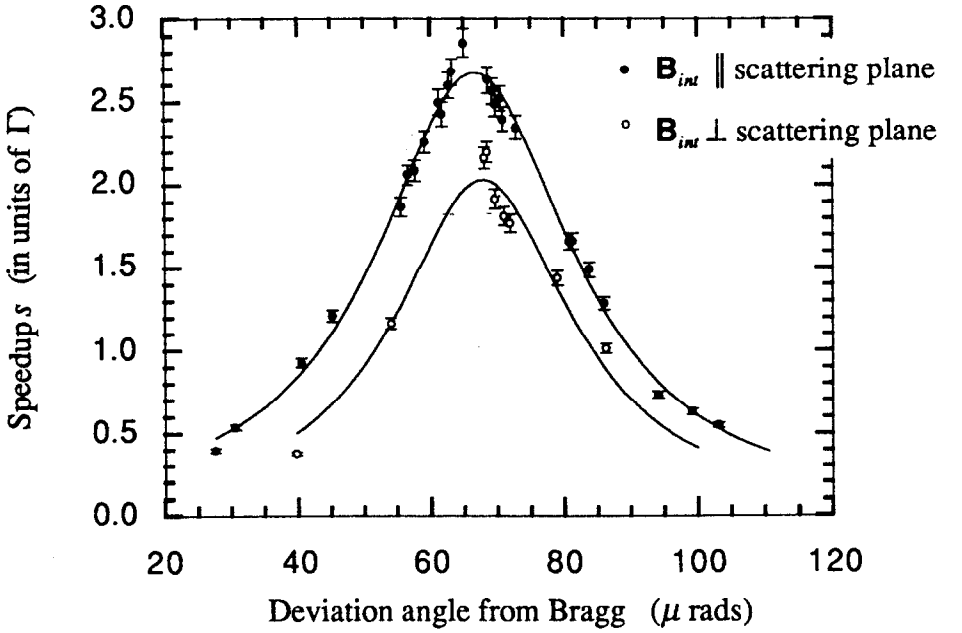

Fig. 11-1.2. A plot of the average speedup, s, versus the deviation angle from Bragg. At the Bragg peak, when $\mathbf{B}_{int}$ is parallel to the scattering plane, the average total decay rate is roughly 4 times as fast, and it becomes 3 times as fast when $\mathbf{B}_{int}$ is perpendicular to the scattering plane. All data was fitted with a Lorentzian function.

this is the position of the nonresonant Bragg peak. The angular linewidth was measured to be $32 \pm 20 \mu$rad ($36 \pm 11 \mu$rad). The large uncertainties for the perpendicular case result from collecting too few data points on the low angle side of the peak. On the basis of the fits, one can assume that s follows a Lorentzian angular distribution centered at the Bragg peak.

The average speedup, s, is not to be confused with the dynamical speedup factors. Even when factoring in the 20μrad angular resolution in the data, the dynamical speedup factors are much greater than the average speedup. This can be seen by examining Fig. 7-1.7 (c) (one can neglect lines 3 and 4 since they have small scattering amplitudes compared to lines 1 and 6). Thus, near the Bragg peak, the dynamical speedup factors $\Omega_{s\alpha}$ and Γ_s do not describe the effective speedup of the quantum beat spectra (one could have inferred this from examining the collapse in the resonance width near the Bragg peak as shown in Fig. 7-6.4). At the Bragg peak the effective speedup is considerably smaller than the dynamical speedup factors. Also, the effective speedup may only increase marginally if the angular divergence of the incident beam is decreased significantly from the 20μrad that existed for these measurements.

11.2 Resonance Frequency Shifts

The other remarkable feature that stands out in the nuclear hyperfine quantum beat patterns are resonance frequency shifts. As discussed in Section 3.7, a single nucleus interacting with its own self-fields gives rise to frequency shifts. In a similar manner, the collective state of a distribution of nuclei interacts with its own self-fields which, in this case, are the multiply scattered fields in the medium. This cooperative interaction among the nuclei gives rise to a collective resonance frequency shift. This effect has been observed in the frequency domain through careful Mössbauer experiments by van Bürck.[1] In the time domain, this effect is much more dramatic and significantly modifies the time spectra.

The same problems encountered in trying to examine the dynamical speedup factors $\Omega_{s\alpha}$ and Γ_s discussed in Section 11.1 are present when trying to extract the characteristics of the dynamical frequency shift factor, ω_s, from the quantum beat data (except, fortunately, that the collective resonance frequency shift does not vary with time)--the non-Lorentzian resonance behavior, the variation of ω_s with the deviation angle from Bragg and for lines with different scattering amplitudes, and the plethora of hyperfine lines from YIG.

Determining the precise behavior of the collective resonance frequency shift becomes even more intractable because there are a myriad of other effects that can cause the resonance lines to shift about. For instance, the theory that gave rise to ω_s in Section 7-6 and 7-7 had some approximations made: that the crystal was infinitely thick and had a single resonance line. Neither of these cases hold for the YIG crystals used in the experiments. The effects of crystal thickness are discussed in Section 11-4. When there are two or more resonances, coupling can occur between them and produce phase shifts in the time spectrum [2,3](see Appendix B.2), and, when the resonances are close together, the resonant lines can interfere with each other enough to shift the peak intensities of each resonance line.

The spectator iron atoms occupying the a and $d3$-sites also modify the frequency and time spectra. The a-sites have little effect upon the time spectra since, because their internal magnetic field strengths are much larger that those for the d-sites, their resonance lines interact little with the d-site resonance lines. However, the resonance lines of the $d3$-site lie at the same energies as the lines of the $d2$-site because they have the same quadrupole energy shifts. Because the geometrical structure factor for the $d3$-site is zero, this site does not reflect any fields and only transmission can occur. This transmission channel opens up another avenue for an incident photon to escape through rather than

traveling in the reflection channel of the $d2$-site. The interaction between the $d2$ and $d3$-sites in the frequency domain is shown in Fig. 11-2.1. In the figure the reflected fields from the $d1$ and $d2$-sites are shown--their hyperfine resonance lines are shifted from each other because they have different electric quadrupole energy shifts. However, the amplitude of each pair of lines should be identical. Yet the figure shows that for each pair of closely spaced lines the $d2$-line typically has a smaller amplitude. The reduction in amplitude of the $d2$-line is the result of photons being diverted into the transmission channel opened up by the $d3$-site. This interaction between the $d2$ and $d3$-sites significantly alters the shape and slightly shifts the position of the $d2$-resonance lines.

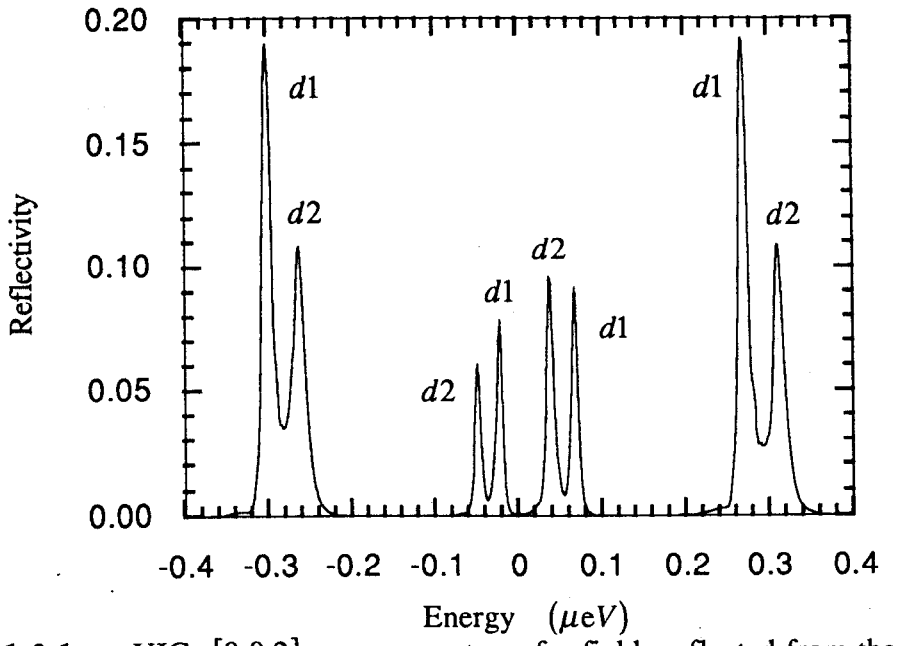

Fig. 11-2.1. YIG [0 0 2] energy spectrum for fields reflected from the $d1$ and $d2$-sites. The incident angle is $+20\mu rad$ from the Bragg peak. The incident field is $\hat{\boldsymbol{\sigma}}$ polarized and the internal magnetic field is parallel to the scattering plane and crystal surface (that is, nearly in the photon direction). The $d2$-lines suffer a diminution in amplitude because of additional absorption from the nonreflecting $d3$-site that has resonance lines coincident with the $d2$-lines.

The $d2$-$d3$ interaction is not the only effect that can cause frequency shifts. Nuclear level mixing resulting from two competing quantization axes (the magnetic field and electric field gradient directions) changes the scattering amplitudes of each hyperfine line. Since the resonance frequency shifts are proportional to the scattering amplitude, they will vary depending upon the amount of nuclear level mixing. When the electric field gradient axis is parallel to the internal magnetic field direction, there is no nuclear level

mixing since there is only one clearly defined quantization axis. When the two axes are perpendicular, the amount of nuclear level mixing maximizes. However, since the electric quadrupole interaction is small compared to the magnetic dipole interaction, this effect is small. Fig. 11-2.2 shows that shifts of up to 1.5 neV (or 0.3Γ) can occur when nuclear level mixing is included (for the case in which the internal magnetic field is parallel to the $d1$-electric field gradient and perpendicular to the $d2$-electric field gradient).

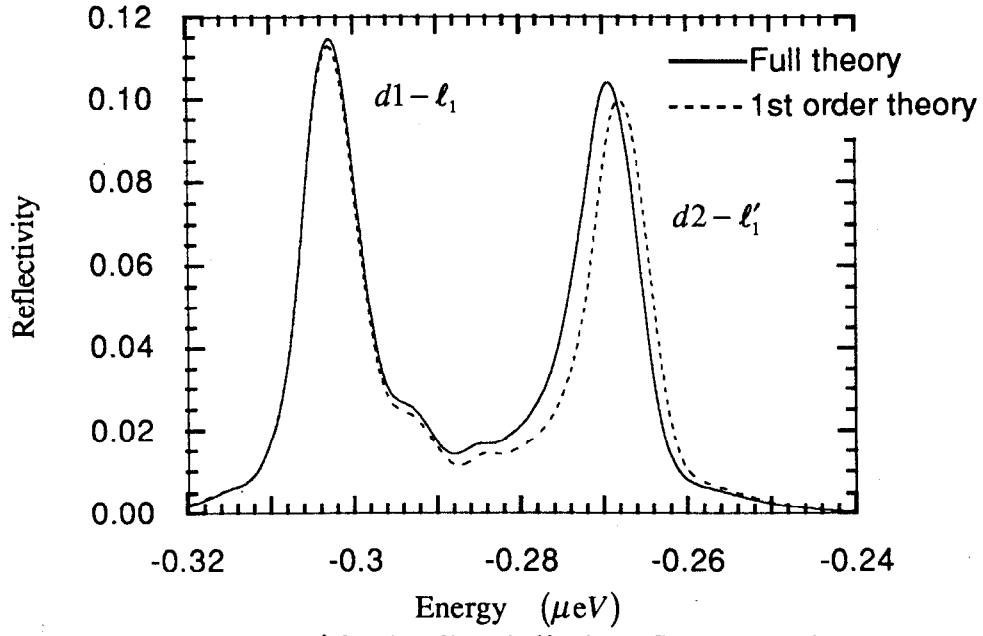

Fig. 11-2.2. Lines ℓ_1 and ℓ_1' for the $d1$ and $d2$-sites. Same scattering geometry as that used in Fig. 11-2.1 except that the incident angle is $+40\mu rad$ from the Bragg peak. The solid curve is calculated using the full dynamical diffraction theory including nuclear level mixing while the dotted curve excludes nuclear level mixing. Nuclear level mixing causes a shift in the $d2$-line of 1.5 neV (or 0.3Γ).

All the additional effects that cause apparent shifts in the resonant frequency increases the difficulty of conclusively stating anything about the dynamical resonance frequency shifts discussed in Chapter 7. And the multiplicity of hyperfine lines for complicated systems such as YIG can make life even harder. For instance, one would be hard pressed to say anything about dynamical resonance frequency shifts for the quantum beat data exhibited in Fig. 11-1.1 (the magnetic field, in this case, is perpendicular to the scattering plane). The asymmetry in the beat patterns for reflections on both sides of the Bragg peak is due to resonance frequency shifts and a host of other dynamical factors in a way that is not clearly apparent. This is because all of the hyperfine lines beat with each

other with the beating between the strongest lines, lines 1 and 6, dominating the pattern. Since lines 1 and 6 have the same scattering amplitude, these lines are frequency shifted by the same amount. Thus, to first order, the beat pattern will look the same between two angular positions symmetric about the Bragg diffraction peak even though the resonance frequency shift is antisymmetric about the Bragg diffraction peak (see Fig. 7-2.7). The differences in the beat patterns comes about because of the beating between lines 1 and 6 with the weaker lines 3 and 4, and due to the dynamical effects described earlier in this section.

Going to the scattering geometry where the magnetic field is parallel to the scattering plane simplifies matters. For this geometry the pair of line 1&4 and 3&6 beat with each other (see Fig. 8-1.4), and, most importantly, each pair of lines beats with the same amplitude. If lines 1 and 6 are frequency shifted by δ and lines 3 and 4 are frequency shifted by Δ, then the two possible beat frequencies are shifted by the difference between these individual frequency shifts:

$$(\omega_4 + \Delta) - (\omega_1 + \delta) = (\omega_4 - \omega_1) - (\delta - \Delta) = \Delta\omega_{14} - f$$

$$(\omega_6 + \delta) - (\omega_3 + \Delta) = (\omega_6 - \omega_3) + (\delta - \Delta) = \Delta\omega_{36} + f$$

where $\Delta\omega$ is the beat frequency shifted by $f = (\delta - \Delta)$. Going from one side of the Bragg peak to the other side causes f to change sign, and each beat frequency shifts in the opposite direction. For large enough f this results in clearly visible effects that can dominate other effects caused by all other possible sources of frequency shifts.

An illustration of how resonance frequency shifts modify quantum beat patterns is given in Figs. 11-2.3 and 11-2.4. They were calculated at symmetric positions about the Bragg peak for a horizontally polarized field incident at 40μrad from the Bragg peak. Since the incident and scattered field directions are nearly parallel to the magnetic field, the scattered fields can be approximated as both left $(\hat{\mathbf{e}}_+)$ and right $(\hat{\mathbf{e}}_-)$ circularly polarized for the pair of lines 1&4 and 3&6 respectively. The $\hat{\mathbf{e}}_+$ fields interfere producing the shifted beat frequency $\Delta\omega_{14} - f$, and the $\hat{\mathbf{e}}_-$ fields interfere producing the shifted beat frequency $\Delta\omega_{36} + f$. The quantum beat patterns of each polarized field is shown in (a) of Figs. 11-2.3 and 11-2.4. The sum of these beat patterns is shown in (b) of each figure. Because f changes sign on opposite sides of the Bragg peak, the total field intensity differs on symmetrical sides of the Bragg peak. These patterns were calculated only for reflections from the $d1$ and $d2$ sites. The effect of adding absorption from the $d3$ is shown in (c) of each figure--small additional frequency shifts results.

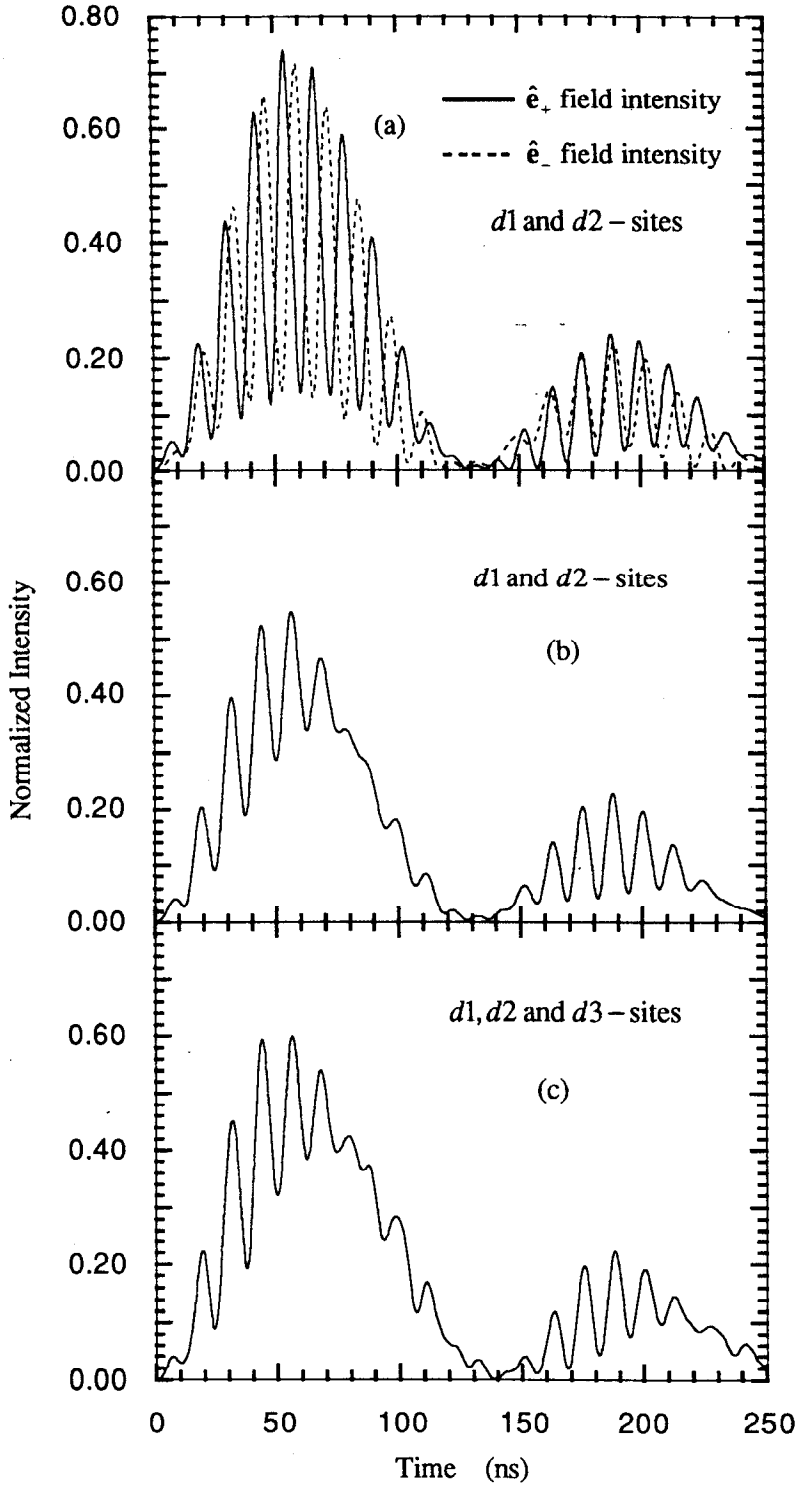

Fig. 11-2.3. YIG [0 0 2] beat patterns for a $\hat{\sigma}$ field incident $-40\mu rad$ from the Bragg peak. $\mathbf{B}_{int}$ is parallel to scattering plane and crystal surface (nominally in the incident and scattered photon directions). The $\hat{e}_+$ and $\hat{e}_-$ field intensities in (a) are summed to produce the net field intensity in (b) when only scattering from the $d1$ and $d2$-sites. The effect of including the $d3$-site is shown in (c).

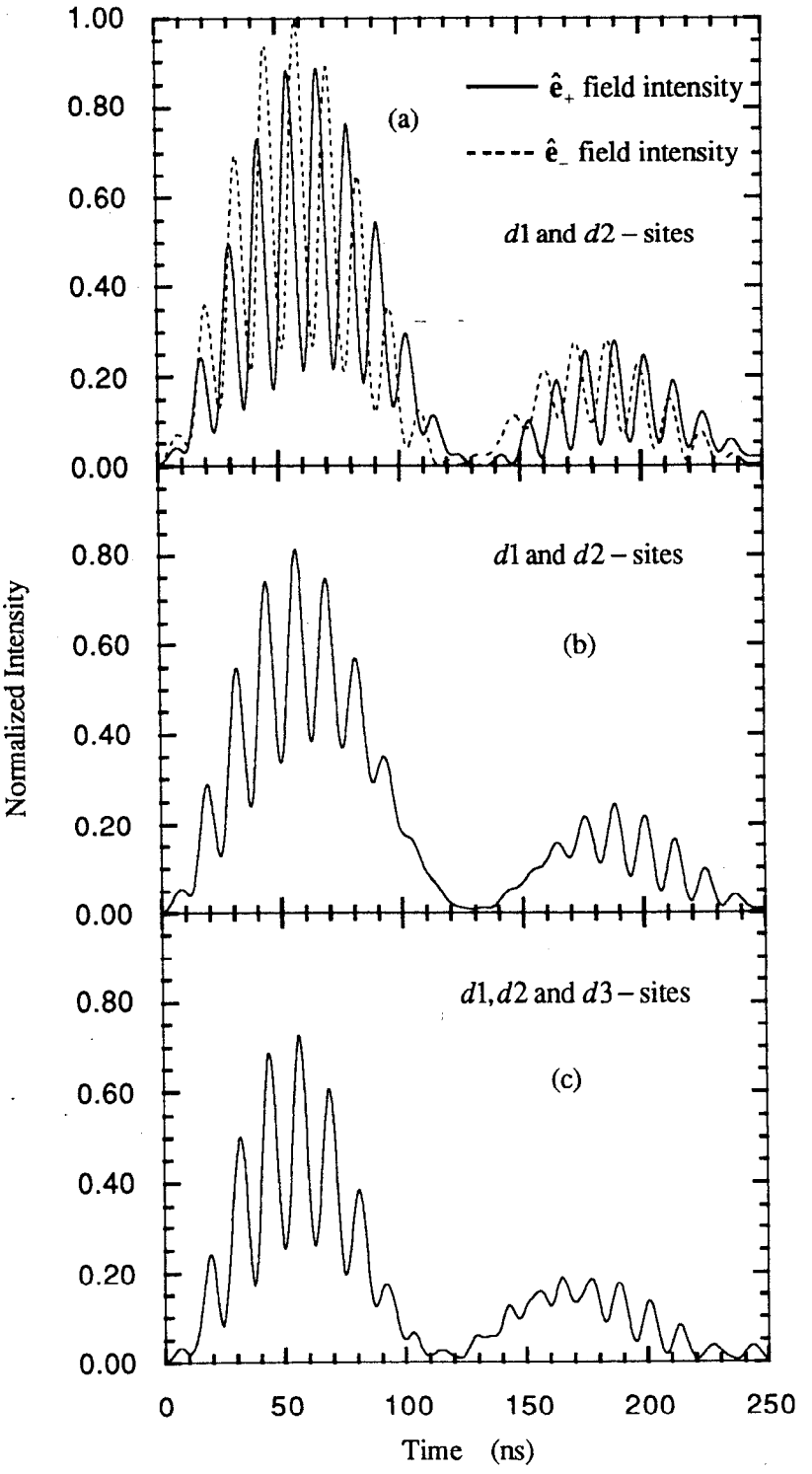

Fig. 11-2.4. Same as Fig. 11-2.3 except that the $\hat{\sigma}$ polarized field is incident $+40\mu rad$ from the Bragg peak.

To get a handle on understanding the resonant frequency shifts, a simple semi-kinematical theory based on average beat frequencies and frequency shifts can be applied. This is justified because the 4 magnetic beat periods are all nearly equivalent (the same goes for the 2 electric quadrupole beats) as illustrated in Table 10-1.2. The net intensity of the diffracted fields can be approximated as

$$I(t) = I_0 e^{-(s+\Gamma)t/\hbar}\left\{\sin^2\left[\frac{(\Delta\omega_{14}-f)t}{2}\right]+\sin^2\left[\frac{(\Delta\omega_{36}+f)t}{2}\right]\right\}\sin^2\left(\frac{\Delta\omega_{EQ}t}{2}\right) \quad (11\text{-}2.1)$$

where $\Delta\omega_{14}$, $\Delta\omega_{36}$, and $\Delta\omega_{EQ}$ are average magnetic and electric quadrupole beat frequencies, s is the average speedup discussed in Section 11.1, and f is an average beat frequency shift.

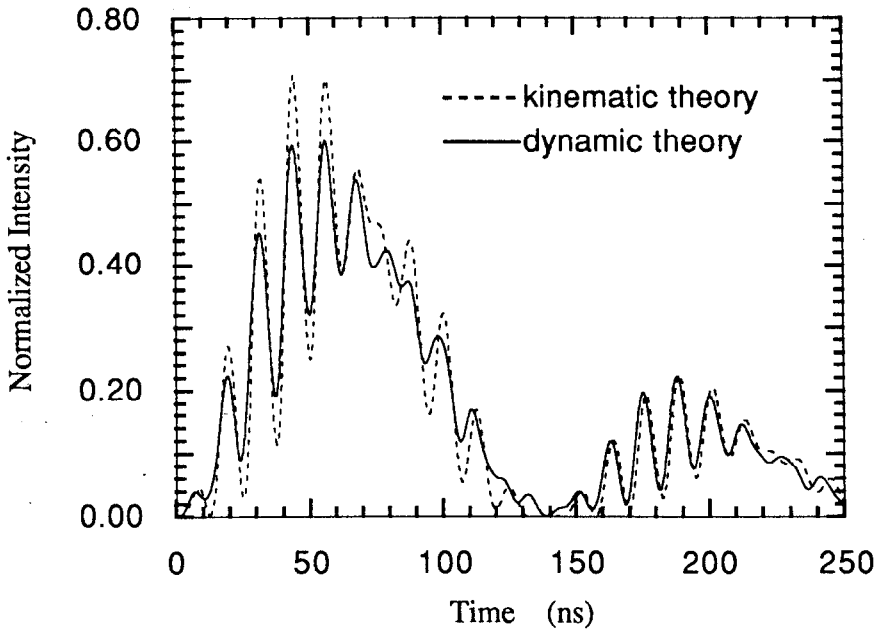

Fig. 11-2.5. As a demonstration, the semi-kinematical formula, Eq. 11-2.3, was fit to the dynamical diffraction calculation (shown in Fig. 11-2.3 (c)). The best kinematic fit gave an average beat frequency shift of $f = 3.4 \pm .5\,\text{neV}$, or $0.7 \pm 0.1\Gamma$.

This formula was fitted to the quantum beat pattern shown in Fig. 11-2.3 (c). The average magnetic beat periods used were $\Delta T_{14} = 12.2\,\text{nsec}$ and $\Delta T_{36} = 13.0\,\text{nsec}$. The values s, $\Delta\omega_{EQ}$, and f were allowed to vary to get the best χ^2 fit. The results of the fit, shown in Fig. 11-2.5, gave $s = 0.3 \pm 0.1\Gamma$, $\Delta T_{EQ} = 138 \pm 2\,\text{nsec}$, and $f = 3.4 \pm .5\,\text{neV}$, or $0.7 \pm 0.1\Gamma$ where Γ is the natural linewidth $\left(\Gamma = 4.67 \times 10^{-9}\ \text{eV}\right)$. What this fit

demonstrates is how closely semi-kinematical diffraction theory parallels dynamical diffraction theory when a few dynamical quantities are inserted into kinematical expressions. When using Eqs. 7-6.30 and 7-7.1, the collective dynamical frequency shift 40μrad below the Bragg peak (taking the difference in ω_s between lines 1&4 or 3&6) is 1.1neV (0.23Γ) which is the same order of magnitude as the average beat frequency shift. The discrepancy between the two values shows that there are other frequency shifts that must be taken into account.

For $f = 3.4$neV (at $\delta\theta = -40\mu$rad), the beat period between lines 1 and 4 decreases by 0.1 nsec and the beat period between lines 3 and 6 increases by 0.1 nsec--the beat periods then diverge by an extra 0.2 nsec forcing the beat pattern of the $\hat{\mathbf{e}}_+$ fields to be more out of phase with the pattern of the $\hat{\mathbf{e}}_-$ fields. This causes the beat pattern to become washed out as shown by the diminished peak to valley contrast in Fig. 11-2.3 (b). Symmetrically on the other side of the Bragg peak (at $\delta\theta = +40\mu$rad), the beat period between the two circularly polarized fields should converge by 0.2 nsec making the beat patterns more in phase and increasing the peak to valley contrast as shown in Fig. 11-2.4 (b). The effect of the $d3$-site causes additional frequency shifts that are not symmetrical on both sides of the Bragg peak--they appear to cause more drastic effects on the positive side of the Bragg peak (as shown in (c) in Figs. 11-2.3 and 11-2.4).

The striking changes in the quantum beat patterns as a function of the deviation angle from the Bragg peak are presented in Fig. 11-2.6. Full nuclear dynamical diffraction theory was used to obtain the fits (Eq. 11-2.1 was not used). As can be clearly noticed, in going from the low angle side of the Bragg peak to the high angle side, the $\hat{\mathbf{e}}_+$ and $\hat{\mathbf{e}}_-$ time beat patterns progress from nearly out of phase to nearly in phase. In other words, the contrast improves as the deviation from Bragg increases over the angular range given in the figure.

The data in Fig. 11-2.6 was also fit using the simple semi-kinematical formula described by Eq. 11-2.1. The average beat frequency shift as a function of angle is shown in Fig. 11-2.7. On the low side of the Bragg peak, the parameters $\Delta\omega_{14}$ and $\Delta\omega_{36}$ were fixed (their periods were set at $\Delta T_{14} = 12.2$nsec and $\Delta T_{36} = 13.0$nsec). However, on the high angle side of the Bragg peak, because of the drastic effects by the $d3$-site which played havoc with the fits, these parameters were varied. An attempt was made to fit the data with a Lorentzian dispersion curve noting that, since the angular divergence in the data was 20μrad, semi-kinematic fits near the Bragg peak become difficult to interpret since both positive and negative frequency shifts can exist simultaneously. The fit shows that, like the dynamical resonance frequency shift, the average beat frequency shift follows a

dispersive relationship. The data also reveals that it is possible to easily measure average frequency shifts smaller than a linewidth.

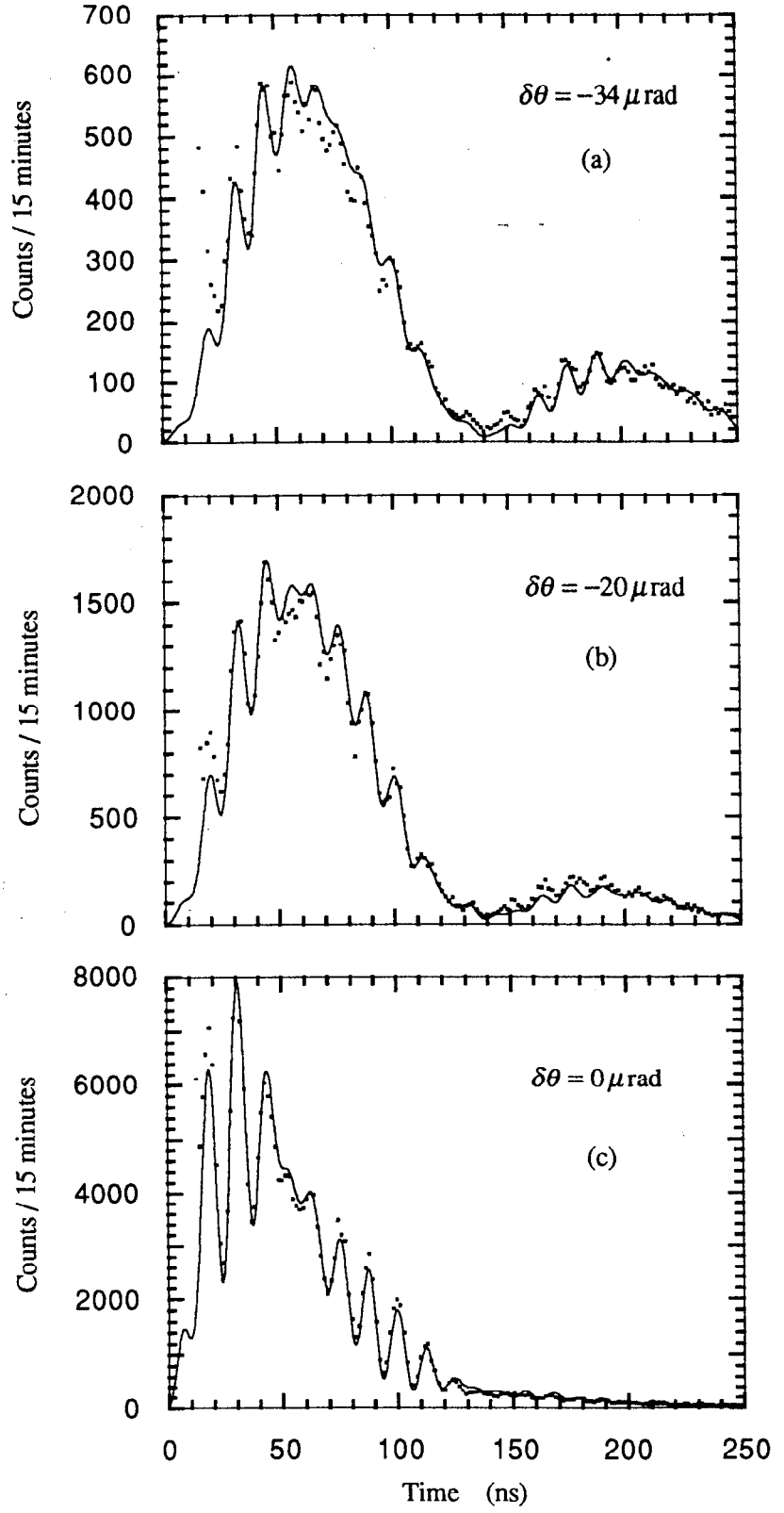

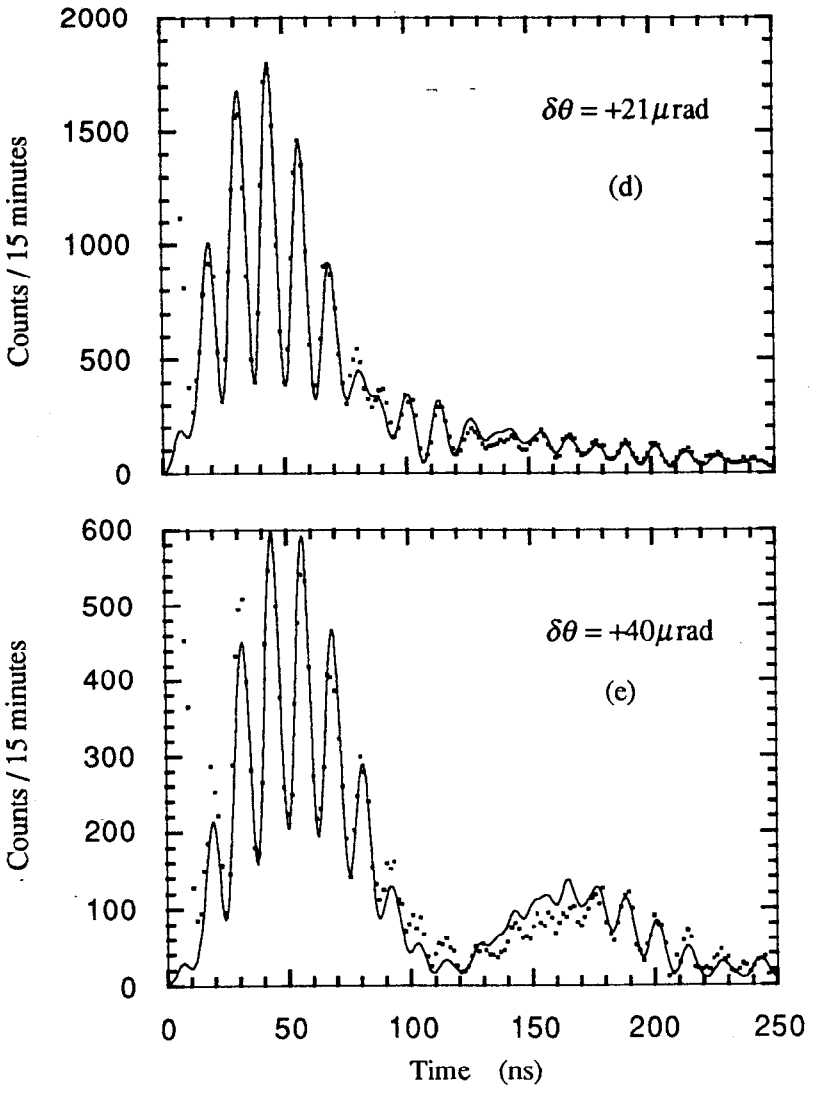

Fig. 11-2.6. Nuclear hyperfine quantum beat patterns as a function of the deviation from the Bragg peak. Measurements for (a), (b), and (c) were taken on the low angle side of the Bragg peak at -34, -20, and 0 μrad respectively. Measurements for (d) and (e) were taken on the high angle side of the Bragg peak at 21 and 40 μrad. Note that the contrast improves when going from the low angle side to the high angle side of the Bragg peak.

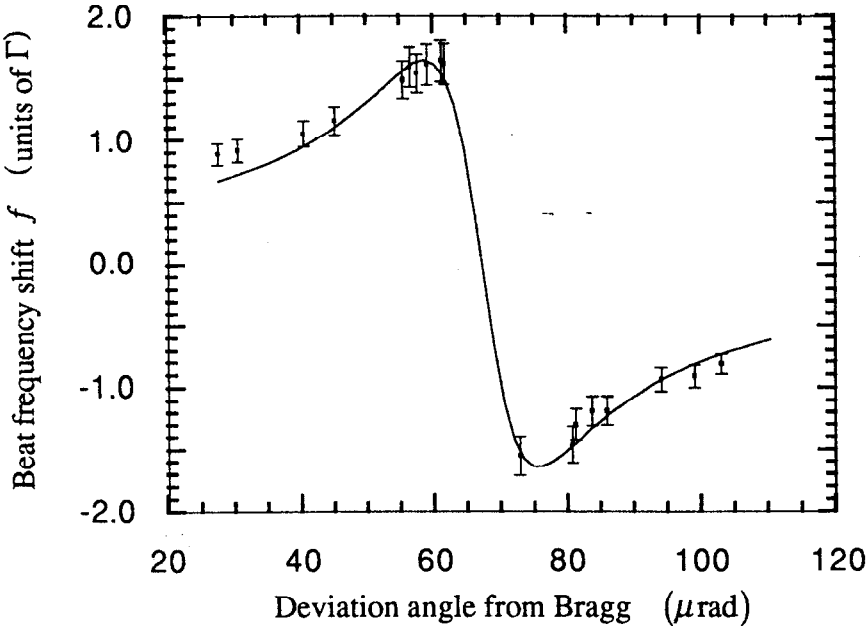

Fig. 11-2.7. The average beat frequency shift versus the deviation angle from Bragg appears to follow a Lorentzian dispersive curve. Average beat frequency shifts of up to $1\frac{1}{2}$ linewidths occurred near the Bragg peak. The dispersion curve is centered at $67 \pm 5\,\mu$rad and has a $17 \pm 7\,\mu$rad linewidth.

11.3 The Lamb-Mössbauer Factor

The change in the quantum beat patterns as a function of the deviation angle from Bragg provides a unique opportunity to measure the Lamb-Mössbauer factor. This opportunity comes about because the angular independent part of the structure factor, Eq. 7-2.10, is directly proportional to the Lamb-Mössbauer factor, $L_M(\mathbf{k}_i)L_M(\mathbf{k}_f)$, and three well known experimentally measured quantities: $\Gamma(L,\lambda)$ is the radiative decay rate $\Gamma_{rad} = \Gamma/(1+\alpha)$ where $\hbar/\Gamma = 140.95\,$nsec and $\alpha = 8.23$ for ^{57}Fe, and C is the isotopic concentration which has been accurately measured to be 0.8097 for the YIG crystal samples. Since changes in the quantum beat patterns are directly correlated with the strength of the scattering amplitude, information can be extracted from these changes to determine the Lamb-Mössbauer factor.

Fitting the data in Fig. 11-2.6 by allowing the Lamb-Mössbauer factor to vary produces new fits that are precisely the same as the old fits except that the value of $\delta\theta$ giving the best fit is different. This results because increases in the Lamb-Mössbauer factor only serves to increase the nuclear Darwin width (see Fig. 11-3.1). If the Lamb-Mössbauer factor is increased to a new value, the new beat pattern can be made identical to the old pattern by simply going to a point further from the Bragg peak (a horizontal line drawn in Fig. 11-3.1 intercepts the curves having a larger Lamb-Mössbauer factor further out from the peak). Thus, by precisely measuring the difference in angle between two reflections, the Lamb-Mössbauer factor that most closely results in describing these differences can be found.

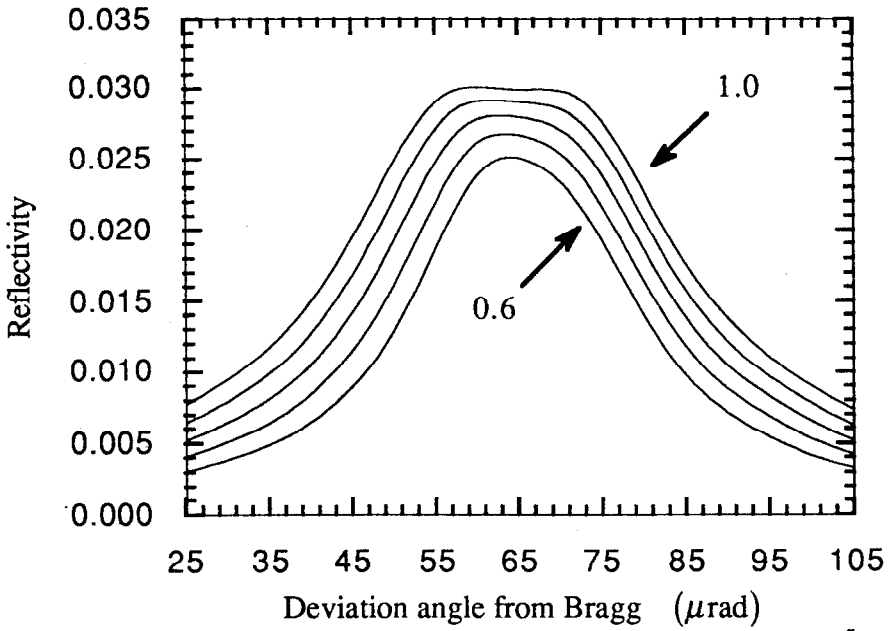

Fig. 11-3.1. Darwin curves for a 2.6μm thick YIG crystal for the [0 0 2] reflection and for a magnetic field parallel to the scattering plane. The Lamb-Mössbauer factor for the top curve was set at unity, and the lower curves illustrate what happens when this factor is decreased to 0.6 in steps of 0.1--the peak intensity decreases and the Darwin width narrows. The Bragg peak is centered at 65μrad, and the Darwin width is 41μrad for a Lamb-Mössbauer factor of 0.82 (this is the value used in all the previous fits in this and the preceding chapter).

Two experimental runs were made in which the YIG crystal was rotated in steps of 1 millidegree (17.4μrad). The crystal was centered on a Huber 4-circle diffractometer having a θ-circle consisting of a Huber 430 goniometer connected with a 20:1 gear reducer. As a result, the θ-circle was able to make step sizes of $\frac{1}{4}$ millidegrees.

Unfortunately, because these measurements were made without the intention of measuring the Lamb-Mössbauer factor (the possibility of doing this was discovered only after the measurements), the experiment was not carefully tailored for this application. Any backlash problems in the θ-circle would show up as large $4.4\,\mu$rad discrepancies because of the large stepping size. For each run 4 measurements were taken at one and two millidegrees above and below the Bragg peak, and one measurement was taken at the Bragg peak. Before each off-Bragg measurement was made, a rocking curve measurement was performed to re-determine the position of the Bragg peak. This additional check was done because the synchrotron beam direction stability and the backlash problems of the Huber goniometers caused real or apparent shifts in the position of the Bragg peak.

The results are shown in Fig. 11-3.2. Plotted is the standard deviation, σ_N, between the actual and measured angle (obtained by the best fit to the data) versus the Lamb-Mössbauer factor

$$\sigma_N = \sqrt{\left(\Delta\theta_{act} - \Delta\theta_{meas}\right)^2 / N}\,. \tag{11-3.1}$$

The quantity $\Delta\theta_{act}$ is either ± 1 or ± 2 millidegrees, and $\Delta\theta_{meas}$ is the difference in angle between the angle measured at the Bragg peak and the angle measured off-Bragg. The minimum standard deviation for two sets of runs lie at different Lamb-Mössbauer factors--a parabolic fit to the data yielded Lamb-Mössbauer factors of 0.78 and 0.86 at the minima. Thus, the Lamb-Mössbauer factor could be determined to only with 5%:

$$L_M(\mathbf{k}_i)L_M(\mathbf{k}_f) = 0.82 \pm 0.04.$$

On the agenda were improvements to the experimental apparatus in order to perform more sensitive measurements about the YIG Bragg peak. A Si [10 6 4] channel cut monochromator having a Darwin width of $2\,\mu$rad was built and attached to an Ishikawa sine-bar rotation stage capable of making $0.05\,\mu$rad steps. This system would have greatly improved the angle measurements, but, unfortunately due to lack of time, this system was never used (the Si [10 6 4] reflection reduces the nuclear counting rate by a factor of 10 forcing one to count 10 times longer to get the same statistics as before).

Also, of major interest would be to perform these measurements at other reflections than the YIG [0 0 2] reflection. Little is known about how the Lamb-Mössbauer factor varies with the order of reflection (or the scattering angle).

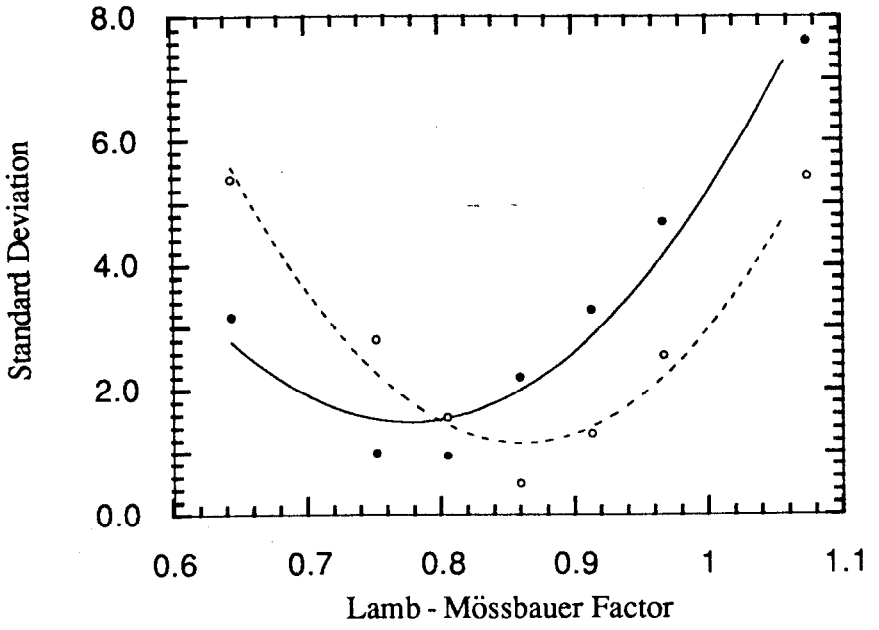

Fig. 11-3.2. Two trial runs to determine the Lamb-Mössbauer factor for the YIG [0 0 2] reflection. The minimum standard deviation gives an average Lamb-Mössbauer factor between the two trial runs of 0.82 ± 0.04.

11.4 Crystal Thickness Effects

The time evolution of radiation scattered by a collection of resonant particles can be significantly influenced by the total number of resonant scatterers. This property provides the opportunity to infer the thickness of a medium of scatterers directly from the time distribution of the scattered radiation.

The fields reflected from a thin crystal have characteristics that are similar to the fields transmitted through a thin isotropic slab (that is, a thin absorber) except that there are small resonance frequency shifts and small increases in the decay rate (see Section 7-6). For a thick crystal, because many more scatterers contribute to the scattered fields, there can be substantial frequency shifts and increases in the decay rate (as seen in Sections 11-1 and 11-2). Simply due to speedup effects, as the thickness of a crystal increases, the time distribution of the scattered radiation is squeezed into earlier times.

Care must be taken when trying to determine the thickness of crystals when Bragg scattering is used. This is because primary extinction can severely limit the depth that fields

can penetrate into the crystal. If the crystal is thicker that the extinction length for a particular order of reflection, then information about the crystal thickness cannot be extracted because changes in the time distribution saturate at the extinction length.

A YIG thickness greater than 1μm cannot be measured using the [0 0 2] reflection because the penetration depth for 14.413 keV radiation is about 1.1μm. However, the penetration depth for the [0 0 10] reflection is roughly six times greater giving the possibility of measuring crystal thicknesses up to 6.4μm.

Calculations of YIG [0 0 10] quantum beat patterns for various crystal thickness are shown in Fig. 11-4.1. The area of each curve is normalized to the area of the data presented in (a) in Figs. 10-3.1 and 10-4.1 for the case in which the internal magnetic field is parallel and perpendicular to the scattering plane (the intensity variation with thickness was normalized away because this information is absent in the data). From the figures, one can see that the second peak (past 150 nsec) of the electric quadrupole beat is much more prominent for thin crystals than for thick crystals. For the thicker crystals, the beat pattern is squeezed towards earlier time giving prominent peaks below 50 nsec.

Using the result that the quantum beat patterns were sensitive to thickness variations produced surprising results. One of the crystals grown by Gualtieri, crystal #57-2, was stated to have a thickness of 6.7 μm.[4] The YIG [0 0 2] quantum beat patterns were not sensitive to crystals this thick since the penetration depth is only 1.1 μm, thus the calculations showed no discrepancy. However, a significant discrepancy existed for the YIG [0 0 10] quantum beat patterns. The YIG [0 0 10] data (together with lower order YIG [0 0 6] and higher order [0 0 14] data) yielded a thickness for crystal #57-2 of $2.6\pm0.2\mu$m rather than the expected 6.7 μm. This unexpected result precipitated a second set of rocking curve measurements to understand more about the structure of this particular crystal. These precision rocking curve measurements are discussed in Section 9.1, and the results are shown in Fig. 9-1.2. The rocking curve for crystal #57-2 showed that the YIG film had bifurcated into two separate layers having slightly different lattice spacings. The YIG reflections were probing only one of these layers--the one 2.6μm thick.

No attempt was made in further experiments to investigate the second 4.1 μm thick layer of crystal #57-2. Instead, the crystal having the best crystal perfection, crystal #57-6, was used in further experiments. This determination was made using the data in Fig. 9-1.2. The YIG [0 0 10] quantum beat data for crystal #57-6 was consistent for a

crystal having a thickness of $4.3 \pm 0.4\,\mu$m. Within the uncertainty, this value agrees with Gaultieri's measured value of $4.7\,\mu$m.

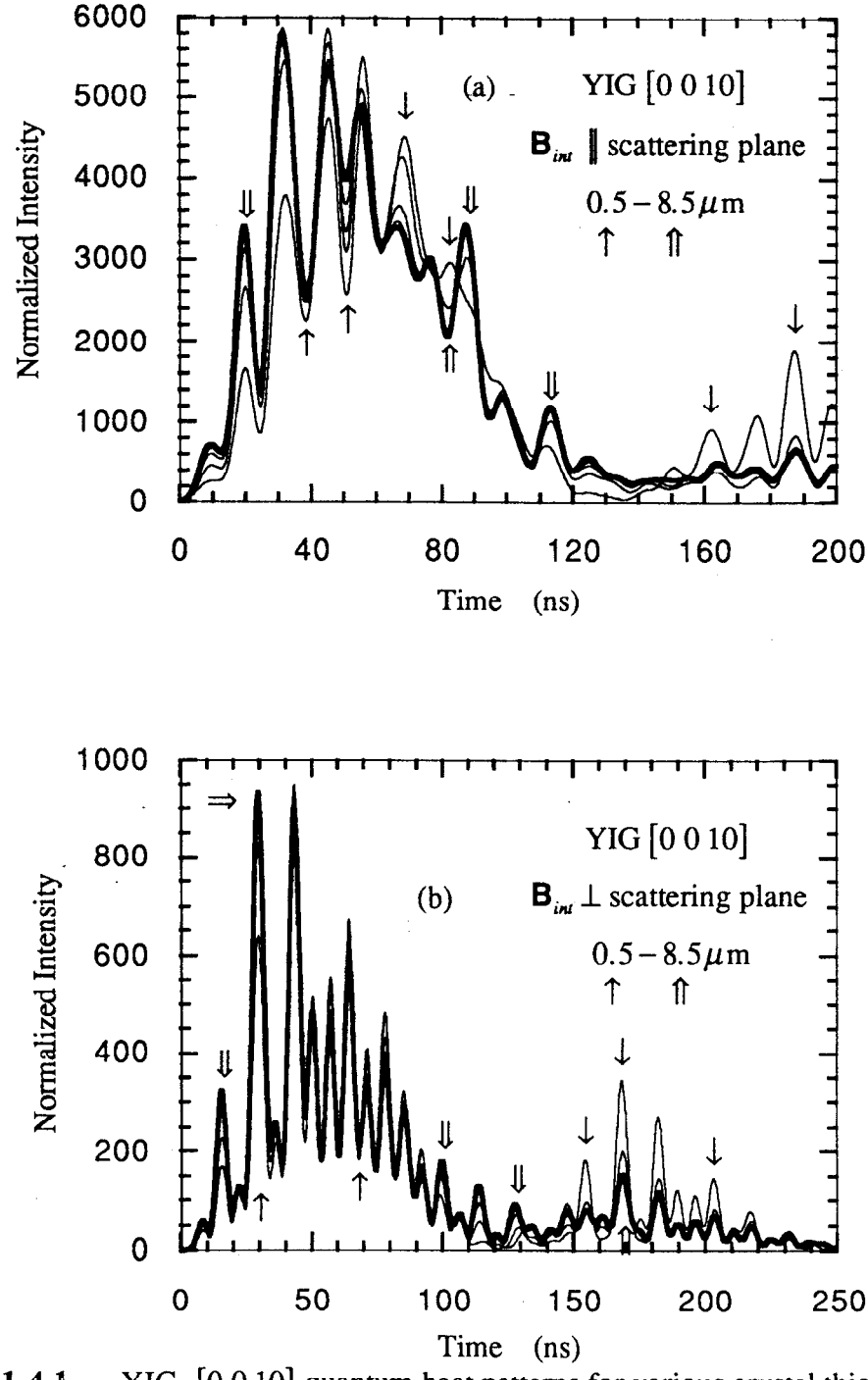

Fig. 11-4.1. YIG [0 0 10] quantum beat patterns for various crystal thicknesses (from 0.5 to 8.5 μm in steps of 2.0 μm). The bold-faced curve represents the 8.5 μm thick crystal and is pointed to by the ⇑ arrow.

11.5 Mössbauer Filter Experiment

Quantum beat patterns can be drastically modified by inserting x-ray optical elements in the beam path. For instance, consider the case when the magnetic field applied across a YIG crystal is parallel to the scattering plane. The net reflected field will then have a four line spectrum (see Fig. 8-1.4) composed of right and left circularly polarized fields. The lines having the same polarization interfere with each other to produce the typical quantum beat pattern having a 12 to 13 nsec beat period. However, this magnetic beating can be completely eliminated by inserting in the beam path a "black" Mössbauer absorber that completely absorbs all resonant photons of the inner lines (lines 3 and 4). With the inner two lines blocked out, the only beating that can occur is the electric quadrupole beating between the two d-site lines.

An experiment was performed to eliminate the magnetic hyperfine beats present in a quantum beat pattern. The experimental setup is described in Section 9.4. The "black" Mössbauer absorbers used in the push-pull arrangement shown in Fig. 9-4.4 were 91.2% enriched ammonium lithium ferrofluoride absorbers having a single line resonance energy spectrum. The push-pull arrangement ensures that both inner lines of YIG are filtered out simultaneously.

Figure 11-5.1 shows the YIG [0 0 2] quantum beat pattern without the "black" absorbers in the beam path. This figure requires some explaining. This experiment was the first time-resolved Mössbauer measurement made by the Stanford nuclear resonance group (in collaboration with Ercan Alp and Gopal Shenoy from Argonne National Labs). In this first successful search for the nuclear resonance signal, many problems were encountered that were unanticipated.

One problem is clearly shown in Fig. 11-5.1 (a) and (b). The nuclear resonance signal sat on top of a large undulating background that was later found out to be due to afterpulses in the phototubes of the detector. They had a large 1 in 10 afterpulse rate with the afterpulses occurring 460 and 540 nsec after a prompt pulse. The experiment was done on the 10-2 beamline at SSRL. This storage ring operated in a timing mode where electron pulses were separated by 195 nsec (unlike CESR and PEP where pulses were separated by 400 nsec and 2 μsec respectively). Thus, the oscillations seen in the background time data were due to afterpulses initiated by prompt pulses occurring well before the prompt pulse giving rise to the nuclear resonance signal. Fortunately, by using background runs, the background could be adequately subtracted from the nuclear resonance time data. The results of such a background subtraction is shown in Fig. 11-5.1 (c).

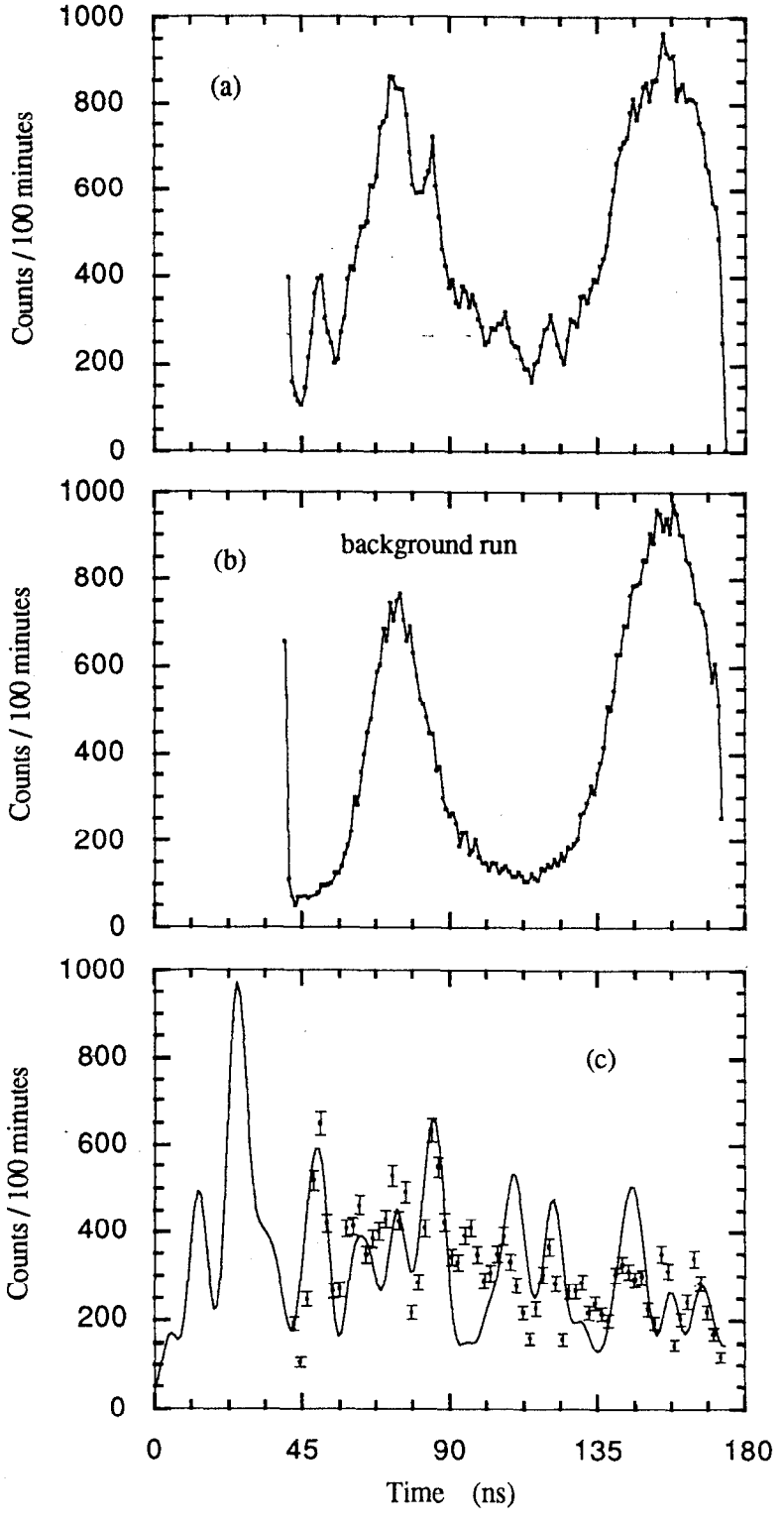

Fig. 11-5.1. Nuclear resonance signal for a scattering geometry that produces significant nuclear level mixing. Total signal plus background is in (a), background due to phototube afterpulses is in (b), and (c) is the result after background subtraction. Nuclear scattering counting rate was about 3.6 counts/sec. (Lines are drawn though data in (a) and (b)).

The other problem resulted from a confusion about the crystallographic directions in the YIG crystal samples. The YIG crystal #57-2 was aligned so that its flat was perpendicular to the incident beam. The flat turned out to be the YIG [1 1 0] direction. For this orientation of the YIG crystal, the internal magnetic field (which was nominally parallel to the incident beam direction) bisects the electric field gradient [1 0 0] and [0 1 0] directions. When the angle between the magnetic field and both electric field gradients is 45°, the electric quadrupole splitting between the $d1$ and $d2$-sites is identical. The lines from each site then lie at the same energy, and, because of the crystallographic 180° phase difference between the two sites, the reflection becomes forbidden for nuclear diffraction. In the experiment, the crystal was set at an azimuthal angle of 44° thus making the reflection nearly forbidden. At this orientation, the nuclear signal is reduced by a factor of 15 over the optimum orientation (that is, for an azimuthal angle of 0°). An extremely painstaking and time consuming effort was undertaken to find the nuclear resonance signal under such low counting rates (≈3.6 counts/sec).

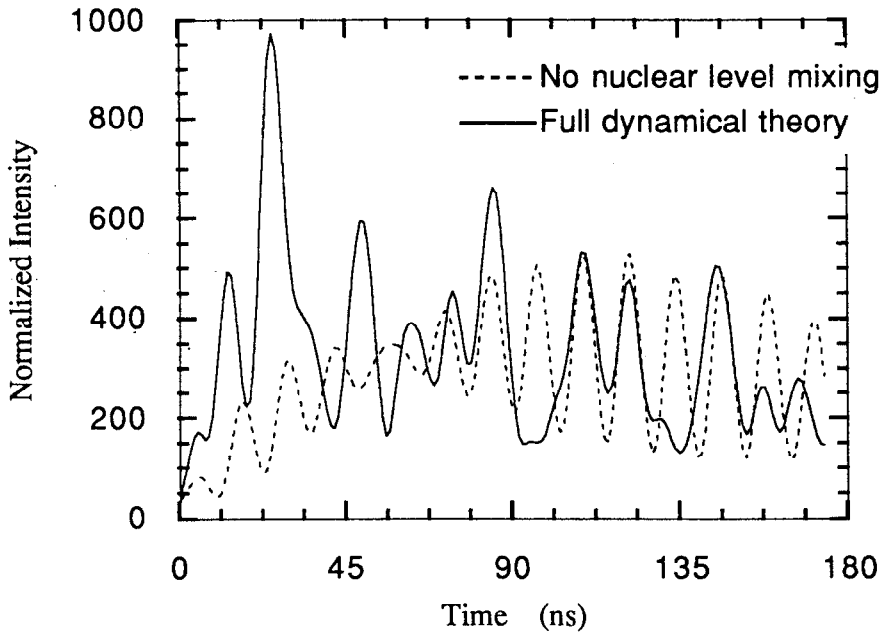

Fig. 11-5.2. Comparison between the full nuclear dynamical diffraction theory and when the theory neglects nuclear level mixing.

Sometimes accidents, as in this situation, can lead to some interesting physics. When the angle between the internal magnetic field and the $d1$ and $d2$-site electric field gradients is at 45°, the nuclear reflection is forbidden only to first order, and second order

effects come into prominence. Nuclear level mixing, which is almost negligible for other angles between the magnetic field and electric field gradients, becomes quite significant at the 45° angle. As described in Section 5.3, the mixing of nuclear states becomes so strong that linear polarization reversal occurs--incident $\hat{\sigma}$ polarized fields are scattered into outgoing π polarized fields. Including nuclear polarization mixing in the nuclear dynamical diffraction theory was necessary to fit the data. Fig. 11-5.2 shows the effect of nuclear level mixing for the fit in Fig. 11-5.1. This phenomena of strongly mixed nuclear states where each resonant line amplitude results from superpositions of all possible nuclear quantum states was later investigated more carefully by the Hamburg nuclear resonance scattering group.[5, 6]

The result of inserting the "black" Mössbauer absorbers in push-pull mode is shown in Fig. 11-5.3. Magnetic hyperfine beats are no longer visible--the "black" absorbers were successful in significantly filtering out the inner resonant lines. What is left is the slow electric quadrupole beat between the two d-sites. The data was fitted with the simple kinematic formula given by Eq. 11-1.1 to illustrate that the time distribution follows an expected slow beat pattern on top of an exponential decay curve. The data exhibited a speedup of $s = 2.9 \pm 0.3$ which is consistent for fields reflected at an angle near the Bragg

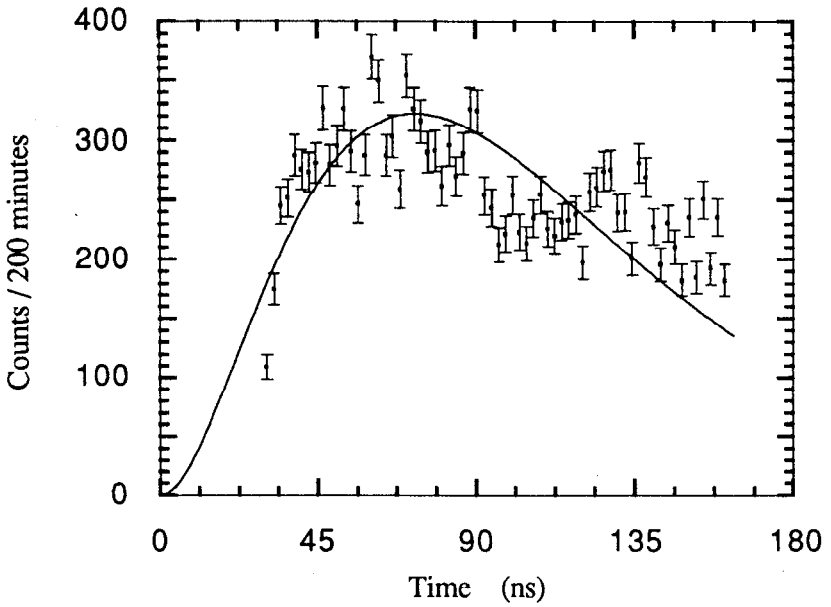

Fig. 11-5.3. Time distribution for an experiment where "black" Mössbauer absorbers filter out hyperfine lines to eliminate magnetic beats. Only the electric quadrupole beat is evident. The counting rate was about 1.3 counts/sec.

peak (the data in Fig. 11-5.1 indicates the reflection was about -5μrad from the Bragg peak). The precise quadrupole beat period was indeterminable due to the lack of good statistics in the data, so the theoretical value of 3.7 μsec was used in the fit.

11.6 General Dynamical Scattering

Nuclear dynamical diffraction theory has been quite successful in explaining all the data obtained by scattering resonant x-rays off ^{57}Fe enriched YIG crystals. The fits have not been perfect, but this problem may be due to crystal imperfection, nonuniformities in the hyperfine fields throughout the crystal, or the inability to accurately characterize the polarization of the field incident upon the crystal. Even certain physical interactions that one would neglect upon first thought because their effects are small can produce noticeable perturbations in the quantum beat patterns. For instance, even though the a-sites have much larger internal magnetic fields that the d-sites, and the a-sites do not reflect any fields for the scattering orders considered in the experiments, these sites can produce small, noticeable effects for incident angles near the Bragg peak. This is shown in Fig. 11-6.1 for

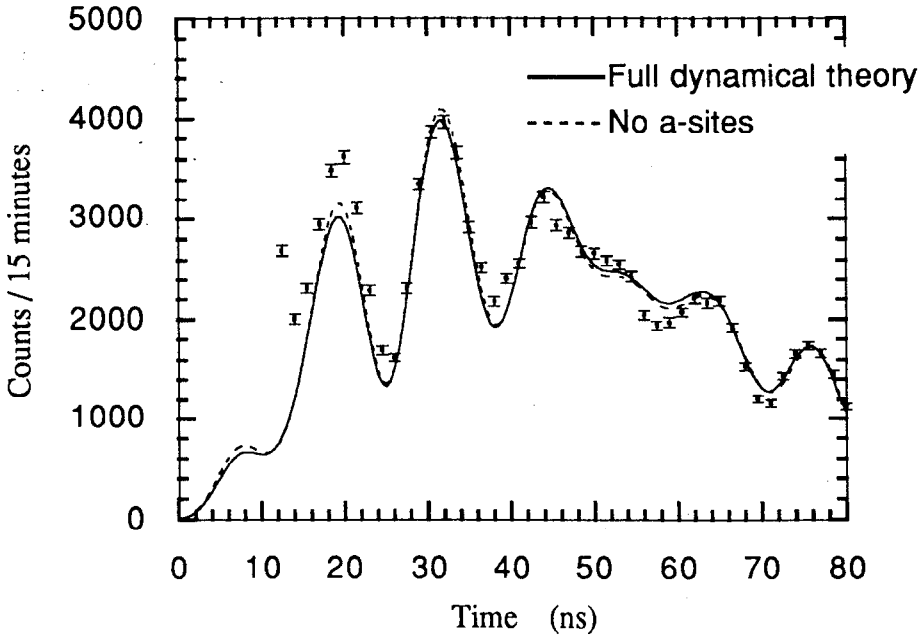

Fig. 11-6.1. Small perturbations upon the time beat patterns due to the presence of ^{57}Fe occupying the a-sites in YIG. The dotted curve shows the effect of eliminating the a-sites. The incident angle is -1μrad from the Bragg peak.

a case in which the internal magnetic field is parallel to the scattering plane. The major effect of the a-sites shows up in the null region where the $\hat{e}_+$ and $\hat{e}_-$ polarized field intensities are out of phase. Yet, theses effects are too small to yield any meaningful information about the a-sites in the data collected.

One interesting problem that was analyzed was whether there was any additional dephasing in the scattering process that would cause the quantum beats to wash out earlier than expected. To see this effect required a long count rate experiment that covered a range of several lifetimes. Two TACs were used to perform this experiment--one measured time spectra from 0 to 250 nsec, and the other measured spectra from 200 to 450 nsec. The TACs could be put in synch by using the overlapping measurement (the TACs were actually found to be in synch making time corrections between TACs unnecessary). The results are shown in Fig. 11-6.2. Clear, unmistakable beats can be seen up to $2\frac{1}{2}$ lifetimes (340 nsec), and beyond that time both data and theory start to become washed out--natural dephasing due to the decay of the nuclear excited state makes it necessary to perform

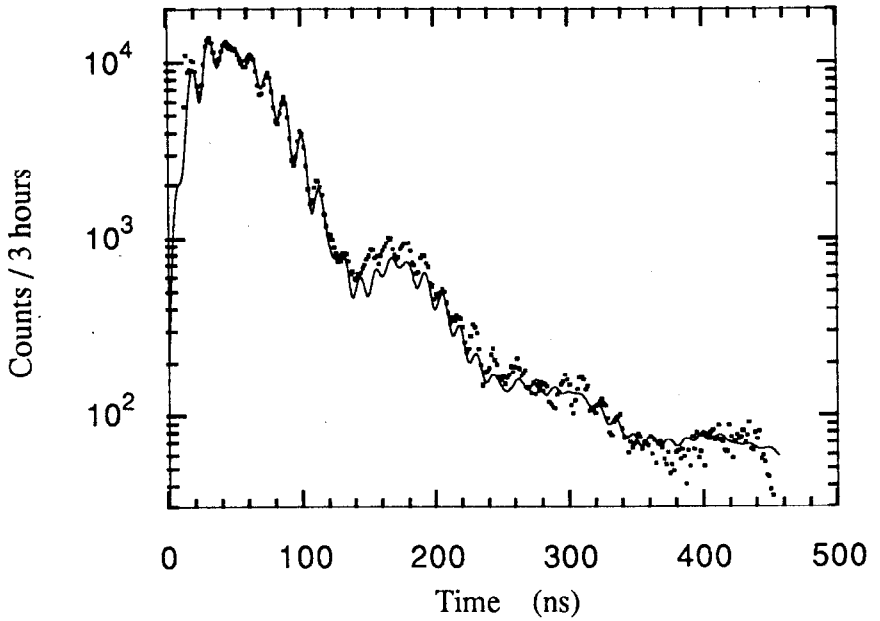

Fig. 11-6.2. Three hour measurement of YIG [0 0 2] time spectrum covering over 3 natural lifetimes. The incident angle is $-9\,\mu$rad from the Bragg peak, the internal magnetic field is parallel to the scattering plane, and a background of 1.5 counts/sec was used in the fit. Data collected over a long time is typically more difficult to fit than data collected over a short time. This is probably because there is more time for settings to change during the experiment (such as the incident beam direction). Ringing can be seen up to $2\frac{1}{2}$ lifetimes revealing that the crystal operates similar to a set of oscillators having a high Q.

measurements lasting longer than 3 hours to find out what is happening beyond $2\frac{1}{2}$ lifetimes.

The only difference between the scattering amplitudes for the YIG [0 0 2n] (where n is odd) reflections is that the angular factors in the polarization matrices change and that the real part of the photoelectric scattering amplitude decreases as the Bragg angle increases (that is, $f_0 \rightarrow 0$ in Eq. 7-2.2 as the scattering angle approaches 90°). The decrease in the real part of the photoelectric scattering amplitude only serves to decrease the index of refraction shift and the Darwin width of the Bragg peak. This makes the peak speedup and frequency shifts occur at a smaller deviation angle from Bragg, and it causes the reflected intensity to decrease. What significantly changes the shape of the beat patterns between the

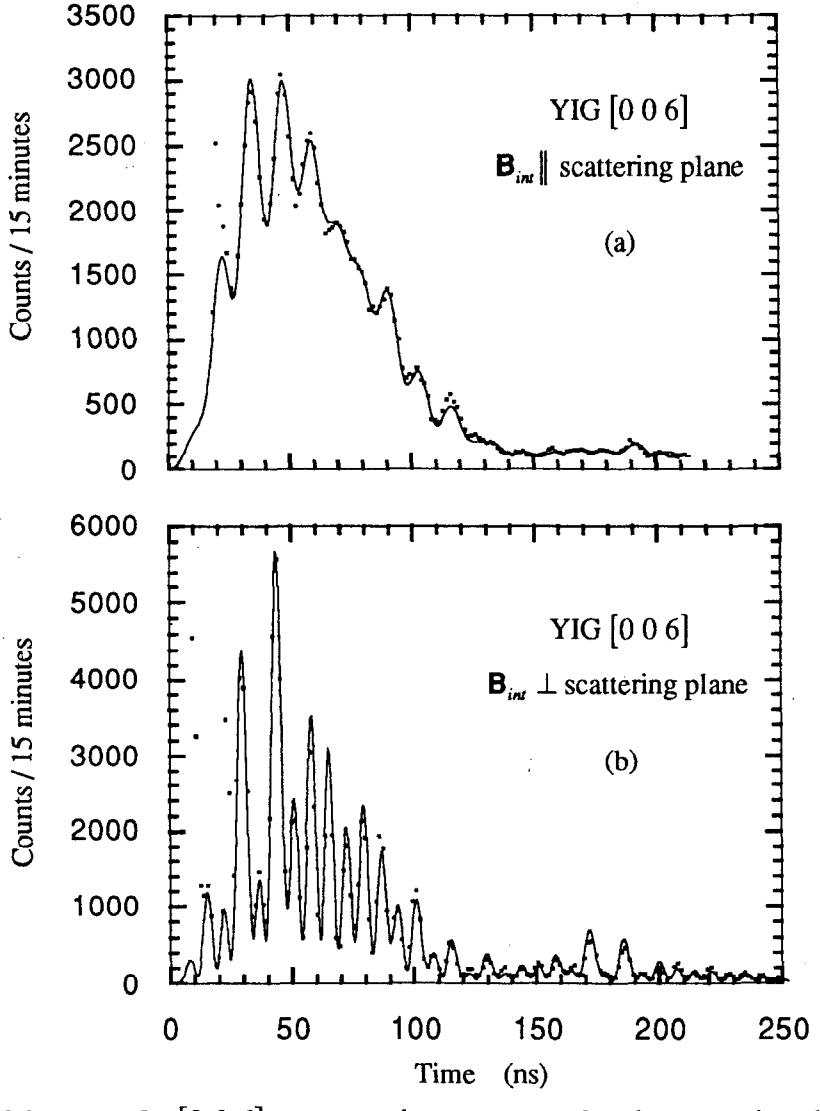

Fig. 11-6.3. YIG [0 0 6] quantum beat patterns for the cases in which the internal magnetic field is (a) parallel and (b) perpendicular to the scattering plane. A horizontally polarized field is incident at an angle (a) -2μrad (b) -1μrad from the Bragg peak.

various YIG reflections are the differences in the polarization matrices (Eqs. 5-1.22 and 5-1.28 for the common scattering geometries used in the experiments).

Time spectra for the YIG [0 0 2] and [0 0 10] reflections have already been shown in Figs. 10-1.3, 10-1.4, 10-3.1, and 10-4.1 for the two cases in which the magnetic field is parallel and perpendicular to the scattering plane (the incoming field was incident at an angle from the Bragg peak of -3μrad for Fig. 10-3.1 (a) and -4μrad for Fig. 10-4.1 (a)). To complete the set, YIG [0 0 6] and [0 0 14] are shown in Figs. 11-6.3 and 11-6.4.

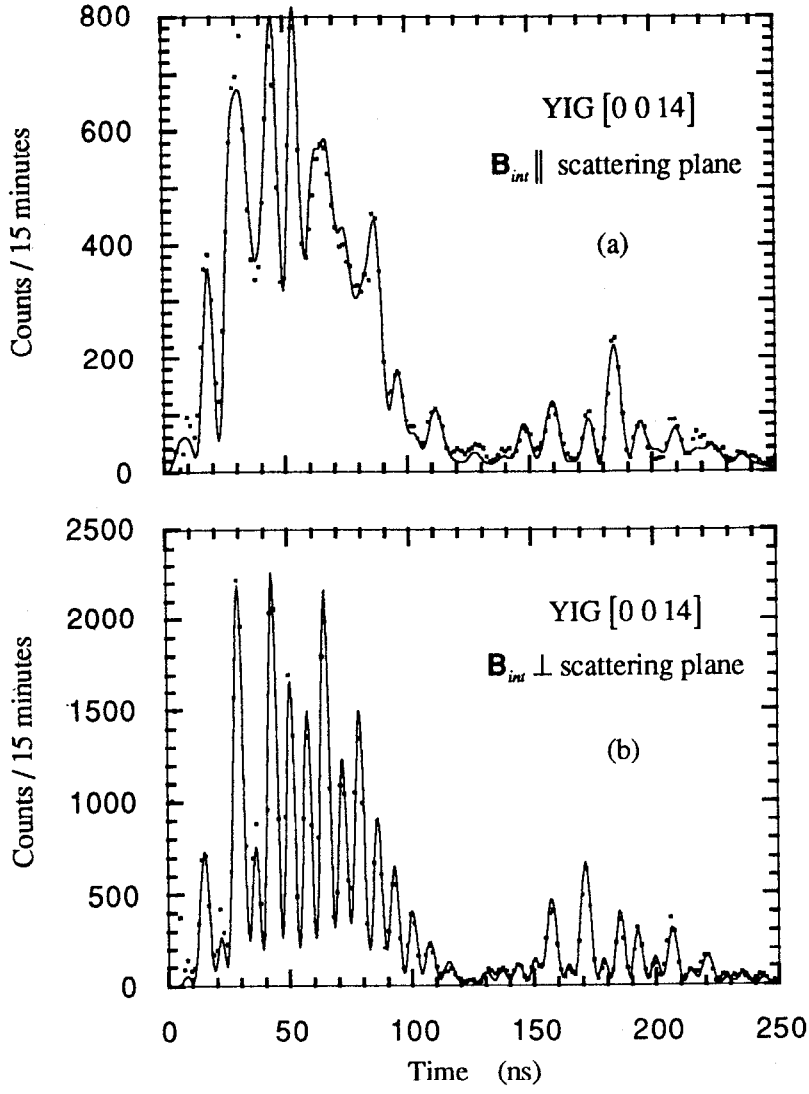

Fig. 11-6.4. YIG [0 0 14] quantum beat patterns for the cases in which the internal magnetic field is (a) parallel and (b) perpendicular to the scattering plane. A horizontally polarized field is incident at an angle (a) -6μrad (b) $+2\mu$rad from the Bragg peak.

Nuclear dynamical diffraction theory should hold equally well for multiple crystal reflections. The only change comes in the boundary conditions in which the incident field on the proceeding crystal is the reflected field from the preceding crystal. Double crystal diffraction experiments were performed by the nuclear resonance scattering group at Hamburg,[7] but only for the case in which both YIG crystals were operated identically. In contrast, double crystal diffraction experiments were performed for various orientations of the internal magnetic field across the two crystals and for various combinations of reflections. Fig. 11-6.5 shows the results of a double reflection from two YIG crystals oriented for the [0 0 2] reflection. In Fig. (a) and (b) both crystals have their internal magnetic fields parallel and perpendicular, respectively, to the scattering plane. In Fig. (c) the first crystal has its internal magnetic field oriented parallel to the scattering plane, while the second crystal has its field oriented perpendicular to the scattering plane. The very noticeable difference between the single and double reflection measurements is an overall shift in the quantum beat patterns. This shift results because the double crystal reflection performs a convolution of two single crystal beat patterns.

Another experiment was performed in which the first crystal was oriented for the [0 0 2] reflection and the second crystal was oriented for the [0 0 4] reflection (the internal magnetic field for both crystals was oriented parallel to the scattering plane). The results are shown in Fig. 11-6.6. The [0 0 4] reflection allows both photoelectric and nuclear diffraction. The double crystal beat pattern should then, to first order, show a YIG [0 0 2] beat pattern since the YIG [0 0 2] diffracted field should reflect promptly from the electrons in the second crystal. To second order, a convolution of single crystal YIG [0 0 2] and YIG [0 0 4] beat patterns should be present.

Double crystal experiments allows one to probe the hyperfine structure of crystals for allowed photoelectric reflections. For instance, observing the quantum beat signal from a YIG [0 0 4] reflection is not possible with the present detector because of the intensity of the allowed photoelectric reflection (unless one uses a narrow bandpass crystal monochromator, but these monochromators also drastically reduce the nuclear signal intensity). The YIG [0 0 2]-[0 0 4] double crystal reflection allows one to get around this problem and to extract information about the photoelectrically allowed [0 0 4] reflection.

Using the first crystal as a monochromator produces extremely monochromatic x-rays to be used in further experiments involving not only crystals but other types of samples. Unfortunately, YIG is a hyperfine split crystal, and its complicated time response must be deconvolved from any experimental results--its time response must, therefore, be

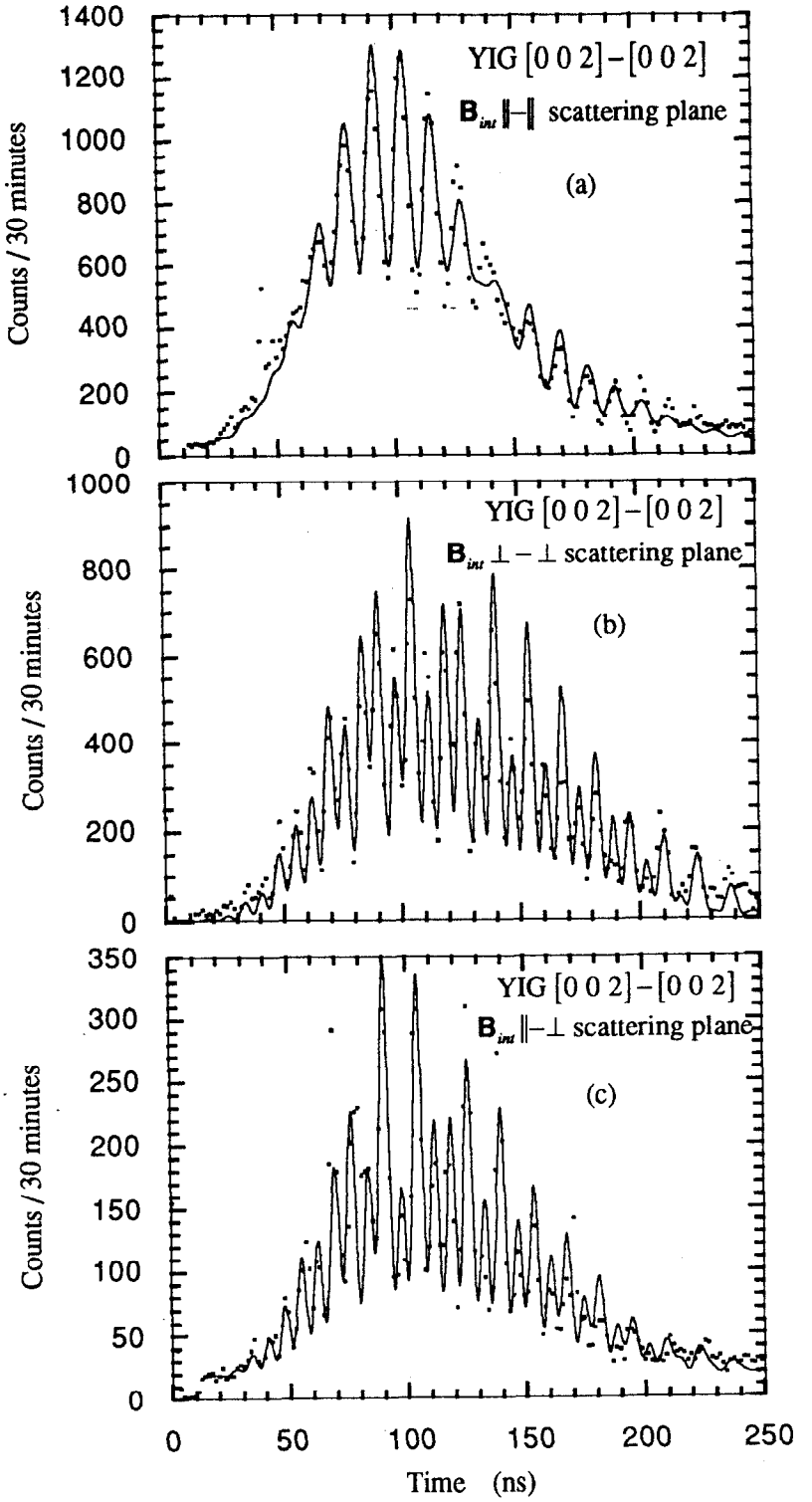

Fig. 11-6.5. Double crystal YIG quantum beat patterns. Both crystals are oriented in the [0 0 2] direction. The internal magnetic field is oriented parallel or perpendicular to the scattering for each crystal separately. In (c), the magnetic field is parallel to the first crystal and perpendicular to the second crystal.

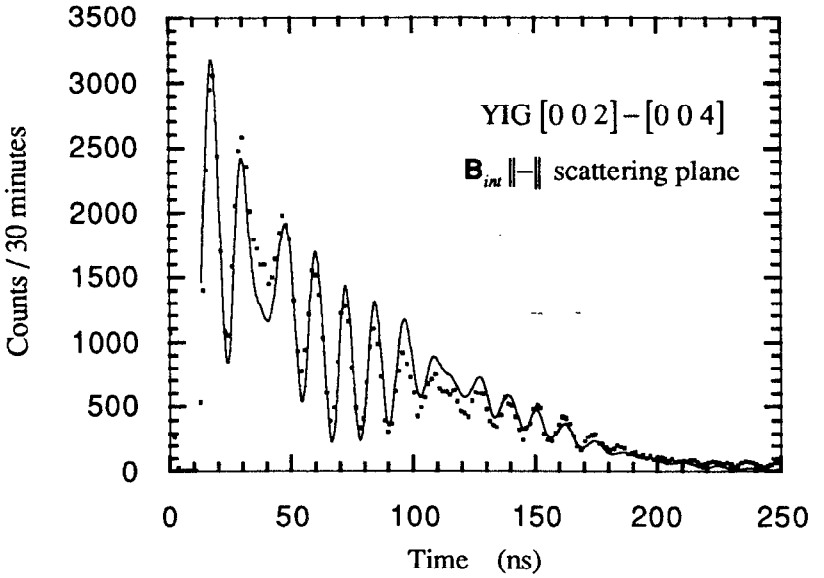

Fig. 11-6.6. Double crystal YIG quantum beat pattern. Both crystals have their internal magnetic fields oriented parallel to the scattering plane, but the first crystal is oriented in the [0 0 2] direction and the second crystal is oriented in the [0 0 4] direction.

well known. However, there is a possibility of constructing single line YIG crystals by impregnating them with certain elements. Even so, the linewidth would not be broad enough to eliminate the necessity of performing deconvolutions to erase the effects of the monochromator when it is used for experiments involving ^{57}Fe enriched samples (even using the properties of the decay rate speedup does not help because speedups, or, in frequency space, an increase in the linewidth, of only as great as 3 have been observed for YIG).

REFERENCES

[1] U. van Bürck, G. V. Smirnov, R. L. Mössbauer, H. J. Maurus, and N. A. Semioschkina, *J. Phys. C: Solid St. Phys.* **13**, 4511 (1980).

[2] A. I. Chumakov, G. V. Smirnov, M. V. Zelepukhin, U. van Bürck, E. Gerdau, R. Rüffer, and H. D. Rüter, *Europhys. Lett.* **17**, 269 (1991).

[3] U. van Bürck, D. P. Siddons, J. B. Hastings, U. Bergmann, and R. Hollatz, *Phys. Rev. B* , (To be published).

[4] D. M. Gualtieri, W. Lavender, and S. L. Ruby, *J. Appl. Phys.* **63**, 3795 (1988).

[5] R. Hollatz, W. Sturhahn, H. D. Rüter, and E. Gerdau, *Influence of Relative Phase Factors between Inequivalent Sites of Single Crystals on Mossbauer*

Experiments, International Conference on the Applications of the Mössbauer Effect (Budapest, Hungary, 1989), vol. 2, p. 14.11.

[6] H. D. Rüter, R. Rüffer, R. Hollatz, W. Sturhahn, and E. Gerdau, *Hyp. Int.* **58**, 2477 (1990).

[7] E. Gerdau, R. Rüffer, R. Hollatz, *Phys. Rev. Lett.* **57**, 1141 (1986).

12. CONCLUSION

The theory of the scattering of x-rays by resonant nuclei is, in principle, much simpler that the theory describing the scattering of x-rays from electrons. This is because electronic dynamical diffraction theory requires relativistic Hartree-Fock calculations to determine the resonant or nonresonant photoelectric scattering amplitude for many electron atoms. Because nuclei can be approximated as point particles, such calculations for nuclear systems are unnecessary. A simple nonrelativistic perturbation theory, treating the nuclei as point particles, can be used to understand the nature of electromagnetic fields scattered from nuclei.

Once the spherical multipole scattering amplitude, whether for nuclear or electronic interactions, has been formulated, the differences between nuclear and electronic scattering theory disappear. The electromagnetic fields scattered from particles can then be expressed in terms of spherical multipole fields. In this thesis, a dynamical scattering theory has been developed where spherical multipole fields interact with a system of particles and undergo multiple scattering. When elastic scattering is assumed, there is no way to determine which photon scattered off which particle since the state of the particle before and after the scattering process is the same. Thus, to describe the scattering interaction, one must coherently sum up all the probability amplitudes of scattering from all of the particles in the system. This sum forms a collective state of many particles--the system of particles acts collectively as an entirely different particle.

Dynamical scattering theory reveals that a collective state has properties similar to a single particle. A single particle interacting with a photon undergoes frequency shifts and has a resonance linewidth due to its interaction with the generated self-fields. Similarly, when the collective state interacts with a photon, it interacts with its generated self-fields which, in this case, are the multiply scattered fields in the medium. These interactions are shown to also lead to resonance frequency shifts and linewidth broadening (or radiative speedup).

The connection between quantum mechanics and classical mechanics was bridged by performing a sum over all of the multiply scattered fields in a medium. What was found was interesting but not surprising. The net electric field multiply scattered from a phased collection of particles was found to be identical to the solution of the Maxwell equations for a medium when the quantum mechanical form of the scattering amplitude is

used in the inhomogeneous wave equation. This semi-classical result confirms that dynamical diffraction theory rests on solid ground.

Nuclear dynamical diffraction effects were strongly evident in the time-resolved Mössbauer spectra measured in synchrotron x-ray diffraction experiments involving ^{57}Fe enriched YIG films. In the time domain, resonant frequency shifts and decay rate speedups were observed, and they were seen to vary as a function of the deviation from the Bragg angle of a YIG crystal. The average decay rate speedup varied in a Lorentzian fashion with the deviation angle, and the peak was centered at the nonresonant Bragg peak. The average resonant frequency shift was seen to vary in a Lorentzian dispersive fashion. Both effects were predicted by nuclear dynamical diffraction theory. A peak speedup of 3Γ and a peak frequency shift of 1.5Γ (where $\Gamma = 4.67\,\text{neV}$ is the natural linewidth) was measured for YIG. The incident beam from a monochromator had an angular divergence of about $20\mu\text{rad}$, and should this divergence be reduced in future experiments, larger peak speedups and frequency shifts should be obtainable.

By measuring the variations in the quantum beat patterns as a function of the deviation angle from the Bragg peak, the Lamb-Mössbauer factor was deduced. A Lamb-Mössbauer factor of 0.82 with a 5% uncertainty was measured for the YIG [0 0 2] reflection. Of interest would be to repeat these measurements for other orders of reflection. How this factor depends with scattering angle or upon the order of reflection is not well known.

Another nuclear dynamical effect observed was the variation in the quantum beat patterns due to the thickness of the crystal film. In one measurement using the YIG [0 0 10] reflection, the nuclear dynamical theory gave a thickness ($2.6\mu\text{m}$) that was inconsistent with a measurement made during the fabrication of the crystal film ($6.7\mu\text{m}$). With more careful diffraction experiments to measure the rocking curve of the crystal, the dynamical theory was vindicated--the rocking curve measurements showed that the crystal had bifurcated into two layers having different lattice constants. Thus, dynamical effects were shown to be sensitive to thickness variations in a crystal.

Nuclear dynamical diffraction theory was also tested in a double crystal reflection experiment. In this case, the idea of a collective state must be extended to two crystals separated in space. However, since diffraction is essentially a phased scattering phenomena, the separation of two crystals poses no problem as long as all of the diffracting particles have the same spatial phases (modulo 2π). The two crystal YIG $[0\,0\,2]-[0\,0\,2]$ reflection data was well explained by dynamical diffraction theory for different orientations of the internal magnetic field across each crystal. A double crystal

YIG [0 0 2]−[0 0 4] reflection experiment was also done. This experiment showed that, using the first [0 0 2] crystal as a monochromator source, an electronically allowed [0 0 4] reflection could be probed. Without the YIG [0 0 2] crystal, the photoelectric prompt reflection would have overwhelmed the detector (a scintillator coincidence photodetector where the scintillator is a plastic material possessing a short fluorescent lifetime).

Nuclear dynamical scattering theory is necessary to describe the results of time-resolved Mössbauer spectroscopy principally because multiple scattering is no longer insignificant. However, there remains a whole host of physical phenomena that have nothing to do with multiple scattering (such as nuclear hyperfine structure quantum beats, the orientation and strength of the various hyperfine fields, nuclear level mixing, polarization and angular scattering characteristics, and angular interferometry) which were also investigated in this thesis.

One such kinematic effect investigated involved a dual time and frequency experiment that utilized information from both frequency and time space. A "black" Mössbauer absorber was used to completely filter out the inner two lines of a hyperfine split YIG spectrum. The inner magnetic field was oriented nominally parallel to the incident and outgoing photon directions. For such a case, filtering out the inner two lines prevents any magnetic beating. The time-resolved experiment showed no fast magnetic hyperfine beats--only a slow electric quadrupole beat remained (due to the beating between lines from iron nuclei lying in different crystallographic sites).

Another kinematic scattering phenomena investigated involved a situation in which time domain measurements have advantages over frequency domain measurements. This advantage lies in the ability to easily detect relative phase differences between resonant amplitudes. Since resonant lines are usually spaced far apart, very little phase information can be extracted from the interference between the lines. However, since the interference between resonant lines shows up as a beat pattern in the time domain, phase shifts in the amplitudes show up as clearly observable shifts in the beat patterns.

An angular interferometry experiment took full advantage of the ability to observe purely geometrical phase changes in the time domain. In this experiment, the phase shift of the quantum state of a photon that has undergone a rotation was measured--these phase shifts are purely geometrical effects independent of dynamical, or multiple, scattering or the number of scatterers. By using nuclear transitions, photons could be prepared having a definite component of angular momentum along a quantization axis (the internal

magnetic field direction). These photons underwent phase shifts depending upon the amount of azimuthal (angular momentum-conserving) rotation about the quantization axis. These phase shifts were observed to be different between right-handed rotations and left-handed rotations about the quantization axis. For scattering angles near 45°, the phase difference was large enough to shift the quantum beat patterns for right and left-handed rotations almost 180° out of phase. Such striking phase effects would be extremely difficult, if not impossible, to observe through traditional Mössbauer velocity experiments.

One interesting question that may be posed by Mössbauer experimentalists is whether measurements made in the time domain reveal any information that cannot be obtained by traditional measurements in the frequency domain. For the samples used in this thesis, both time-resolved and conventional Mössbauer spectroscopy would most likely yield the same results when analyzing the internal hyperfine fields. The hyperfine field values for the internal magnetic field and the electric quadrupole splitting could be measured to within 1-2% through the analysis of quantum beat patterns. This is about as well as traditional Mössbauer velocity measurements. Where time-resolved measurements using synchrotron x-ray sources become more useful is in hyperfine field measurements of samples that are not amenable to conventional Mössbauer spectroscopy. For example, when using radioactive sources, the scattering intensity from extremely small samples is generally too small to extract information about the hyperfine fields. Such samples may include materials in highly pressurized diamond anvil cells where magnetic phase transitions can be explored, or nanostructures and micro-crystals where one, two, or three dimensional magnetism can be explored. For instance, one dimensional magnetism can be investigated in small magnetic fibers, and two dimensional magnetism can be explored in the surface layer of materials or in thin magnetic crystal or multilayer films composed of only a few monolayers of resonant nuclei. When the third generation synchrotron sources are constructed, undulator beamlines should be able to provide the necessary high brilliance to make such measurements not only possible but straightforward.

APPENDIX A

A.1 Angular Interferometry (Physical Review Letter)

The discussion in Chapter 5 explored the properties of angular phase shifts from the perspective of the S and T-matrix scattering formalism presented in the previous chapters. To complement the discussion, the angular phase shifts are understood in this appendix by using the fundamental rotational and mirror symmetry properties of free space which leads to the realization that bosons, such as photons, essentially behave as three dimensional irreducible representations of the group $O^+(3)$. (In a similar fashion, these symmetry properties reveal that fermions, such as electrons or neutrons, can be realized as two dimensional irreducible representations of the group $SU(2)$.) The following is a recently published journal article: D. E. Brown, J. Arthur, A. Q. R. Baron, G. S. Brown, and S. Shastri, *Phys. Rev. Lett.* **69**, 699 (1992).

Phase Shift of a Rotated Quantum State Observed in an X-ray Scattering Experiment

D. E. Brown, J. Arthur, A. Q. R. Baron
Stanford Synchrotron Radiation Laboratory, P. O. Box 4349, Bin 69, Stanford, California 94309

G. S. Brown
Dept. of Physics, University of California at Santa Cruz, Santa Cruz, California 95064

S. Shastri
Cornell High Energy Synchrotron Source and the School of Applied and Engineering Physics, Cornell Univ., Ithaca NY 14853

Abstract

The rotation of the reference frame of a particle is known to lead to a phase change of its wavefunction proportional to its angular momentum. This can manifest itself as an angle-dependent phase shift of a photon scattered by a fixed target, when the photon state is an eigenstate of the component of total angular momentum perpendicular to the scattering plane. This phase shift has been observed in the quantum beat pattern resulting from the transient excitation of ^{57}Fe nuclei by synchrotron radiation.

PACS number: 03.65.-w,78.70.Ck,42.10.Jd,76.80.+y

Quantum wavefunctions and classical wave fields reflect the symmetries of space and time that result in conservation laws and phase factors involving the conserved quantities. For example, the homogeneity of time leads to the conservation of energy and the uniformity of space leads to the conservation of total linear momentum for an isolated system. Such systems are invariant under translations in time or space, and the translated wavefunctions acquire phase shifts depending on the conserved values.[1,2] For simple eigenstates of energy and linear momentum

$$\psi(t+\Delta t)=e^{-iH\Delta t/\hbar}\psi(t) \tag{1}$$

$$\psi(\mathbf{r}-\Delta\mathbf{r})=e^{-i\Delta\mathbf{r}\cdot\mathbf{p}/\hbar}\psi(\mathbf{r}). \tag{2}$$

Of particular interest in this Letter are the effects of rotations on the properties of a system. Rotational symmetry results in the conservation of total angular momentum, $\mathbf{J}$, and a rotated eigenstate acquires an angular phase shift:

$$\psi(\phi-\Delta\phi)=e^{-i\Delta\phi\cdot\mathbf{J}/\hbar}\psi(\phi). \tag{3}$$

A vivid consequence of this angular phase is the 4π rotational symmetry of fermions that has been demonstrated in neutron interferometer experiments.[3-5] The angular phases for photons are dramatically illustrated in this Letter in an elastic scattering experiment involving resonant scattering of x-rays from nuclei.

Considering only basic symmetry properties of free space (such as rotational and mirror symmetry) angular momentum wavefunctions of a general particle can be constructed. The rotational symmetry properties lead to the formation of irreducible representations, $D^{(j)}\left(\hat{\mathbf{k}}\rightarrow\hat{\mathbf{z}}\right)$, describing rotations of a system with quantization axis $\hat{\mathbf{k}}$ into a system with quantization axis $\hat{\mathbf{z}}$, and having rotation-angle-dependent matrix elements that depend only upon the geometry of space and not upon the dynamics, or interactions, in the system. When j (the total angular momentum quantum number) is integral, these irreducible representations are naturally present in classical electrodynamics in the multipole field solutions of the Maxwell equations.

Consider a process that changes the direction of propagation of a photon without changing its total angular momentum. According to Eq.(3), a phase shift should arise depending on the projection of the total angular momentum along the axis of rotation. The angular momentum of a photon perpendicular to its direction of propagation is often not well-defined, but a photon state of well-defined propagation direction can be expanded in terms of basis states (spherical helicity states) having well-defined angular momenta about an axis that is not necessarily the propagation direction. Superpositions of these basis states form the multipole vector spherical harmonics.[6] In this case the total angular momentum

includes orbital angular momentum, and need not be limited to the photon spin value of 1. The rotated photon state has a phase factor $e^{-iM\Delta\phi}$, and the transition amplitude for forming such a rotated state has the conjugate phase factor $e^{+iM\Delta\phi}$. The quantity $\Delta\phi$ is the change in the photon's direction expressed as an azimuthal angle in a spherical coordinate system aligned along the axis of rotation, and M is the projection of the photon's total angular momentum along that axis. (If expressed in a spherical coordinate system that is not aligned along the rotation axis, the rotated wavefunction will in general also depend on the values of the polar angles of the photon propagation vectors.) The phase factor $e^{iM\Delta\phi}$ is independent of the polarization of the incident or rotated photon, and it is also independent of the dynamical details of the interaction that causes the photon direction to change.

To measure the angular phase change of a photon, it is sufficient to prepare a photon state with definite angular momentum about an axis perpendicular to its propagation direction, cause the state to rotate about this axis through a known angle without changing its total angular momentum, and observe the interference between the rotated state and another coherent reference photon state. We realized such an experiment using elastic scattering of synchrotron x-rays by nuclear resonances. The photon-nuclear interaction served to select photon states with definite values of M. Bragg scattering served to define the rotation angle, and the coherent, pulsed nature of the synchrotron excitation provided reference photons for the interference measurement.

For the experiment a yttrium iron garnet (YIG) crystal enriched with ^{57}Fe was used in Bragg geometry to diffract an incident beam of 14.4 keV photons through a scattering angle, $2\theta_B$, equal to twice the Bragg angle. The YIG magnetic crystal structure allowed us to observe pure nuclear resonant scattering from a ferromagnetically aligned subset of ^{57}Fe nuclei.[7] A small external magnetic field was used to orient the internal ferromagnetic field perpendicular to the scattering plane, so that the rotation angle of the scattered photons around the nuclear quantization axis was equal to $2\theta_B$.

In a magnetic field, the 14.4 keV ^{57}Fe nuclear resonance is generally split into a hyperfine six line spectrum (see Fig. 1). In our experiment the incident photons, due to the nature of the synchrotron source, were linearly polarized parallel to the nuclear quantization axis. Under these conditions the transitions labeled 2 and 5 in Fig. 1 are not allowed by polarization selection rules. The remaining four transitions are allowed, and the scattering process does not change the polarization state of the light. The two strongest transitions are those labeled 1 and 6 in Fig. 1. They are separated by about 6×10^{-7} eV, and the energy width of each resonance is approximately 5×10^{-9} eV. When excited coherently by an abrupt pulse of synchrotron light, the resonant states decay with a lifetime of about 141 ns. Because states with different frequencies are excited coherently, the decay curve exhibits

interference beats, principally the 7 ns beat period due to the interference of transitions 1 and 6.

Transitions 1 and 6 select photon states having total angular momentum projections along the nuclear quantization axis of $M=-1$ and $M=+1$. Thus, for the line with $M=+1$ the angular phase shift in the scattering amplitude is $2\theta_B$ while for the line with $M=-1$ it is $-2\theta_B$. The time beat pattern resulting from the interference of the two lines is phase retarded by $4\theta_B$:

$$I(t) \sim \left(1+\cos\left[\Delta\omega t - 4\theta_B\right]\right) \tag{4}$$

where $\Delta\omega$ is the beat frequency. If the direction of scattering is reversed (see Fig. 2), the angular phase shifts change sign, resulting in a phase advanced time beat pattern

$$I(t) \sim \left(1+\cos\left[\Delta\omega t + 4\theta_B\right]\right). \tag{5}$$

The time beat pattern contains a phase factor that is twice the scattering angle; the phase factor is negative for right handed rotations around the quantization axis and positive for left handed rotations. The net phase difference between time beat patterns with opposite rotation angles is four times the scattering angle: $8\theta_B$. This is a very noticeable effect for scattering angles near $45°$.

The YIG time beat pattern involves more than two resonant lines (the four lines mentioned above are further split by an electric quadrupole interaction giving a total of 8 lines), so the patterns are more complicated than those described by Eqs.(4) and (5). Yet, since all the lines have $M=\pm 1$, the $8\theta_B$ phase difference is the dominant effect.

The experiment was performed at the 24 pole wiggler beamline F2 at the Cornell High Energy Synchrotron Source (CHESS). A double crystal Si [1 1 1] monochromator provided a source beam having a 2 eV bandwidth at the nuclear resonance energy of 14.413 keV. A gold-coated flat mirror was used in grazing incidence geometry to filter out the higher order harmonics coming through the silicon monochromator. The diffracted light from the YIG crystal was detected by a fast plastic scintillator coincidence detector, and the photon arrival time was recorded by fast timing electronics. Similar experimental techniques have been used in a number of previous resonant nuclear scattering experiments.[8] The angular phase shift was not explicitly noted in these earlier experiments since they either involved small Bragg angles, or they involved antiferromagnetic samples from which all reflections involve both right and left handed scattering rotations. However, it should be pointed out that the angular phase factor is implicitly present in the polarization matrices for nuclear scattering described by various authors.[9-13] We found it experimentally convenient to change the sense of the scattering angle by reversing the

magnetic field direction, but it is conceptually simpler to think of the scattering angle being reversed, as shown in Fig. 2.

YIG $[0\,0\,\pm 10]$ reflections have Bragg angles of $\pm 20°$, giving a net phase difference of 160° between their line 1—line 6 time beat patterns. The peaks of the $[0\,0\,10]$ pattern lie nearly in the valleys of the $[0\,0\,-10]$ pattern. This is shown in Fig. 3 where, despite complications due to the multiplicity of hyperfine levels, the advance or retardation of the 7 ns beat period is clearly visible. To get good fits to the data, we used the full Ewald-Laue dynamical diffraction theory for resonant scatterers,[11,14,15] including small contributions from the electronic and nuclear index of refraction. However, the angular phase shift which advances or retards the observed beat pattern is a purely kinematical, geometrical effect.

Recently, two resonant nuclear scattering experiments have demonstrated shifts in the time beat patterns due to passage of the radiation through the scattering material.[16,17] These shifts are caused by dynamical, index of refraction effects in the material, and they are not related to the angular phase shifts.

The fundamental symmetry properties of wave mechanics predict that an angular momentum-conserving rotation of a wavefunction is accompanied by an angular phase shift. A dramatic way to demonstrate this phase effect involves elastic resonant nuclear scattering of photons. The nuclear scatterer serves as a filter, allowing only photon states with well-defined angular momentum components to pass. Coherent generation of more than one angular momentum state using synchrotron light permits the angular phase shifts to be clearly observed in an interference measurement. A measurement of this type may have practical applications: for a given scattering angle, the time beat pattern can be used to uniquely determine the sign of the magnetic field at the scattering nuclei. In our experiment, the time beat patterns indicate that for the selected ^{57}Fe nuclei (the nuclei occupying the sites in YIG with local tetrahedral symmetry[7]), the internal magnetic field direction is opposite to the external guide field.

Support for this research was provided by the U. S. Department of Energy, Office of Basic Energy Science, Division of Materials Sciences. CHESS is supported by the National Science Foundation under Award No. 90-21700.

REFERENCES

[1] R. L. Liboff, *Introductory Quantum Mechanics* (Holden-Day, San Francisco, 1980).

[2] A. S. Davydov, *Quantum Mechanics* (Pergamon Press, Oxford, 1985).

[3] Y. Aharonov and L. Susskind, *Phys. Rev.* **158**, 1237 (1967).

[4] H. Rauch, A. Zeilinger, G. Badurek, and A. Wilfing, *Phys. Lett.* **54A**, 425 (1975).

[5] S. A. Werner, R. Colella, A. W. Overhauser, and C. F. Eagen, *Phys. Rev. Lett.* **35**,1053 (1975).

[6] V. B. Berestetskii, E. M. Lifshitz, and L. P. Pitaevskii, *Quantum Electrodynamics* (Pergamon Press, Oxford, 1982), vol. 4.

[7] H. Winkler, R. Eisberg, E. Alp, R. Rüffer, E. Gerdau, S. Lauer, A. X. Trautwein, M. Grodzicki, and A. Vera, *Z. Phys. B* **49**, 331 (1983).

[8] E. Gerdau, R. Rüffer, H. Winkler, W. Tolksdorf, C. P. Klages, and J. P. Hannon, *Phys. Rev. Lett.* **54**, 835 (1985); E. Gerdau, R. Rüffer, R. Hollatz, and J. P. Hannon, *Phys. Rev. Lett.* **57**, 1141 (1986); R. Rüffer, E. Gerdau, and R. Hollatz, *Phys. Rev. Lett.* **58**, 2359 (1987); U. van Bürck, R. L. Mössbauer, E. Gerdau, R. Rüffer, R. Hollatz, G. V. Smirnov, and J. P. Hannon, *Phys. Rev. Lett.* **59**, 355 (1987); G. Faigel, D. P. Siddons, J. B. Hastings, P. E. Haustein, J. R. Grover, and L. E. Berman, *Phys. Rev. Lett.* **61**, 2794 (1988); J. Arthur, G. S. Brown, D. E. Brown, and S. L. Ruby, *Phys. Rev. Lett.* **63**, 1629 (1989); S. Kikuta, Y. Yoda, Y. Kudo, K. Izumi, T. Ishikawa, C. K. Suzuki, H. Ohno, H. Takei, K. Nakayama, X. W. Zhang, T. Matsushita, S. Kishimoto, and M. Ando, *Jap. J. App. Phys.* **30**, L 1686 (1991).

[9] H. Frauenfelder, D. E. Nagle, R. D. Taylor, D. R. F. Cochran, and W. M. Visscher, *Phys. Rev.* **126**, 1065 (1962).

[10] M. Blume and O. C. Kistner, *Phys. Rev.* **171**, 417 (1968).

[11] J. P. Hannon and G. T. Trammell, *Phys. Rev.* **186**, 306 (1969).

[12] U. van Bürck, G. V. Smirnov, R. L. Mössbauer, F. Parak, and N. A. Semioschkina, *J. Phys. C* **11**, 2305 (1978).

[13] D. P. Siddons, J. B. Hastings, G. Faigel, L. E. Berman, P. E. Haustein, and J. R. Grover, *Phys. Rev. Lett.* **62**, 1384 (1989).

[14] B. W. Batterman and H. Cole, *Rev. Mod. Phys.* **36**, 681 (1964).

[15] A. M. Afanas'ev and Y. Kagan, *Zh. Eksp. Teor. Fiz.* **48**, 327 (1965) [*JETP* **21**, 215 (1965)]; Y. Kagan, A. M. Afanas'ev, and I. P. Perstnev, *Zh. Eksp. Teor. Fiz.* **54**, 1530 (1968) [*JETP* **27**, 819 (1968)]; Y. Kagan, A. M. Afanas'ev, and V. G. Kohn, *J. Phys. C* **12**, 615 (1979).

[16] A. I. Chumakov, G. V. Smirnov, M. V. Zelepukhin, U. van Bürck, E. Gerdau, R. Rüffer, and H. D. Rüter, *Europhys. Lett.* **17**, 269 (1991).

[17] U. van Bürck, D. P. Siddons, J. B. Hastings, U. Bergmann, and R. Hollatz, (To be published).

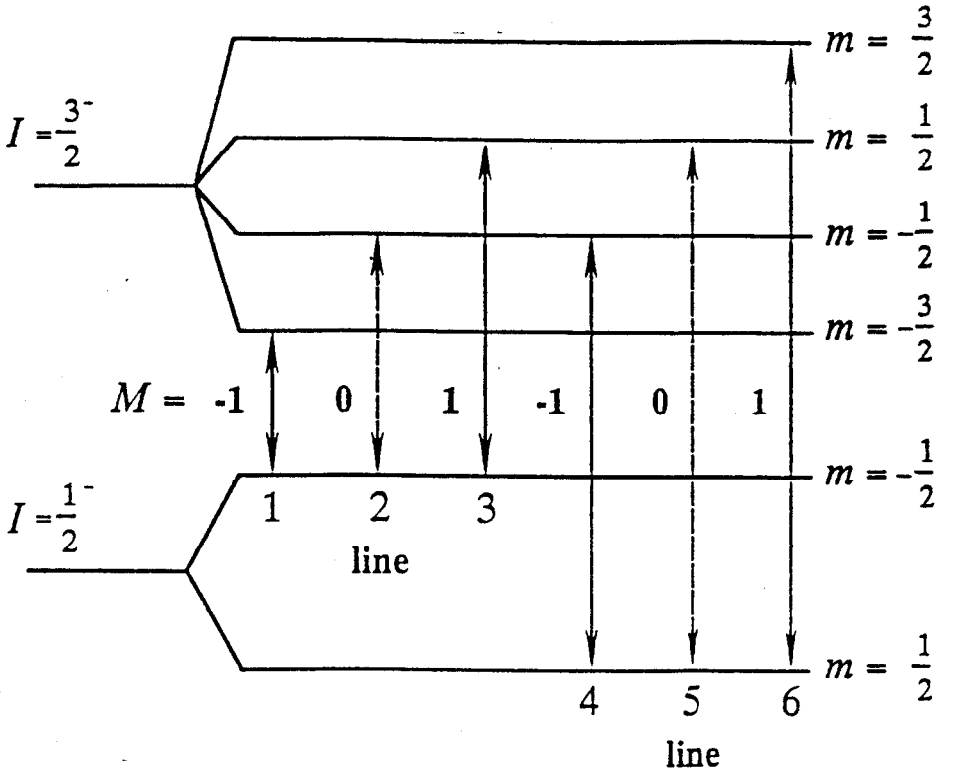

Fig. 1. Hyperfine nuclear resonance of ^{57}Fe. The magnetic quantum numbers are given with respect to a quantum axis oriented parallel to the internal magnetic field. When the magnetic field is perpendicular to the scattering plane, lines 2 and 5 are excitable by and radiate linearly polarized light perpendicular to the magnetic field. The other four lines are excitable by and radiate linearly polarized light parallel to the magnetic field. Radiated photons from lines 1,3,4,6 have the same polarization but different phases depending upon their scattering angles and angular momentum components, M.

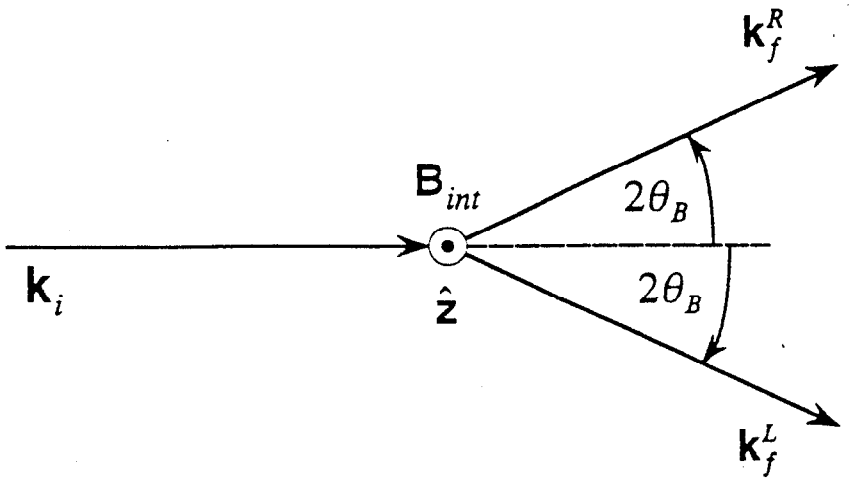

Fig. 2. Complementary scattering geometries. Incident photons $\mathbf{k}_i$ can be scattered by equivalent Bragg reflections in either a right-handed sense $\mathbf{k}_f^R$ or a left-handed sense $\mathbf{k}_f^L$ about the nuclear quantization axis, $\hat{\mathbf{z}}$, parallel to the internal magnetic field $\mathbf{B}_{int}$.

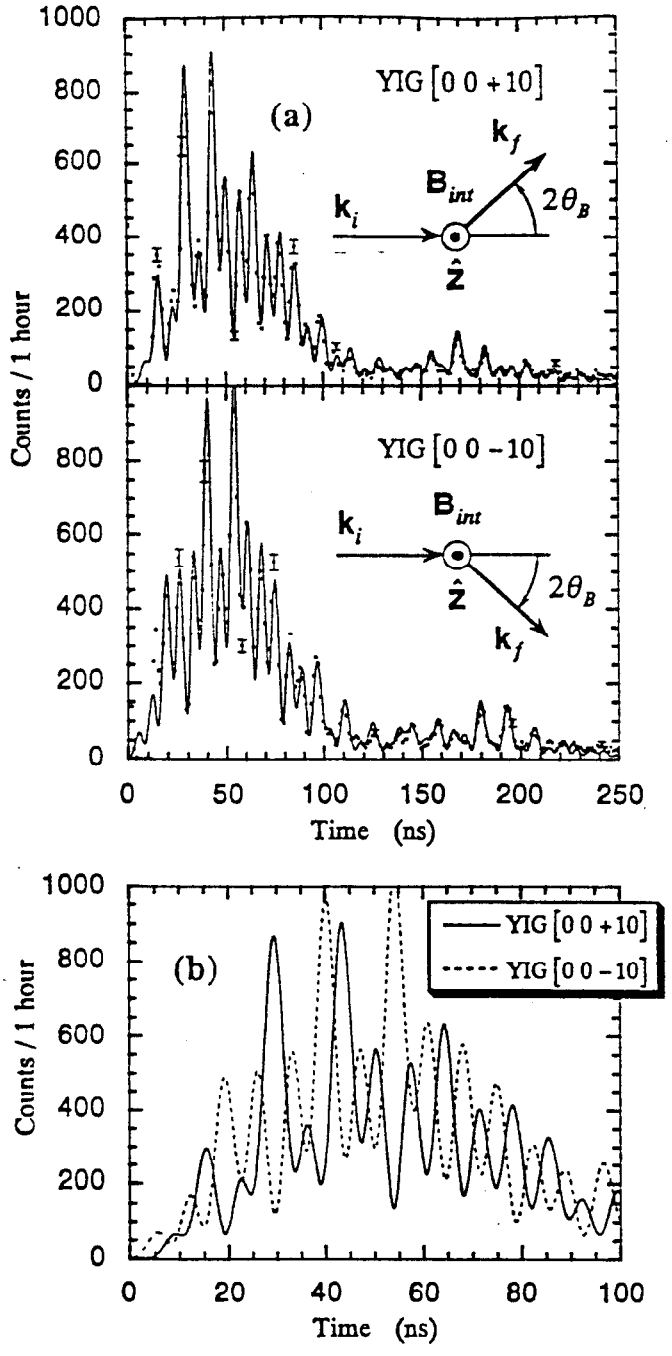

Fig. 3. (a) Time beat patterns for left and right handed scattering. Solid curves are dynamical diffraction theory calculations, including the angular phase. Because some of the interfering transitions share identical M values, the shifted beat patterns are modulated with an unshifted beat pattern of longer period, giving different heights to corresponding intensity peaks in the $[0\ 0\ 10]$ and $[0\ 0\ -10]$ patterns. (b) Expanded, superimposed view of the fits to the data. The nearly 180° phase difference is clearly evident.

APPENDIX B

B.1 Time Domain Calculation for a Plane Parallel Slab of Resonant Scatterers Excited by a ^{57}Co Source

In this example, a plane parallel slab of single line resonant scatterers is excited by a ^{57}Co source. The field emanating from this source will be approximated as a decaying exponential wave Doppler shifted by $\Delta\omega$ to take into account the relative motion between the source and the scatterers:

$$a_0(t,z,z_0) = E_0 e^{ikz_0} e^{-i(\omega_0+\Delta\omega)t-\Gamma t/2\hbar}. \tag{B.1-1}$$

Let the scatterers have the same natural frequency, ω_0, and linewidth, Γ, as the source. The impulse response of the scatterers is then

$$H(t,z',z) = -(\Gamma_s/4\hbar L)e^{-i\omega_0 t-\Gamma t/2\hbar}\theta(t) \tag{B.1-2}$$

where Γ_s is given by Eq. 6-5.16

Using the multiple scattering equations, Eqs. 6-5.11 and 6-5.12, first order scattering gives

$$a_1(t,z,z_0)dz = \int_0^t \left[E_0 e^{ikz_0} e^{-i(\omega_0+\Delta\omega)t'-\Gamma t/2\hbar}\right]\left[-(\Gamma_s/4\hbar L)e^{-i\omega_0(t-t')-\Gamma(t-t')/2\hbar}\right]dt'\,dz$$

$$= A(t)\left(\frac{1}{-i\Delta\omega}\right)\left(e^{-i\Delta\omega t}-1\right)dz \tag{B.1-3}$$

where $$A(t) = -(\Gamma_s/4\hbar L)E_0 e^{ikz_0} e^{-i\omega_0 t-\Gamma t/2\hbar}. \tag{B.1-4}$$

Second order scattering gives

$$a_2(t,z,z_0)dz = \int_0^t\int_0^z dz'A(t')\left(\frac{1}{-i\Delta\omega}\right)\left(e^{-i\Delta\omega t'}-1\right)\left[-(\Gamma_s/4\hbar L)e^{-i\omega_0(t-t')-\Gamma(t-t')/2\hbar}\right]dt'\,dz$$

$$= A(t)\left(\frac{1}{-i\Delta\omega}\right)\left[\left(\frac{1}{-i\Delta\omega}\right)\left(e^{-i\Delta\omega t}-1\right)-t\right]\left[-\left(\frac{\Gamma_s z}{4\hbar L}\right)\right]dz. \tag{B.1-5}$$

Similarly, third and fourth order scattering gives

$$a_3(t,z,z_0)dz = A(t)\left(\frac{1}{-i\Delta\omega}\right)\left[\left(\frac{1}{-i\Delta\omega}\right)\left[\left(\frac{1}{-i\Delta\omega}\right)\left(e^{-i\Delta\omega t}-1\right)-t\right]-\frac{t^2}{2!}\right]\left[\left(\frac{\Gamma_s z}{4\hbar L}\right)^2\frac{1}{2!}\right]dz \tag{B.1-6}$$

$$a_3(t,z,z_0)dz = A(t)\left(\frac{1}{-i\Delta\omega}\right)\left[\left(\frac{1}{-i\Delta\omega}\right)\left[\left(\frac{1}{-i\Delta\omega}\right)\left[\left(\frac{1}{-i\Delta\omega}\right)\left(e^{-i\Delta\omega t}-1\right)-t\right]-\frac{t^2}{2!}\right]-\frac{t^3}{3!}\right]$$

$$\times\left[-\left(\frac{\Gamma_s z}{4\hbar L}\right)^3\frac{1}{3!}\right]dz. \qquad \text{(B.1-7)}$$

Adding up all the scattering terms, and ordering them in powers of $-1/i\Delta\omega$ results in a comprehensible series expansion:

$(a_1 + a_2 + a_3 + a_4 + \cdots)dz =$

$$= A(t)\left\{\left(\frac{e^{-i\Delta\omega t}}{-i\Delta\omega}\right)\left[1-\frac{\Gamma_s z}{4\hbar L(-i\Delta\omega)}+\left(\frac{\Gamma_s z}{4\hbar L(-i\Delta\omega)}\right)^2\frac{1}{2!}-\left(\frac{\Gamma_s z}{4\hbar L(-i\Delta\omega)}\right)^3\frac{1}{3!}+\cdots\right]\right.$$

$$-\left(\frac{1}{-i\Delta\omega}\right)\left[1-\frac{\Gamma_s zt}{4\hbar L}+\left(\frac{\Gamma_s zt}{4\hbar L}\right)^2\frac{1}{(2!)^2}-\left(\frac{\Gamma_s zt}{4\hbar L}\right)^3\frac{1}{(3!)^2}+\cdots\right]$$

$$-\left(\frac{1}{-i\Delta\omega}\right)^2\left[-\frac{\Gamma_s z}{4\hbar L}+\left(\frac{\Gamma_s z}{4\hbar L}\right)^2\frac{1}{2!}t-\left(\frac{\Gamma_s z}{4\hbar L}\right)^3\frac{1}{3!}\frac{t^2}{2!}+\cdots\right]$$

$$-\left(\frac{1}{-i\Delta\omega}\right)^3\left[\left(\frac{\Gamma_s z}{4\hbar L}\right)^2\frac{1}{2!}-\left(\frac{\Gamma_s z}{4\hbar L}\right)^3\frac{1}{3!}t+\cdots\right]$$

$$\left.-\left(\frac{1}{-i\Delta\omega}\right)^4\left[-\left(\frac{\Gamma_s z}{4\hbar L}\right)^3\frac{1}{3!}+\cdots\right]-\cdots\right.$$

$$= A(t)\left\{\left(\frac{e^{-i\Delta\omega t}}{-i\Delta\omega}\right)e^{-[\Gamma_s z/4\hbar L(-i\Delta\omega)]}-\left(\frac{i}{\Delta\omega}\right)J_0\left(\sqrt{\Gamma_s zt/\hbar L}\right)-\left(\frac{i}{\Delta\omega}\right)^2\frac{\partial}{\partial t}J_0\left(\sqrt{\Gamma_s zt/\hbar L}\right)\right.$$

$$\left.-\left(\frac{i}{\Delta\omega}\right)^3\frac{\partial^2}{\partial t^2}J_0\left(\sqrt{\Gamma_s zt/\hbar L}\right)-\cdots-\left(\frac{i}{\Delta\omega}\right)^{n+1}\frac{\partial^n}{\partial t^n}J_0\left(\sqrt{\Gamma_s zt/\hbar L}\right)\right\}. \qquad \text{(B.1-8)}$$

Using the expression for the scattering channel field, Eq. 6-5.13, and using the relations

$$\int_0^L J_0\left(\sqrt{\Gamma_s zt/\hbar L}\right)dz = 2L\frac{J_1\left(\sqrt{\Gamma_s t/\hbar}\right)}{\sqrt{\Gamma_s t/\hbar}} \qquad \text{(B.1-9)}$$

and
$$\frac{\partial^n}{\partial t^n}\frac{J_1\left(\sqrt{\Gamma_s t/\hbar}\right)}{\sqrt{\Gamma_s t/\hbar}} = \left(\frac{-\Gamma_s}{2\hbar}\right)^n \frac{J_{n+1}\left(\sqrt{\Gamma_s t/\hbar}\right)}{\left(\sqrt{\Gamma_s t/\hbar}\right)^{n+1}} \tag{B.1-10}$$

gives

$$E_{scf}(t,L,z_0) = E_0 e^{ikz_0} e^{-i\omega_0 t - \Gamma t/2\hbar}\left\{ e^{-i\left[\frac{\Gamma_s}{4\hbar\Delta\omega}+\Delta\omega t\right]} - \sum_{n=1}^{\infty}\left(\frac{-i\Gamma_s}{2\hbar\Delta\omega}\right)^n \frac{J_n\left(\sqrt{\Gamma_s t/\hbar}\right)}{\left(\sqrt{\Gamma_s t/\hbar}\right)^n}\right\}. \tag{B.1-11}$$

This expression can be simplified by using the generating function for Bessel functions:

$$e^{\frac{1}{2}x\left(u-\frac{1}{u}\right)} = \sum_{m=-\infty}^{\infty} u^m J_m(x). \tag{B.1-12}$$

Then

$$\sum_{n=1}^{\infty}\left(\frac{-i\Gamma_s}{2\hbar\Delta\omega}\right)^n \frac{J_n\left(\sqrt{\Gamma_s t/\hbar}\right)}{\left(\sqrt{\Gamma_s t/\hbar}\right)^n} = \sum_{n=-\infty}^{\infty}\left(\frac{-i\Gamma_s}{2\hbar\Delta\omega}\right)^n \frac{J_n\left(\sqrt{\Gamma_s t/\hbar}\right)}{\left(\sqrt{\Gamma_s t/\hbar}\right)^n} - \sum_{n=-\infty}^{0}\left(\frac{-i\Gamma_s}{2\hbar\Delta\omega}\right)^n \frac{J_n\left(\sqrt{\Gamma_s t/\hbar}\right)}{\left(\sqrt{\Gamma_s t/\hbar}\right)^n}$$

where
$$\sum_{n=-\infty}^{\infty}\left(\frac{-i\Gamma_s}{2\hbar\Delta\omega}\right)^n \frac{J_n\left(\sqrt{\Gamma_s t/\hbar}\right)}{\left(\sqrt{\Gamma_s t/\hbar}\right)^n} = e^{-i\left[\frac{\Gamma_s}{4\hbar\Delta\omega}+\Delta\omega t\right]}$$

and
$$\sum_{n=-\infty}^{0}\left(\frac{-i\Gamma_s}{2\hbar\Delta\omega}\right)^n \frac{J_n\left(\sqrt{\Gamma_s t/\hbar}\right)}{\left(\sqrt{\Gamma_s t/\hbar}\right)^n} = \sum_{n=0}^{\infty}\left(\frac{-i2\hbar\Delta\omega}{\Gamma_s}\right)^n \left(\sqrt{\Gamma_s t/\hbar}\right)^n J_n\left(\sqrt{\Gamma_s t/\hbar}\right).$$

Finally, after collecting all terms, the scattering channel field can be expressed as

$$E_{scf}(t,L,z_0) = E_0 e^{ikz_0} e^{-i\omega_0 t - \Gamma t/2\hbar}\sum_{n=0}^{\infty}\left(\frac{-i2\hbar\Delta\omega}{\Gamma_s}\right)^n \left(\sqrt{\Gamma_s t/\hbar}\right)^n J_n\left(\sqrt{\Gamma_s t/\hbar}\right). \tag{B.1-13}$$

This result agrees precisely with Lynch, Holland, and Hamermesh's Fourier transform solution using contour integral methods.[1] The obvious drawback to this time domain multipole scattering approach is that one must have a deft faculty towards massaging complicated infinite series expansions into familiar analytical functions. The beauty of this time domain formalism is that one may completely work out problems entirely in the time domain and observe how the physics evolves at each step of the calculation--performing Fourier transforms can obscure the actual physics behind the scattering process (for instance, the entire issue of multiple scattering appears to be completely absent in the Fourier transform method).

REFERENCES

[1] F. J. Lynch, R. E. Holland, and M. Hamermesh, *Phys. Rev.* **120**, 513 (1960).

B.2 Investigation of the Dynamical Phase between Two Resonant Lines Excited by a Synchrotron Source

In this example the dynamical phase between two widely spaced resonant lines is calculated using the time domain multiple scattering formalism. For a plane parallel slab of scatterers, this phase is shown to be proportional to the thickness of the slab and inversely proportional to the frequency separation between the resonant lines. The source field incident upon the slab is a synchrotron pulse

$$a_0(t,z,z_0) = E_0 e^{ikz_0}\delta(t), \tag{B.2-1}$$

and the impulse response of the system of scatterers is the sum of two resonant amplitudes

$$H(t,z',z) = -(\Gamma_s/4\hbar L)\left\{e^{-i\omega_1 t} + e^{-i\omega_2 t}\right\}e^{-\Gamma t/2\hbar}\theta(t) \tag{B.2-2}$$

where Γ_s is given by Eq. 6-5.16, and ω_1 and ω_2 are the two resonant frequencies.

Using the multiple scattering equations, Eqs. 6-5.11 and 6-5.12, the first order scattered field amplitude is

$$a_1(t,z,z_0)\,dz = \int_0^t\left[E_0 e^{ikz_0}\delta(t')\right]\left[-(\Gamma_s/4\hbar L)\left\{e^{-i\omega_1(t-t')} + e^{-i\omega_2(t-t')}\right\}e^{-\Gamma(t-t')/2\hbar}\right]dt'\,dz$$

$$= A(t)\left\{1 + e^{-i\Delta\omega t}\right\}dz \tag{B.2-3}$$

where $$A(t) = -(\Gamma_s/4\hbar L)E_0 e^{ikz_0}e^{-i\omega_1 t - \Gamma t/2\hbar}, \tag{B.2-4}$$

and $$\Delta\omega = \omega_2 - \omega_1. \tag{B.2-5}$$

The second order scattered field amplitude is

$$a_2(t,z,z_0)\,dz = \int_0^t\int_0^z dz' A(t')\left\{1 + e^{-i\Delta\omega t'}\right\}\left[\left(A(t-t')e^{-ikz_0}/E_0\right)\left\{1 + e^{-i\Delta\omega(t-t')}\right\}\right]dt'\,dz$$

$$= A(t)\left[-\left(\frac{\Gamma_s z}{4\hbar L}\right)\right]\left\{t\left(1 + e^{-i\Delta\omega t}\right) + \frac{2}{i\Delta\omega}\left(1 - e^{-i\Delta\omega t}\right)\right\}dz. \tag{B.2-6}$$

Crunching out the convolution integrals for the third and fourth order scattered field amplitudes give

$$a_3(t,z,z_0)\,dz = A(t)\left[\left(\frac{\Gamma_s z}{4\hbar L}\right)^2\frac{1}{2!}\right]\left\{\frac{t^2}{2!}\left(1 + e^{-i\Delta\omega t}\right) + \frac{3t}{i\Delta\omega}\left(1 - e^{-i\Delta\omega t}\right)\right\}dz \tag{B.2-7}$$

and $$a_4(t,z,z_0)dz = A(t)\left[-\left(\frac{\Gamma_s z}{4\hbar L}\right)^3\frac{1}{3!}\right]\left\{\frac{t^3}{3!}\left(1+e^{-i\Delta\omega t}\right)+\frac{4t^2}{(i\Delta\omega)2!}\left(1-e^{-i\Delta\omega t}\right)\right.$$

$$\left.+\frac{2t}{(i\Delta\omega)^2}\left(1+e^{-i\Delta\omega t}\right)-\frac{4}{(i\Delta\omega)^3}\left(1-e^{-i\Delta\omega t}\right)\right\}dz. \quad \text{(B.2-8)}$$

The sum of the scattering terms up to fourth order can be expressed in a series expansion in $1/i\Delta\omega$:

$a_1+a_2+a_3+a_4+\cdots =$

$$= A(t)\left(1+e^{-i\Delta\omega t}\right)\left\{1-\left(\frac{\Gamma_s zt}{4\hbar L}\right)+\left(\frac{\Gamma_s zt}{4\hbar L}\right)^2\frac{1}{(2!)^2}-\left(\frac{\Gamma_s zt}{4\hbar L}\right)^3\frac{1}{(3!)^2}+\cdots\right\} \quad (1)$$

$$+A(t)\frac{\left(1-e^{-i\Delta\omega t}\right)}{(i\Delta\omega)}\left\{-2\left(\frac{\Gamma_s z}{4\hbar L}\right)+3t\left(\frac{\Gamma_s z}{4\hbar L}\right)^2\frac{1}{2!}-\frac{4t^2}{2!}\left(\frac{\Gamma_s z}{4\hbar L}\right)^3\frac{1}{3!}+\cdots\right\} \quad (2)$$

$$+A(t)\frac{\left(1+e^{-i\Delta\omega t}\right)}{(i\Delta\omega)^2}\left\{-2t\left(\frac{\Gamma_s z}{4\hbar L}\right)^3\frac{1}{3!}+\cdots\right\} \quad (3)$$

$$+A(t)\frac{\left(1-e^{-i\Delta\omega t}\right)}{(i\Delta\omega)^3}\left\{4\left(\frac{\Gamma_s z}{4\hbar L}\right)^3\frac{1}{3!}+\cdots\right\}+\cdots. \quad \text{(B-2.9)}$$

Whether this series expansion can be expressed in a compact analytical form is unknown, but, for widely separated lines, summing all the scattering terms is unnecessary. To first order in $1/i\Delta\omega$ only the first two separate series expansions labeled (1) and (2) in the expression above need be evaluated.

Using the Bessel function identity in Eq. 6-5.20, the series expansion (1) reduces to

$$(1) \longrightarrow A(t)\left(1+e^{-i\Delta\omega t}\right)J_0\left(\sqrt{\Gamma_s zt/\hbar L}\right),$$

and (2) reduces to the simpler form

$$(2) \longrightarrow A(t)\frac{\left(1-e^{-i\Delta\omega t}\right)}{(i\Delta\omega)}\frac{\partial^2}{\partial H_0\partial t}\left[H_0 J_0\left(2\sqrt{H_0 zt}\right)\right]$$

where $$H_0 = \Gamma_s/4\hbar L. \quad \text{(B-2.10)}$$

Using the relations expressed in Eqs. B.1-9 and B.1-10 and the following Bessel function relationships

$$\frac{\partial}{\partial t}\frac{J_1\left(\sqrt{4H_0Lt}\right)}{\sqrt{4H_0Lt}} = -\frac{1}{2t}J_2\left(\sqrt{4H_0Lt}\right) \tag{B-2.11}$$

$$\frac{d}{dx}J_n(x) = \frac{1}{2}\left[J_{n-1}(x) - J_{n+1}(x)\right] \tag{B-2.12}$$

$$J_{n-1}(x) = \frac{2n}{x}J_n(x) - J_{n+1}(x), \tag{B-2.13}$$

and after a little algebra, the scattering channel field (Eq. 6-5.13) reduces, to first order in $1/i\Delta\omega$, to

$$E_{scf}(t) = E_0 e^{ikz_0}\left\{\delta(t) - e^{-i\omega_1 t - \Gamma t/2\hbar}\frac{\Gamma_s}{2\hbar}\frac{J_1\left(\sqrt{\Gamma_s t/\hbar}\right)}{\sqrt{\Gamma_s t/\hbar}}\left[\left(1+e^{-i\Delta\omega t}\right) + i\frac{\Gamma_s}{4\hbar\Delta\omega}\left(1-e^{-i\Delta\omega t}\right)\right]\right\} \tag{B-2.14}$$

Ignoring the prompt delta function pulse, the resonant intensity is then

$$I_{res}(t) = \left|E_{scf}(t) - E_0 e^{ikz_0}\delta(t)\right|^2$$

$$= 2E_0^2\left(\frac{\Gamma_s}{2\hbar}\right)^2\left[1+\left(\frac{\Gamma_s}{4\hbar\Delta\omega}\right)^2\right]\left(\frac{J_1\left(\sqrt{\Gamma_s t/\hbar}\right)}{\sqrt{\Gamma_s t/\hbar}}\right)^2\left\{1+\cos(\Delta\omega t+\phi)\right\}e^{-\Gamma t/\hbar} \tag{B-2.15}$$

$$= 4E_0^2\left(\frac{\Gamma_s}{2\hbar}\right)^2\left[1+\left(\frac{\Gamma_s}{4\hbar\Delta\omega}\right)^2\right]\left(\frac{J_1\left(\sqrt{\Gamma_s t/\hbar}\right)}{\sqrt{\Gamma_s t/\hbar}}\right)^2\cos^2\left(\frac{\Delta\omega t}{2}+\frac{\phi}{2}\right)e^{-\Gamma t/\hbar} \tag{B-2.16}$$

where $\phi = \tan^{-1}\left\{\dfrac{2(\Gamma_s/4\hbar\Delta\omega)}{1-(\Gamma_s/4\hbar\Delta\omega)^2}\right\}$. (B-2.17)

The expression above is similar to the field intensity from a plane parallel slab (described in Section 6-5) multiplied by a sinusoidal beating term due to the beating between lines having different resonant frequencies. The interesting phenomenon is the dynamical phase shift, ϕ, of the quantum beat pattern. This dynamical phase shift is related to the thickness-rate, $\Gamma_s = n\sigma_0 L\Gamma$, and the splitting between the two resonance lines, $\Delta\omega$. Thus, when the splitting is large compared to the thickness-rate, $\Delta\omega >> \Gamma_s/4\hbar$, ϕ is directly proportional to the thickness of the slab and inversely proportional to the frequency separation of the resonance lines:

$$\phi \approx \Gamma_s/2\hbar\Delta\omega = \Gamma n\sigma_0 L/2\hbar\Delta\omega \tag{B-2.18}$$

This dynamical phase shift has been seen by van Bürck *et. al.*,[1] and, in the comparison of their data with Eq. B.2-15, the time domain multiple scattering formalism accurately describes the phase shift phenomenon for all thicknesses of the sample. The calculations van Bürck *et. al.* performed to fit their data relied upon the frequency domain Fourier transform method. Unfortunately, analytically performing the Fourier transform is difficult, so the fits were done by numerically Fourier transforming the frequency response, and this prevented any insight into the physics behind the dynamical phase shift. (One can integrate the Fourier transform using the method of contour integration, but the result is a complicated series expansion requiring a laborious amount of algebra to extricate the results expressed by Eq. B.2-15). The beauty of the multiple scattering formalism is that the physics behind the scattering process can be investigated at each order of scattering.

REFERENCES

[1] U. van Bürck, D. P. Siddons, J. B. Hastings, U. Bergmann, and R. Hollatz, *Phys. Rev. B* , (To be published).

BIBLIOGRAPHY

A. Abragam and R. V. Pound, *Phys. Rev.* **92**, 943 (1953).

M. Abramowitz and I. A. Stegun, *Handbook of Mathematical Functions* (National Bureau of Standards, Washington D.C., 1972).

A. M. Afanas'ev and Y. Kagan, *Sov. Phys. JETP* **21**, 215 (1965).

Y. Aharonov and L. Susskind, *Phys. Rev.* **158**, 1237 (1967).

A. I. Akhiezer, *Quantum Electrodynamics* (Interscience Publishers, New York, 1965).

K. Alder, A. Bohr, T. Huus, B. Mottelson, and A. Winther, *Revs. Mod. Phys.* **28**, 432 (1956).

E. B. Alexandrov, *Opt. Spectrosc.* **17**, 957 (1964).

C. Alf and G. K. Wertheim, *Phys. Rev.* **122**, 1414 (1961).

A. N. Artem'ev, I. P. Perstnev, V. V. Sklyarevskii, G. V. Smirnov, and E. P. Stepanov, *Sov. Phys.-JETP* **37**, 261 (1973).

J. Arthur, G.S. Brown, D.E. Brown, and S. L. Ruby, *Phys. Rev. Lett.* **63**, 1629 (1989).

J. Arthur, D. E. Brown, S. L. Ruby, G. S. Brown, and G. K. Shenoy, *J. Appl. Phys.* **67**, 5704 (1990).

K. Bane, K. Halbach, K.-J. Kim, J. Kirz, P. Morton, H.-D. Nuhn, C. Pellegrini, J. Rosenzweig, J. Seeman, R. Tatchyn, and H. Winick, *The 2 to 4 nm High Power Linear Coherent Light Source*, Workshop on Applications of X-ray FELs (Stanford University, Stanford, Ca., 1992),

S. S. Bashkirov, N. G. Ivoilov, and V. A. Chistyakov, *Sov. Phys.-Solid State* **13**, 570 (1971).

B. W. Batterman and H. Cole, *Rev. Mod. Phys.* **36**, 681 (1964).

R. Bauminger, S. G. Cohen, A. Marinov, and S. Ofer, *Phys. Rev.* **122**, 743 (1961).

V. N. Belogurov, V. A. Bylinkin, and V. I. Mosel, *Izv. Akad. Nauk. Latv. SSR* **3**, 3 (1979 Fizika Atomnogo Yadra I Spectroskopiya Atomov I Molekul).

G. N. Belozerskii, Y. P. Khimich, and V. N. Gitsovich, *Phys. Stat. Sol. (b)* **79**, K125 (1977).

V. A. Belyakov, *Sov. Phys. -Usp.* **18**, 267 (1975).

V. B. Berestetskii, E. M. Lifshitz, and L. P. Pitaevskii, *Quantum Electrodynamics* (Pergamon Press, Oxford, 1982), vol. 4.

I. Bernal, C. W. Struck, and J. G. White, *Acta Cryst.* **16**, 849 (1963).

P. J. Black and P. B. Moon, *Nature (London)* **188**, 481 (1960).

P. J. Black and I. P. Duerdoth, *Proc. Phys. Soc.* **84**, 169 (1964).

M. Blume and O. C. Kistner, *Phys. Rev.* **171**, 417 (1968).

A. I. Borisenko and I. E. Tarapov, *Vector and Tensor Analysis with Applications* (Dover, New York, 1968).

E. O. Brigham, *The Fast Fourier Transform* (Prentice Hall, Englewood Cliffs, 1974).

D. M. Brink and G. R. Satchler, *Angular Momentum* (Clarendon Press, Oxford, 1968).

D. E. Brown, J. Arthur, A. Q. R. Baron, G. S. Brown, and S. Shastri, *Phys. Rev. Lett.* **69**, 699 (1992).

M. Brunel and F. D. Bergevin, *Acta Cryst.* **A37**, 324 (1981).

U. van Bürck, G. V. Smirnov, R. L. Mössbauer, F. Parak, and N. A. Semioschkina, *J. Phys. C: Solid State Phys.* **11**, 2305 (1978).

U. van Bürck, G. V. Smirnov, R. L. Mössbauer, H. J. Maurus, and N. A. Semioschkina, *J. Phys. C: Solid St. Phys.* **13**, 4511 (1980).

U. van Bürck, R. L. Mössbauer, E. Gerdau, R. Rüffer, R. Hollatz, G. V. Smirnov, and J. P. Hannon, *Phys. Rev. Lett.* **59**, 355 (1987).

U. van Bürck, D. P. Siddons, J. B. Hastings, U. Bergmann, and R. Hollatz, *Phys. Rev. B*, (To be published).

W. R. Busing and H. A. Levy, *Angle Calculations for 3- and 4-Circle X-Ray and Neutron Diffractometers*, ORNL Report 4056 (Oak Ridge National Laboratory, Oak Ridge, Tenn., 1967).

A. I. Chechin, N. V. Andronova, M. V. Zelepukhin, A. N. Artem'ev, and E. P. Stepanov, *JETP Lett.* **37**, 633 (1983).

A. I. Chumakov, G. V. Smirnov, M. V. Zelepukhin, U. van Bürck, E. Gerdau, R. Rüffer, and H. D. Rüter, *Europhys. Lett.* **17**, 269 (1991).

A. I. Chumakov, G. V. Smirnov, M. V. Zelepukhin, U. van Bürck, E. Gerdau, R. Rüffer, and H. D. Rüter, *Hyp. Int.* **71**, 1341 (1992).

R. L. Cohen, G. L. Miller, and K. W. West, *Phys. Rev. Lett.* **41**, 381 (1978).

C. Cohen-Tannoudji, B. Diu, and F. Laloë, *Quantum Mechanics* (Wiley, New York, 1977).

R. Colella, *Acta Cryst.* **A30**, 413 (1974).

D. T. Cromer and D. Liberman, *J. Chem. Phys.* **53**, 1891 (1970).

A. S. Davydov, *Quantum Mechanics* (Pergamon Press, Oxford, 1985).

R. H. Dicke, *Phys. Rev.* **93**, 99 (1954).

R. Diehl, *Solid St. Commun.* **17**, 743 (1975).

P. A. M. Dirac, *The Principles of Quantum Mechanics* (Clarendon Press, Oxford, 1958).

J. N. Dodd, R. D. Kaul, and D. M. Warrington, *Proc. Phys. Soc. (London)* **84**, 176 (1964).

I. Dzyaloshinsky, *Phys. Chem. Solids* **4**, 241-255 (1958).

A. Y. Dzyublik, *Phys. Stat. Sol. (b)* **123**, 53 (1984).

A. R. Edmonds, *Angular Momentum in Quantum Mechanics* (Princeton University Press, Princeton, N. J., 1960).

M. Eibschutz and M. E. Lines, *Phys. Rev. B* **7**, 4907 (1973).

C. Fabre, M. Gross, and S. Haroche, *Opt. Comm.* **13**, 393 (1975).

G. Faigel, D. P. Siddons, J. B. Hastings, P. E. Haustein, and J. R. Grover, *Phys. Rev. Lett.* **58**, 2699 (1987).

G. Faigel, D. P. Siddons, J. B. Hastings, P. E. Haustein, J. R. Grover, and L. E. Berman, *Phys. Rev. Lett.* **61**, 2794 (1988).

H. Frauenfelder, D. E. Nagle, R. D. Taylor, D. R. F. Cochran, and W. M. Visscher, *Phys. Rev.* **126**, 1065 (1962).

H. Frauenfelder, *The Mössbauer Effect* (W. A. Benjamin, New York, 1962).

H. Frauenfelder, *Subatomic Physics* (Prentice-Hall, Englewood Cliffs, N.J., 1974).

A. J. Freeman and R. B. Frankel, *Hyperfine Interactions* (Academic Press, New York, 1967).

B. S. Garbow, (Applied Mathematics Division of Argonne National Laboratory, Netlib%ANL-MCS.ARPA, 1983)

E. Gerdau, R. Rüffer, H. Winkler, W. Tolksdorf, C. P. Klages, and J. P. Hannon, *Phys. Rev. Lett.* **54**, 835 (1985).

E. Gerdau, R. Rüffer, R. Hollatz, and J. P. Hannon, *Phys. Rev. Lett.* **57**, 1141 (1986).

E. Gerdau and R. Rüffer, *Hyp. Int.* **27**, 59 (1986).

V. I. Goldanskii and R. H. Herber, *Chemical Applications of Mössbauer Spectroscopy* (Academic Press, New York, 1968).

M. L. Goldberger and K. M. Watson, *Collision Theory* (Wiley, New York, 1964).

W. Gornik, D. Kaiser, W. Lange, J. Luther, and H. H. Schulz, *Opt. Comm.* **6**, 327 (1972).

D. M. Gualtieri, W. Lavender, and S. L. Ruby, *J. Appl. Phys.* **63**, 3795 (1988).

F. Halzen and A. D. Martin, *Quarks and Leptons* (Wiley, New York, 1984).

W. C. Hamilton, *International Tables for X-Ray Crystallography*, edited by J. A. Ibers and W. C. Hamilton (Kynoch Press, Birmingham, England, 1974), vol. 4, pp. 275.

J. P. Hannon and G. T. Trammell, *Phys. Rev. Lett.* **21**, 726 (1968).

J. P. Hannon and G. T. Trammell, *Phys. Rev.* **169**, 169 (1968).

J. P. Hannon and G. T. Trammell, *Phys. Rev.* **186**, 306 (1969).

J. P. Hannon, N. J. Carron, and G. T. Trammell, *Phys. Rev. B* **9**, 2791 (1974).

J. P. Hannon, N. J. Carron, and G. T. Trammell, *Phys. Rev. B* **9**, 2810 (1974).

S. Haroche, J. A. Paisner, and A. L. Schawlow, *Phys. Rev. Lett.* **33**, 948 (1974).

S. Haroche, M. Gross, and M. Silverman, *Phys. Rev. Lett.* **33**, 1063 (1974).

S. Haroche, *High-Resolution Laser Spectroscopy* , edited by K. Shimoda, (Springer Verlag, Berlin, 1976) p. 253.

W. Heitler, *The Quantum Theory of Radiation* (Clarendon Press, Oxford, 1954).

A. Hese, A. Renn, and H. S. Schweda, *Opt. Comm.* **20**, 385 (1977).

R. Hollatz, W. Sturhahn, H. D. Rüter, and E. Gerdau, *Influence of Relative Phase Factors between Inequivalent Sites of Single Crystals on Mössbauer Experiments*, International Conference on the Applications of the Mössbauer Effect (Budapest, Hungary, 1989), vol. 2, p. 14.11.

R. M. Housley, R. W. Grant, and U. Gonser, *Phys. Rev.* **178**, 514 (1969).

T. Ishikawa, Y. Yoda, K. Izumi, C. K. Suziki, X. W. Zhang, M. Ando, and S. Kikuta, *Rev. Sci. Instrum.* **63**, 1015 (1992).

J. D. Jackson, *Classical Electrodynamics* (Wiley, New York, 1975).

R. W. James, *The Optical Principles of the Diffraction of X-Rays* (Ox Bow Press, Woodbridge, Conn., 1982).

Y. Kagan, A. M. Afanas'ev, and I. P. Perstnev, *Sov. Phys. JETP* **27**, 819 (1968).

Y. Kagan, A. M. Afanas'ev, and V. G. Kohn, *J. Phys. C* **12**, 615 (1979).

S. Kikuta, Y. Yoda, Y. Kudo, K. Izumi, T. Ishikawa, C. K. Suzuki, H. Ohno, H. Takei, K. Nakayama, X. W. Zhang, T. Matsushita, S. Kishimoto, and M. Ando, *Jpn. J. App. Phys.* **30**, L 1686 (1991).

P. P. Kovalenko, V. G. Labushkin, V. V. Rudenko, V. A. Sarkisyan, and V. N. Seleznev, *JETP Lett.* **26**, 85 (1977).

P. P. Kovalenko, V. G. Labushkin, A. K. Ovsepyan, E. R. Sarkisov, E. V. Smirnov, A. R. Prokopov, and V. N. Seleznev, *Sov. Phys. Solid State* **26**, 1849 (1984).

W. Kuhn, *Phil. Mag.* **8**, 625 (1929).

M. Lax, *Rev. Mod. Phys.* **23**, 287 (1951).

C. M. Lederer and V. S. Shirley, *Table of Isotopes* (Wiley, New York, 1978).

R. L. Liboff, *Introductory Quantum Mechanics* (Holden-Day, San Francisco, 1980).

B. A. Lippmann and J. Schwinger, *Phys. Rev.* **79**, 469 (1950).

S. P. Lloyd, *Phys. Rev.* **81**, 161 (1951).

P. R. Locher and S. Geschwind, *Phys. Rev.* **139**, A991 (1965).

F. J. Lynch, R. E. Holland, and M. Hamermesh, *Phys. Rev.* **120**, 513 (1960).

I. S. Lyubutin, E. F. Makarov, and V. A. Povitskii, *Sov. Phys. JETP* **26**, 44 (1967).

C. H. MacGillavry and G. D. Rieck, *International Tables for X-Ray Crystallography* (Kynoch Press, Birmingham, England, 1968), vol. 3.

S. Margulies and J. R. Ehrman, *Nucl. Instr. and Meth.* **12**, 131 (1961).

J. Mathews, *Tensor Spherical Harmonics* (California Institute of Technology, 1981).

E. Matthias, W. Schneider, and R. M. Steffen, *Phys. Rev.* **125**, 261 (1962).

E. Matthias, W. Schneider, and R. M. Steffen, *Arkiv Fur Fysik* **24**, 97 (1963).

H. J. Maurus, U. van Bürck, G. V. Smirnov, and R. L. Mössbauer, *J. Phys. C: Solid State Phys.* **17**, 1991 (1984).

W. H. McMaster, N. K. D. Grande, J. H. Mallett, J. H. Hubbell, and National Bureau of Standards, *Compilation of X-Ray Cross Sections*, UCRL Report 50174, Sec. III, Rev. 1 (Lawrence Radiation Laboratory, University of California, Livermore, Ca., 1969).

A. Messiah, *Quantum Mechanics* (Wiley, New York, 1962), vol. 2.

R. M. Mirzababaev, G. V. Smirnov, V. V. Sklyarevskii, A. N. Artemev, A. N. Izrailenko, and A. V. Babkov, *Phys. Lett.* **37A**, 441 (1971).

C. Moler and J. Dongarra, (Applied Mathematics Division of Argonne National Laboratory, Netlib%ANL-MCS.ARPA, 1978)

R. L. Mössbauer, *Z. Physik* **151**, 124 (1958).

R. Nathans, S. J. Pickart, H. A. Alperin, and P. J. Brown, *Phys. Rev.* **136**, A 1641 (1964).

I. I. Nikolaev, L. S. Pavlyukov, and V. P. Mar'in, *Sov. Phys. Solid State* **17**, 1016 (1975).

S. Ogawa and S. Morimoto, *J. Phys. Soc. Jpn.* **17**, 654 (1962).

A. Papoulis, *The Fourier Integral and its Applications* (McGraw-Hill, New York, 1962).

J. M. Paterson, *PEP as a Synchrotron Radiation Source: Status and Review,* SSRL ACD-NOTE **68**, (1989) [SLAC-PUB-4899, March 1989].

M. P. Petrov, G. A. Smolensky, A. P. Paugurt, and S. A. Kizhaev, *Nuclear Magnetic Resonance and Magnetic Properties of* $FeBO_3$*-Type Crystals*, edited by J. C. D. Graham, J. J.Rhynes, Proceedings of the Seventeenth Conference on Magnetism and Magnetic Materials (AIP, New York, 1971), p. 379.

R. V. Pound, *Phys. Rev.* **79**, 685 (1950).

R. S. Preston, S. S. Hanna, and J. Heberle, *Phys. Rev.* **128**, 2207 (1962).

H. Rauch, A. Zeilinger, G. Badurek, and A. Wilfing, *Phys. Lett.* **54A**, 425 (1975).

J. S. Rollett, *Computing Methods in Crystallography* (Pergamon Press, Oxford, 1965).

M. E. Rose, *Elementary Theory of Angular Momentum* (Wiley, New York, 1957).

S. L. Ruby, *J. Phys. (Paris) Colloq.* **6**, 209 (1974).

R. Rüffer, E. Gerdau, and R. Hollatz, *Phys. Rev. Lett.* **58**, 2359 (1987).

H. D. Rüter, R. Hollatz, W. Sturhahn, and E. Gerdau, *Dependence of Nuclear Diffraction on the Azimuthal Angle:* [0 0 2]- *and* [0 0 10]- *Reflections of* YIG, International Conference on the Applications of the Mössbauer Effect (Budapest, Hungary, 1989), vol. 2, p. 14.19.

H. D. Rüter, R. Rüffer, R. Hollatz, W. Sturhahn, and E. Gerdau, *Hyp. Int.* **58**, 2477 (1990).

J. J. Sakurai, *Advanced Quantum Mechanics* (Addison-Wesley, Reading, Mass., 1967).

L. I. Schiff, *Phys. Rev.* **70**, 761 (1946).

L. I. Schiff, *Quantum Mechanics* (McGraw-Hill, New York, 1968).

E. J. Seppi and F. Boehm, *Phys. Rev.* **128**, 2334 (1962).

Q. Shen, *Acta Cryst.* **A42**, 525 (1986).

C. G. Shull, W. A. Strauser, and E. O. Wollan, *Phys. Rev.* **83**, 333 (1951).

D. P. Siddons, J. B. Hastings, G. Faigel, L. E. Berman, P. E. Haustein, and J. R. Grover, *Phys. Rev. Lett.* **62**, 1384 (1989).

G. V. Smirnov, V. V. Sklyarevskii, R. A. Voskanyan, and A. N. Artem'ev, *JETP Lett.* **9**, 123 (1969).

G. V. Smirnov, V. V. Sklyarevskii, A. N. Artem'ev, and R. A. Voscanyan, *Phys. Lett.* **32A**, 532 (1970).

G. V. Smirnov, V. V. Mostovoi, Y. V. Shvyd'ko, V. N. Seleznev, and V. V. Rudenko, *Sov. Phys. JETP* **51**, 603 (1980).

G. V. Smirnov, Y. V. Shyvd'ko, and E. Realo, *JETP Lett.* **39**, 41 (1984).

P. B. Smith and P. M. Endt, *Phys. Rev.* **110**, 397 (1958).

R. M. Steffen and H. Frauenfelder, *Perturbed Angular Correlations*, edited by E. Karisson, E. Matthias, K. Siegbahn (North-Holland, Amsterdam, 1964).

H. Sugawara, *The Tristan Super Light Facility*, KEK Progress Report 92-1 (National Laboratory for High Energy Physics, Tsukuba, Japan, 1992).

C. P. Swann and F. R. Metzger, *Phys. Rev.* **108**, 982 (1957).

G. T. Trammell, *Phys. Rev.* **126**, 1045 (1962).

V. K. Voitovetskii, I. L. Korsunskii, A. I. Novikov, and Y. F. Pazhin, *Sov. Phys. JETP* **27**, 729 (1968).

V. K. Voitovetskii, I. L. Korsunskii, Y. F. Pazhin, and R. S. Silakov, *JETP Lett.* **12**, 212 (1970).

B. E. Warren, *X-Ray Diffraction* (Dover, New York, 1990).

M. Weissbluth, *Atoms and Molecules* (Academic Press, New York, 1978).

S. A. Werner, R. Colella, A. W. Overhauser, and C. F. Eagen, *Phys. Rev. Lett.* **35**,1053 (1975).

H. Wiedemann, *Storage Ring Optimization,* Handbook on Synchrotron Radiation, vol. 3, edited by G. S. Brown and D. E. Moncton (North-Holland, Amsterdam, 1991).

H. Winick, *Synchrotron Radiation,* Physics of Particle Accelerators (AIP Conference Proceedings No. **184**), vol. 2, edited by M. Month and M. Dienes (American Institute of Physics, New York, 1989)

H. Winkler, R. Eisberg, E. Alp, R. Rüffer, E. Gerdau, S. Lauer, A. X. Trautwein, M. Grodzicki, and A. Vera, *Z. Phys. B* **49**, 331 (1983).

R. W. G. Wyckoff, *Crystal Structures* , vol. 2. & 3 (Robert E. Krieger, Malabar, Florida, 1982).

W. H. Zachariasen, *Theory of X-Ray Diffraction in Crystals* (Dover, New York, 1945).

V. S. Zasimov, R. N. Kuz'min, and A. Yu. Aleksandrov, *Sov. Phys. Solid State* **17**, 2044 (1976).

X. W. Zhang, T. Mochizuki, H. Sugiyama, S. Yamamoto, H. Kitamura, T. Sioya, M. Ando, Y. Yoda, T. Ishikawa, S. Kikuta, and C. K. Suzuki, *Rev. Sci. Instrum.* **63**, 404 (1992).